Naval Research Laboratory
Washington, DC 20375-5320

Dielectric Response at THz Frequencies of Fe Water Complexes and Their Interaction with O_3 Calculated by Density Functional Theory

L. Huang
S.G. Lambrakos

Center for Computational Materials Science
Materials Science and Technology Division

A. Shabaev

George Mason University
Fairfax, Virginia

L. Massa

Hunter College
New York, New York

C. Yapijakis

The Cooper Union
New York, New York

October 24, 2012

REPORT DOCUMENTATION PAGE

1. REPORT DATE *(DD-MM-YYYY)* 24-10-2012	2. REPORT TYPE NRL Memorandum Report	3. DATES COVERED *(From - To)* October 1, 2011 – August 1, 2012

4. TITLE AND SUBTITLE

Dielectric Response at THz Frequencies of Fe Water Complexes and Their Interaction with O_3 Calculated by Density Functional Theory

5a. CONTRACT NUMBER

5b. GRANT NUMBER

5c. PROGRAM ELEMENT NUMBER

6. AUTHOR(S)

L. Huang, S.G. Lambrakos, A. Shabaev,[1] L. Massa,[2] and C. Yapijakis[3]

5d. PROJECT NUMBER

5e. TASK NUMBER

5f. WORK UNIT NUMBER
63-9564-L-2-5

7. PERFORMING ORGANIZATION NAME(S) AND ADDRESS(ES)

Naval Research Laboratory, Code 6394
4555 Overlook Avenue, SW
Washington, DC 20375-5320

8. PERFORMING ORGANIZATION REPORT NUMBER

NRL/MR/6390--12-9428

9. SPONSORING / MONITORING AGENCY NAME(S) AND ADDRESS(ES)

Office of Naval Research
One Liberty Center
875 North Randolph Street, Suite 1425
Arlington, VA 22203-1995

10. SPONSOR / MONITOR'S ACRONYM(S)
ONR

11. SPONSOR / MONITOR'S REPORT NUMBER(S)

12. DISTRIBUTION / AVAILABILITY STATEMENT

Approved for public release; distribution is unlimited.

13. SUPPLEMENTARY NOTES

[1] George Mason University, Department of Computation and Data Sciences, Fairfax, VA 22030
[2] Hunter College, City University of New York, New York, NY 10065
[3] Albert Nerkin School of Engineering, The Cooper Union, New York, NY 10003

14. ABSTRACT

The need for better monitoring of water quality and levels of water contamination implies a need for determining the dielectric response properties of water contaminants with respect to electromagnetic wave excitation. In addition to monitoring contaminants, there is an associated need for monitoring chemical processes whose purpose is deactivation or assistance in the removal of water contaminants. Two naturally occurring water contaminants, which are the result of decaying vegetation, are Iron and Manganese, where Iron is in general at much higher concentrations. Correspondingly, a process that is highly effective for assisting filtration of water contaminants, including Iron and Manganese, is the addition in solution of Ozone, i.e., the preozonation process. The present study is based on significant progress in density functional theory (DFT), and associated software technology, which is sufficiently mature for the determination of dielectric response functions, and actually provides complementary information to that obtained from experiment. This point is further demonstrated in this study by calculations of ground state resonance structure associated with water complexes of Fe and the interaction of these complexes with Ozone using DFT. The calculation of ground state resonance structure is for the construction of parameterized dielectric response functions for excitation by electromagnetic waves at frequencies within the THz range. The THz range is associated with frequencies that are characteristic of ground state resonance structure, in contrast to frequencies that can induce appreciable electronic state transitions. Dielectric functions provide for different types of analyses concerning the dielectric response of water contaminants. In particular, these dielectric response functions provide quantitative initial estimates of spectral response features for subsequent adjustment with respect to additional information such as laboratory measurements and other types of theory-based calculations. With respect to qualitative analysis, these spectra provide for the molecular level interpretation of response structure. The DFT software GAUSSIAN was used for the calculations of ground state resonance structure presented here.

15. SUBJECT TERMS

Density functional theory (DFT)	Dielectric functions	Ground state resonance	Water complexes

16. SECURITY CLASSIFICATION OF:

a. REPORT Unclassified Unlimited	b. ABSTRACT Unclassified Unlimited	c. THIS PAGE Unclassified Unlimited	17. LIMITATION OF ABSTRACT UU	18. NUMBER OF PAGES 67	19a. NAME OF RESPONSIBLE PERSON Samuel G. Lambrakos 19b. TELEPHONE NUMBER *(include area code)* (202) 767-2601

Standard Form 298 (Rev. 8-98)
Prescribed by ANSI Std. Z39.18

i

Contents

Introduction

The need for better monitoring of water quality and levels of water contamination implies a need for determining the dielectric response properties of water contaminants with respect to electromagnetic wave excitation. In addition to monitoring contaminants, there is an associated need for monitoring chemical processes whose purpose is deactivation or assistance in the removal of water contaminants. Two naturally occurring water contaminants, which are the result of decaying vegetation, are Iron and Manganese, where Iron is in general at much higher concentrations. Correspondingly, a process that is highly effective for assisting filtration of water contaminants, including Iron and Manganese, is the addition in solution of Ozone, i.e., the preozonation process. The present study is based on significant progress in density functional theory (DFT), and associated software technology, which is sufficiently mature for the determination of dielectric response functions, and actually provides complementary information to that obtained from experiment. The calculation of ground state resonance structure is for the construction of parameterized dielectric response functions for excitation by electromagnetic waves at frequencies within the THz range. The THz range is associated with frequencies that are characteristically perturbative to molecular states, and thus represent ground state resonance structure, in contrast to frequencies that can induce appreciable electronic state transitions. Dielectric functions provide for different types of analyses concerning the dielectric response of water contaminants. In particular, these dielectric response functions provide quantitative initial estimates of spectral response features for subsequent adjustment with respect to additional information such as laboratory measurements and other types of theory based calculations. With respect to qualitative analysis, these spectra provide for the molecular level interpretation of response structure. The DFT software GAUSSIAN was used for the calculations of ground state resonance structure presented here.

Typically, the dielectric response properties for electromagnetic wave excitation at THz frequencies, as well as at other frequencies, are determined by means of experimental measurements. The present study is based on significant progress in density functional theory (DFT), and associated software technology, which is sufficiently mature for the determination of dielectric response functions, and actually provides complementary information to that obtained from experiment. In particular, these dielectric response functions provide quantitative initial estimates of spectral response features that can be adjusted with respect to additional information such as laboratory measurements and other types of theory based calculations, as well as providing for the molecular level interpretation of response structure.

Density functional theory has been successfully used to investigate the vibrational spectra of energetic materials in the form of single molecules and molecular crystals [1-7]. These calculations provide detection signatures for various forms of materials, which can be encountered in various detection scenarios [8,9]. The isolated-molecule simulation results help to identify intramolecular vibrational modes in the absorption spectra of various materials. A series of studies have focused on the general concept of constructing dielectric response functions using DFT for the purpose of quantitative simulation of explosives detection scenarios [9,10,11]. As emphasized in these studies, the construction of permittivity functions using DFT calculations, defines a general approach where dielectric response is estimated within the bounds of relatively well-defined adjustable parameters. Following this approach, permittivity functions are constructed using DFT calculated absorption spectra under the condition that the calculated resonance locations are fixed, while resonance widths and number densities are assumed

adjustable with respect to additional information such as experimentally observed spectra or more advanced theory. It is significant to note that, with respect to practical application, water complexes represent a separate regime for using DFT calculations for construction of dielectric response functions.

A significant aspect of using response spectra calculated by density functional theory, DFT, for the direct construction of dielectric response functions is that it adopts the perspective of computational physics, according to which a numerical simulation represents another source of "experimental" data. This perspective is significant in that a general procedure may be developed for construction of dielectric response functions using DFT calculations as a quantitative initial estimate of spectral response features for subsequent adjustment with respect to additional information such as experimental measurements and other types of theory based calculations. That is to say, for the purpose of simulating many electromagnetic response characteristics of materials, DFT is sufficiently mature for the purpose of generating data complementing, as well as superseding, experimental measurements.

In the case of THz excitation of materials, the procedure of using response spectra calculated using DFT, which is associated with ground state resonance structure, for the direct construction of permittivity functions is well posed owing to the physical characteristic of THz excitation. In particular, it is important to note that the procedure for constructing a permittivity function using response spectra calculated using DFT is physically consistent with the characteristically linear response associated with THz excitation of molecules. Accordingly, one observes a correlation between the advantages of using THz excitation for detection of explosives (and ambient materials) and those for its numerical simulation based on DFT. Specifically, THz excitation is associated with frequencies that are characteristically perturbative to molecular states, in contrast to frequencies that can induce appreciable electronic state transitions. THz excitation does not appreciably induce electronic transitions. Moreover, in the linear (low-intensity) regime, THz excitation can be treated by means of perturbation theory. Of course, the practical aspect of the perturbative character of THz excitation for detection is that detection methodologies can be developed which do not damage materials under examination. The perturbative character of THz excitation with respect to molecular states has significant implications with respect to its numerical simulation based on DFT. It follows then that, owing to the perturbative character of THz excitation, which is characteristically linear, one is able to make a direct association between local oscillations about ground-state minima of a given molecule and THz excitation spectra.

Construction of permittivity functions according to the best fit of available data for a given material corresponding to many different types of experimental measurements has been typically the dominant approach. This approach is extended by using DFT calculations of electromagnetic response as data for construction of permittivity functions. The inclusion of this type of information is significant for accessing what spectral response features at the molecular level are actually detectable with respect to a given set of detection parameters. Accordingly, permittivity functions having been constructed using DFT calculations provide a quantitative correlation between macroscopic material response and molecular structure. Within this context it is not important that the permittivity function be quantitatively accurate for the purpose of being adopted as input for system simulation. Rather, it is important that the permittivity function be qualitatively accurate in terms of specific dielectric response features for the purpose of sensitivity analysis, which is relevant for the assessment of absolute detectability of different types of molecular structure with respect to a given set of detection parameters. That is to say,

permittivity functions that have been determined using DFT can provide a mechanistic interpretation of material response to electromagnetic excitation that could establish the applicability of a given detection methodology for detection of specific molecular characteristics. Within the context of practical application, permittivity functions having been constructed according to the best fit of available data would be "correlated" with those obtained using DFT for proper interpretation of permittivity-function features. Subsequent to establishment of good correlation between DFT and experiment, DFT calculations can be adopted as constraints for the purpose of constructing permittivity functions, whose features are consistent with molecular level response, for adjustment relative to specific sets of either experimental data or additional molecular level information. In what follows, calculations are presented of ground state resonance structure associated with water complexes of Fe and the interaction of these complexes with Ozone, which is for the construction of parameterized dielectric response functions for excitation by electromagnetic waves at compatible frequencies. For this purpose the DFT software GAUSSIAN09 (G09) was adopted [12].

The organization of the subject areas presented here are as follows. First, a brief example is presented of the significance of Iron and Manganese concentrations in water and of their interaction with Ozone. Second, a brief description is presented of vibrational analysis using DFT for the calculation of absorption spectra and of the construction of permittivity functions using DFT calculated spectra. This includes a general review of the formal structure of permittivity functions in terms of analytic function representations. An understanding of the formal structure of permittivity functions in terms of both physical consistency and causality is important for post-processing of DFT calculations for the purpose of constructing permittivity functions. Third, information concerning the ground state resonance structure of Fe water complexes and of their interaction with Ozone, which is obtained using DFT, is presented. This information consists of the ground state molecular geometries and response spectra for different types of Fe water complexes, with and without the presence of Ozone. Fourth, a discussion is presented that elucidates the utility of information concerning the ground state resonance structure of Fe water complexes with ot without the presents of Ozone. This discussion also suggests procedures for the construction of permittivity functions that are in terms of reduced sets of phenomenological parameters. Finally, a conclusion is given summarizing the significance of modeling the dielectric response of molecular clusters relative to monitoring of water contamiants in practice.

Example of the Significance of Iron and Manganese Concentrations
in Water and of Their Interaction with Ozone

New York City's water reservoirs, like all other cities upland water storage systems, have a continuous or occasional water quality problem when the two primary parameters of color colloids and turbidity inert particulates exceed the desirable limits. As these color colloidal particles are the result of decaying vegetation, the accompanying consequence is higher concentrations of both iron and manganese in the water, as both metals are present in the original vegetation and thereby in the color colloids resulting from the decay. Iron, of course, is present in much higher concentrations than manganese.

As the above mentioned water quality parameters are present in relatively low concentrations in typical upland water supply reservoirs, and as the size of all these particulates

are very small, the traditionally used water treatment of coagulation, flocculation, coarse dual media filtration would not only prove inefficient, but it would also require an addition of a disproportional amount of chemicals resulting in a large amount of a chemical sludge requiring disposal. Therefore, the diatomaceous earth filter media with their much smaller size of media particles and the resulting much smaller pore sizes, would be the most suitable filtering media for the treatment of these specific water pollutants requiring removal. Additionally, since the only chemical being added to the process is more diatomaceous earth, and as about 85 percent or more of the total DE material is being recovered and recycled in every run cycle, the resulting sludge is of a considerably lesser quantity and much more innocuous in its disposal.

The preozonation step added prior to the DE process has as its aim the oxidation of the soluble ionized ferric and manganic tiny particulates, therefore resulting in insoluble colloids of ferrous and manganous compounds. These can then be filtered out by the DE process much more efficiently, resulting in a desirable reduction of the iron and manganese concentrations, which are harmful to health, in addition to color and turbidity units reduction.

Therefore, as color levels in the water supply quality are closely correlated to both the turbidity and the iron and manganese concentrations, in modeling the preozonation, DE filtration process there seemed to be no statistical need to also include color as an additional modeling parameter. A multiparameter multiple regression analysis of the NYC pilot test data, which included color data as well, verified this assumption.

Construction of Dielectric Response Functions using DFT

As in previous studies [9,10,11] the formal mathematical structure underlying DFT calculations, as well as the procedure for constructing permittivity functions using these calculations, is included here for purposes of completeness. A brief description of this mathematical structure is as follows.

The DFT software GAUSSIAN09 (G09) can be used to compute an approximation of the IR absorption spectrum of a molecule or molecules [12]. This program calculates vibrational frequencies by determining second derivatives of the energy with respect to the Cartesian nuclear coordinates, and then transforming to mass-weighted coordinates at a stationary point of the geometry [13]. The IR absorption spectrum is obtained using density functional theory to compute the ground state electronic structure in the Born-Oppenheimer approximation using Kohn-Sham density functional theory [14-18]. GAUSSIAN uses specified orbital basis functions to describe the electronic wavefunctions and density. For a given set of nuclear positions, the calculation directly gives the electronic charge density of the molecule, the potential energy V, and the displacements in Cartesian coordinates of each atom. The procedure for vibrational analysis followed in GAUSSIAN is that described in [19]. Reference [20] presents a fairly detailed review of this procedure. A brief description of this procedure is as follows.

The procedure followed by GAUSSIAN is based on the fact the vibrational spectrum depends on the Hessian matrix $\mathbf{f}_{CART}$, which is constructed using the second partial derivatives of the potential energy V with respect to displacements of the atoms in Cartesian coordinates. Accordingly, the elements of the $3N$ x $3N$ matrix $\mathbf{f}_{CART}$ are given by

$$f_{CARTij} = \left(\frac{\partial^2 V}{\partial \xi_i \partial \xi_j} \right)_0 \tag{1}$$

where $\{\xi_1, \xi_2, \xi_3, \xi_4, \xi_5, \xi_6, ..., \xi_{3N}\} = \{\Delta x_1, \Delta y_1, \Delta z_1, \Delta x_2, \Delta y_2, \Delta z_2, ..., \Delta z_N\}$, which are displacements in Cartesian coordinates, and N is the number of atoms. As discussed above, the zero subscript in Eq.(1) indicates that the derivatives are taken at the equilibrium positions of the atoms, and that the first derivatives are zero. Given the Hessian matrix defined by Eq.(1) the operations for calculation of the vibrational spectrum require that the Hessian matrix Eq.(1) be transformed to mass-weighted Cartesian coordinates according to the relation

$$f_{\text{MWC}ij} = \frac{f_{\text{CART}ij}}{\sqrt{m_i m_j}} = \left(\frac{\partial^2 V}{\partial q_i \partial q_j} \right)_0 \tag{2}$$

where $\{q_1, q_2, q_3, q_4, q_5, q_6, ..., q_{3N}\} = \{\sqrt{m_1}\Delta x_1, \sqrt{m_1}\Delta y_1, \sqrt{m_1}\Delta z_1, \sqrt{m_2}\Delta x_2, \sqrt{m_2}\Delta y_2, \sqrt{m_2}\Delta z_2, ..., \sqrt{m_N}\Delta z_N\}$ are the mass-weighted Cartesian coordianates. GAUSSIAN computes the energy second derivatives Eq.(2), thus computing the forces for displacement perturbations of each atom along each Cartesian direction. The first derivatives of the dipole moment with respect to atomic positions $\partial\vec{\mu}/\partial\xi_i$ are also computed. Each vibrational eigenmode leads to one peak in the absorption spectrum, at a frequency equal to the mode's eigenfrequency v_{n0}. The absorption intensity corresponding to a particular eigenmode n whose eigenfrequency is v_{n0} is given by

$$I_n = \frac{\pi}{3c} \left| \sum_{i=1}^{3N} \frac{\partial\vec{\mu}}{\partial\xi_i} l_{\text{CART}in} \right|^2, \tag{3}$$

where $\mathbf{l}_{\text{CART}}$ is the matrix whose elements are the displacements of the atoms in Cartesian coordinates. The matrix $\mathbf{l}_{\text{CART}}$ is determined by the following procedure. First,

$$\mathbf{l}_{\text{CART}} = \mathbf{M}\mathbf{l}_{\text{MWC}}, \tag{4}$$

where $\mathbf{l}_{\text{MWC}}$ is the matrix whose elements are the displacements of the atoms in mass-weighted Cartesian coordinates and $\mathbf{M}$ is a diagonal matrix defined by the elements

$$M_{ii} = \frac{1}{\sqrt{m_i}}. \tag{5}$$

Proceeding, $\mathbf{l}_{\text{MWC}}$ is the matrix needed to diagonalize $\mathbf{f}_{\text{MWC}}$ defined by Eq.(2) such that

$$(\mathbf{l}_{\text{MWC}})^{\text{T}} \mathbf{f}_{\text{MWC}} (\mathbf{l}_{\text{MWC}}) = \Lambda, \tag{6}$$

where Λ is the diagonal matrix with eigenvalues λ_i. The procedure for diagonalizing Eq.(6) consists of the operations

$$\mathbf{f}_{\text{INT}} = (\mathbf{D})^{\text{T}} \mathbf{f}_{\text{MWC}} (\mathbf{D}) \tag{7}$$

and

$$(\mathbf{L})^{\text{T}} \mathbf{f}_{\text{MWC}} (\mathbf{L}) = \Lambda, \tag{8}$$

where $\mathbf{D}$ is a matrix transformation to coordinates where rotation and translation have been

separated out and **L** is the transformation matrix composed of eigenvectors calculated according to Eq.(8). The eigenfrequencies in units of (cm^{-1}) are calculated using the eigenvalues λ_n by the expression

$$\nu_{n0} = \frac{\sqrt{\lambda_n}}{2\pi c} \ , \tag{9}$$

where c is the speed of light. The elements of $\mathbf{l}_{\mathrm{CART}}$ are given by

$$l_{\mathrm{CART}ki} = \sum_{j=1}^{3N} \frac{D_{kj} L_{ji}}{\sqrt{m_j}} \ , \tag{10}$$

where $k, i=1,\ldots, 3N$, and the column vectors of these elements are the normal modes in Cartesian coordinates.

The intensity Eq.(3) must then be multiplied by the number density of molecules to give an absorption-line intensity in the non-interacting molecule approximation. It follows that the absorption spectrum calculated by GAUSSIAN is a sum of delta functions, whose line positions and cefficients correspond to the vibrational-transition frequencies and the absorption-line intensities, respectively. In principle, however, these spectral components must be broadened and shifted to account for anharmonic effects such as finite mode lifetimes and inter-mode couplings.

The construction of permittivity functions using DFT calculations requires that a specific parametric function representation be adopted. This parametric representation must be physically consistent with specific molecular response characteristics, while limiting the inclusion of feature characteristics that tend to mask response signatures that may be potentially detectable. In principle, parameterizations are of two classes. One class consists of parameterizations that are directly related to molecular response characteristics. This class of parameterizations would include spectral scaling and width coefficients. The other class consists of parameterizations that are purely phenomenological and are structured for optimal and convenient best fits to experimental measurements. A sufficiently general parameterization of permittivity functions is given by Drude-Lorentz approximation [21]

$$\varepsilon(\nu) = \varepsilon'(\nu) + i\varepsilon''(\nu) = \varepsilon_\infty + \sum_{n=1}^{N} \frac{\nu_{np}^2}{(\nu_{no}^2 - \nu^2) - i\gamma_n \nu} \ , \tag{11}$$

where ν_{np} and γ_n are the spectral scaling and width of a resonance contributing to the permittivity function. The permittivity ε_∞ is a constant since the dielectric response at high frequencies is substantially detuned from the probe frequency. The real and imaginary parts, $\varepsilon_r(\nu)$ and $\varepsilon_i(\nu)$, respectively, of the permittivity function can be written separately as

$$\varepsilon_r(\nu) = \varepsilon_\infty + \sum_{n=1}^{N} \frac{\nu_{np}^2 (\nu_{no}^2 - \nu^2)}{(\nu_{no}^2 - \nu^2)^2 + \gamma_n^2 \nu^2} \quad \text{and} \quad \varepsilon_i(\nu) = \sum_{n=1}^{N} \frac{\nu_{np}^2 \gamma_n \nu}{(\nu_{no}^2 - \nu^2)^2 + \gamma_n^2 \nu^2} \ . \tag{12}$$

6

With respect to practical application, the absorption coefficient α and index of refraction n_r, given by

$$\alpha = \frac{4\pi\nu}{\sqrt{2}}\left[-\varepsilon_r + \sqrt{\varepsilon_r^2 + \varepsilon_i^2}\right]^{1/2} \quad \text{and} \quad n_r = \frac{1}{\sqrt{2}}\left[\varepsilon_r + \sqrt{\varepsilon_r^2 + \varepsilon_i^2}\right]^{1/2}, \tag{13}$$

respectively, provide direct relationships between calculated quantities obtained by DFT and the "conveniently measurable" quantities α and n_r. It is significant to note that in what follows, the absorption coefficient α is determined using DFT calculated spectra in the same spirit as for its measurement in the laboratory. Although permittivity functions $\varepsilon(\nu)$ are not determined explicitly in the present study, it must be kept in mind that the ultimate construction of these functions is necessary for using DFT calculated spectra to model the dielectric response of complex composite materials and associated detector designs [9].

Physical Significance of Quantum Mechanical Transition State for Molecular Transformation

A molecule in 3-dimensions has a total of 3N-6 normal mode vibrations. The Schrodinger equation for the harmonic oscillations of these normal modes has known solutions. The quantum mechanical spectrum of each of these vibrations is given in the harmonic approximation by the energies E_n = (n+1/2)hν, where n is a quantum number, h is Planck's constant, and ν is a vibration frequency given by $\nu = \sqrt{(k/m)}$, where k is the spring constant of the normal vibration and m is the effective mass contributed by those atoms vibrating in the normal mode. A molecule in stable equilibrium is characterized by all positive normal mode frequencies ν. But the definitive mathematical characteristic of a transition state is that it has all positive frequencies but one, which is imaginary. That is to say, (k/m) is a negative number. The vibration corresponding to an imaginary frequency is one in which the atoms are breaking away from bonds characteristic of chemical reactants and are moving towards those bonds characteristic of chemical products. Chemical reactions break bonds in the reactants, rearrange them and form new bonds in the products. The transition state is a particular geometric arrangement of the atoms in a chemical system, at the maximal peak of the energy surface separating reactants from products. In the transition state every normal vibration distortion but one, occurs within a stable energy minimum. But the one normal mode distortion of imaginary frequency occurs at an unstable energy maximum sending reactants toward products. The height of energy peak, the activation energy E_a, associated with the occurrence of a transition state determines the minimal energy accumulated by reactants to surmount the barrier separating reactants from products. In the Arrhenius formulation, the rate constant for the reaction is given by k = A e$^{-Ea/RT}$, where A is a constant, R is the ideal gas constant, and T is the absolute temperature. The common occurrence is that a particular transition state mechanism for chemical reaction is associated with one imaginary frequency, and therefore a single mechanism of reaction. Much less commonly, an energy surface of multiple channels of reaction mechanism may give rise to correspondingly multiple of imaginary frequencies. But in any event, the transition state contains the energetic and geometric information that defines the transformation inherent within chemical reactions.

Ground State Resonance Structure of Fe Water Complexes
And of Their Interaction with Ozone

In this section are presented the results of computational investigations using DFT concerning Fe water complexes and their interaction with Ozone. These results include the relaxed or equilibrium configurations of Fe water complexes, their interaction with Ozone, and ground-state oscillation frequencies and IR intensities for different geometries of the interacting systems associated with stable structures, which are calculated by DFT according to the frozen phonon approximation. For these calculations geometry optimization and vibrational analysis was effected using the DFT model B3LYP [22, 23] and basis function 6-31G(d,p) [24, 25]. According to the specification of this basis function, (d,p) designates polarization functions having 1 set of d functions for heavy atoms and 1 set of p functions for hydrogen atoms [26].

In general the geometry of any given Fe water complex interacting with Ozone will depend on the electronic configuration of the Ozone, as well as the orientation of Ozone relative to the Fe complex. Shown in Fig. 1 are schematic representations of different electronic configurations of Ozone for neutral and charged structures [27]. Shown in Fig. 2 are schematic representations of different orientations of Ozone with respect to approach to Fe [28].

Shown in Figs. 3 through 9 are geometries and energies of Fe water complexes with and without Ozone, before and after geometry optimization, and with and without the presence of a water solvent background. In addition, indicated in Figs. 3 through 9 are the numbers of imaginary frequencies associated with the optimized geometries.

Proceeding, it is to be noted that the Fe water complex $[Fe(H_2O)_6]^{+2}$ can be associated with two types of symmetry, which are represented by symmetry groups D_{4h} and D_{3d} [29,30]. These two symmetries are shown schematically in Fig.10. Accordingly, the interaction of this Fe complex with Ozone will depend on these symmetries. Shown in Figs. 11 through 14 are geometries and energies of complexes $[Fe(H_2O)_6]^{+2}$ for D_{4h} and D_{3d}, with and without Ozone, before and after geometry optimization, and with and without the presence of a water solvent background. In addition, indicated in Figs. 11 through 14 are the numbers of imaginary frequencies associated with the optimized geometries.

Shown in Figs. 15 through 32 are IR spectra calculated for the optimized geometries shown in Figs. 3 through 32. Again, it must be noted that only a fraction of these calculated spectra are to be associated with stable structures, i.e., structure for which there are no imaginary frequencies. The IR intensities shown in these figures are given in the form of continuous spectrum representations of the spectra. Comparison of these figures shows relative changes of intensities for individual resonances for the various Fe water complexes and their interaction with Ozone relative to the single molecule. The continuous spectra shown in Figs. 15 through 32 are constructed using a superposition of essentially Lorenzian functions of various heights and widths, which have been fit to the discrete spectra, which have been calculated using DFT. This construction is applied within the GAUSSIAN program [12].

Shown in Tables 1 and 2 are comparisons of energies and numbers of imaginary frequencies for initial and optimized geometries of $[Fe \cdot 3(H_2O) \cdot O_3]^{+2}$ and $[Fe \cdot 3(H_2O) \cdot O_3]$, respectively, with and without the presence of a water solvent background. Shown in Tables 3 and 4 are comparisons of energies and numbers of imaginary frequencies for initial and optimized geometries of $[Fe-O_3]^{+2}$ and $[Fe-O_3]$, respectively, in presence of a water solvent background. Finally, shown in Table 5 is a comparison of energies and numbers of imaginary frequencies for initial and optimized geometries of $[Fe(H_2O)_5]^{+2}$ with and without the presence

of a water solvent background, and for the different symmetries D_{4h} and D_{3d}.

Shown in Tables 6 through 12 are frequencies and IR intensities for stable structures of Fe water complexes with and without interaction with Ozone, and without the presence of a water solvent background.

Discussion

The DFT calculated absorption spectra given in Tables 6 through 12 provide two types of information for general analysis of dielectric response. These are the denumeration of ground state resonance modes and estimates of molecular level dielectric response structure. The construction of permittivity functions using the DFT calculated absorption spectra follows the same procedure as that applied for the construction of permittivity functions using experimentally measured absorption spectra, but with the addition of certain constraint conditions. Accordingly, construction of permittivity functions using either DFT or experimentally measured absorption spectra requires parameterizations that are in terms of physically consistent analytic function representations such as the Drude-Lorentz model. Although the formal structure of permittivity functions constructed using DFT and experimental measurements are the same, their interpretation with respect to parameterization is different for each case.

The construction of permittivity functions using experimental measurements defines an inverse problem where resonant locations, peaks and widths, as well as the number of resonances, are assumed adjustable. Following this approach, it follows that many of the detailed characteristics of resonance structure are smoothed or averaged. In addition, measurement artifacts associated with sample preparation and detector configuration can in principle introduce errors. One advantage of permittivity functions constructed using experimental measurements, however, is that many aspects of dielectric response on the macroscale that are associated with multiscale averaging and molecule-lattice coupling are taken into account inherently. Accordingly, the disadvantage of this approach is that the nature of any multiscale averaging and resonant structure, contributing to dielectric response on the macroscopic level, may not be understood. This lack of quantitative understanding can in principle inhibit the development of methodologies for selective excitation of molecular modes, which are for the purpose of enhanced signature detection. Better interpretation of dielectric response of explosives on a macroscale can be achieved through correlation of resonance structure, which is experimentally observed, with spectra calculated by DFT. In principle, correlation of resonance structure would include the quantitative analysis of changes in signature features associated with the transition of the system from that of a low-density system of uncoupled molecule to that of systems consisting of molecules coupled to their molecular environment. Among these types of systems are molecular clusters of explosive molecules [27] or individual explosive molecules having intermolecular coupling with their ambient environment, consisting of either bulk systems or individual molecules, which would include water complexes.

One approach for the construction of permittivity functions using DFT calculations, discussed previously [10,11], is that of a direct problem approach where dielectric response is estimated within the bounds of relatively well-defined adjustable parameters. Following this approach, a permittivity function is constructed using the DFT calculated absorption spectra under the condition that the calculated resonance locations are fixed, while resonance widths and

number densities are assumed adjustable. With respect to this approach, reference is made to Figs. 15 through 32, which show continuous spectra consisting of a superposition of essentially Lorenzian functions of various heights and widths, constructed using discrete spectra. Although the primarily purpose of this type of construction within GAUSSIAN is for the purpose of enhanced visualization of spectral features, it is significant to note that this operation represents, at some level, a zeroth-order estimation of the characteristic scaling and widths of resonances contributing the dielectric response, i.e., permittivity function. For qualitative comparison of spectral features this type of zeroth-order estimate should be sufficient. For the construction of permittivity functions to be used for quantitative simulations, it is more appropriate, however, to assume the characteristic scaling and widths of DFT calculated resonances as adjustable parameters, i.e., parameters to be assigned values according to additional information.

Following an approach for construction of permittivity functions using DFT, which assumes the characteristic scaling and widths of resonances as adjustable parameters, inverse methods of analysis can be adopted. Accordingly, permittivity functions can be constructed using superpositions of Lorenzian functions that are in terms of reduced sets of phenomenological scaling and widths of resonances. This approach should consider, in principle, the sensitivity of reflectivity, as would be measured by a specific detection design (see reference [9]), with respect to variation in values of the associated phenomenological scaling and widths of resonances.

It must be emphasized again here, as in previous studies [10,11], that one purpose of DFT calculated spectra, related to practical application and extremely important for interpretation signature features and the design of detection or monitoring systems, is the quantitative analysis of the inherent limitation on levels of detection associated with various types of detection strategies. With respect to the purpose of examining inherent limitations on monitoring of water contaminants, the dominant features of response spectra that are calculated using DFT provide a foundation for establishing what level of detection is achievable in the absence of instrumental and environmental factors associated with detection. Accordingly, the approach presented here, for construction of permittivity functions, provides a specific application of DFT. For any given water contaminant, e.g., metal-water complex, and frequency range of the incident electromagnetic wave, DFT can calculate a set of response signatures that are each characterized by an excitation frequency, magnitude and width. These response signatures must then be adjusted parametrically to construct permittivity functions. Accordingly, parameter adjustment with respect to a given set of experimental measurements, which would entail parameter optimization and sensitivity analysis, will determine what types of signature structure are recoverable at the level of detection for a given detector design.

Finally, the DFT calculations presented here were performed using the DFT software GAUSSIAN. With respect to the approach presented here for construction of permittivity functions, these calculations represent results of numerical experiments with the "numerical apparatus" GAUSSIAN, which has associated with it specific discrete numerical representations and associated approximations. Again, an underlying factor supporting the construction of permittivity functions using DFT calculated spectra is that the associated software technology has evolved to a point of maturity where dielectric response to electromagnetic excitation can be determined quantitatively for large molecular systems.

Conclusion

The calculations of ground state resonance structure associated with Fe water complexes and their interaction with Ozone using DFT are meant to serve as reasonable estimates of molecular level response characteristics, providing interpretation of dielectric response features, for subsequent adjustment relative to experimental measurements and additional constraint based on molecular structure theory. With respect to spectroscopic methods for monitoring levels of water contamination, i.e., different types of detection strategies and their associated algorithms for post-processing of measurements, the calculated resonance spectra presented here serve the purpose of simulating detector designs for detection of water contaminants. That is to say, for detection of spatially distributed water complexes that correlate with different types of contaminants, these spectra can be assumed as a reasonable estimate of dielectric response for purposes of the practical detection.

Acknowledgement

References

[1]   B. M. Rice and C. F. Chabalowski, "Ab Initio and Nonlocal Density Functional Study of 1,3,5-Trinitro-s-triazine (RDX) Conformers,``J. Phys. Chem., **101**, 8720 (1997).

[2]   Y. Chen, H. Liu, Y. Deng, D. Schauki, M. J. Fitch, R. Osiander, C. Dodson, J. B. Spicer, M. Shur, and X.-C. Zhang, "THz spectroscopic investigation of 2,4-dinitrotoluene," Chemical Physics Letters, **400**, 357-361 (2004).

[3]   D. G. Allis, D. A. Prokhorova, and T. M. Korter, "Solid-State Modeling of the Terahertz Spectrum of the High Explosive HMX," J. Phys. Chem. A., **110**, 1951-1959 (2006).

[4]   D.G. Allis and T. M. Korter, "Theoretical Analysis of the Terahertz Spectrum of the High Explosive PETN," Chem. Phys. Chem., **7**, 2398 (2006).

[5]   J. Chen, Y. Chen, H. Zhao, G. J. Bastiaans, and X.-C. Zhang, Opt. Exp., **15**, 11763 (2007).

[6]   M.R. Leahy-Hoppa, M.J. Fitch, X. Zheng, L.M. Hayden, and R. Osiander, "Wideband terahertz spectroscopy of explosives," Chemical Physics Letters **434**, 227-230 (2007).

[7]   J. Hooper, E. Mitchell, C. Konek, and J. Wilkinson, "Terahertz spectroscopy techniques for explosives detection," Chem. Phys. Lett., **467**, 309 (2009).

[8]   M.R. Leahy-Hoppa, M.J. Fitch, and R. Osiander,"Terahertz spectroscopy techniques for explosives detection," Anal. Bioanal. Chem., **395**, 247 (2009).

[9]   A. Shabaev, S. G. Lambrakos, N. Bernstein, V. L. Jacobs and D. Finkenstadt, "A General Framework for Numerical Simulation of Improvised Explosive Device (IED)-Detection Scenarios Using Density Functional Theory (DFT) and Terahertz (THz) Spectra," Appl. Spectroscopy, **65**, 409 (2011).

[10]   A. Shabaev, S.G., Lambrakos, N. Bernstein, V. Jacobs, D. Finkenstadt, "THz Dielectric Properties of High Explosives Calculated by Density Functional Theory for the Design Of Detectors," Journal of Materials Engineering and Performance, DOI: 10.1007/s11665 011-9857-8, 20 (9), 2011, p.1536.

[11]   L. Huang, A. Shabaev, S.G. Lambrakos, N. Bernstein, V. Jacobs, D. Finkenstadt, L. Massa, "Dielectric Response of High Explosives at THz Frequencies Calculated Using Density Functional Theory," Journal of Materials Engineering and Performance, 2011, DOI: 10.1007/s11665-011-0020-3.

[12]   M. J. Frisch, G. W. Trucks, H. B. Schlegel, G. E. Scuseria, M. A. Robb, J. R. Cheeseman, G. Scalmani, V. Barone, B. Mennucci, G. A. Petersson, H. Nakatsuji, M. Caricato, X. Li, H. P. Hratchian, A. F. Izmaylov, J. Bloino, G. Zheng, J. L. Sonnenberg, M. Hada, M. Ehara, K. Toyota, R. Fukuda, J. Hasegawa, M. Ishida, T. Nakajima, Y. Honda, O. Kitao, H. Nakai, T. Vreven, J. A. Montgomery, Jr., J. E. Peralta, F. Ogliaro, M. Bearpark, J. J. Heyd, E. Brothers, K. N. Kudin, V. N. Staroverov, R. Kobayashi, J. Normand, K. Raghavachari, A. Rendell, J. C. Burant, S. S. Iyengar, J. Tomasi, M. Cossi, N. Rega, J. M. Millam, M. Klene, J. E. Knox, J. B. Cross, V. Bakken, C. Adamo, J. Jaramillo, R. Gomperts, R. E. Stratmann, O. Yazyev, A. J. Austin, R. Cammi, C. Pomelli, J. W. Ochterski, R. L. Martin, K. Morokuma, V. G. Zakrzewski, G. A. Voth, P. Salvador, J. J. Dannenberg, S. Dapprich, A. D. Daniels, Ö. Farkas, J. B. Foresman, J. V. Ortiz, J. Cioslowski, and D. J. Fox, Gaussian 09, Revision A.1, Gaussian, Inc., Wallingford CT, 2009.

[13]   A. Frisch, M. J. Frisch, F. R. Clemente and G. W. Trucks, *Gaussian 09 User's Reference,* Gaussian Inc., 2009, p, 105-106, online: www.gaussian.com/g_tech/g_ur/g09help.htm

[14]   P. Hohenberg and W. Kohn, "Inhomogeneous Electron Gas" Phys. Rev. **136**, B864, (1964).

[15]   W. Kohn and L. J. Sham, "Self-Consistent Equations Including Exchange and Correlation Effects" Phys. Rev. **140**, A1133 (1965).

[16]   R.O. Jones and O. Gunnarson, "The density functional formalism, its applications and prospects" Rev. Mod. Phys. **61**, 689 (1989).

[17]   W.W. Hager and H. Zhang, "A survey of nonlinear conjugate gradient methods," Pacific J. Optim., 2, p. 35-58 (2006).

[18]   R. M. Martin, *Electronic Structures Basic Theory and Practical Methods*, Cambridge University Press, Cambridge 2004, p. 25.

[19]   E. B. Wilson, J. C. Decius and P. C. Cross, *Molecular Vibrations* (McGraw-Hill, New York, 1955).

[20]   J.W. Ochterski, "Vibrational Analysis in Gaussian," help@gaussian.com, 1999.

[21]   C. A. D. Roeser and E. Mazur, "Light-Matter Interactions on Femtosecond Time Scale" in *Frontiers of Optical Spectroscopy*, eds. B. Di Bartolo and O. Forte, NATO Science Series v. 168 p. 29, Kluwer Academic Publishers, Dordrecht − Norwell, 2005; C. F. Bohren and D. R. Huffman, *Absorption and Scattering of Light by Small Particles* (Wiley-VCH Verlag, Weinheim, 2004).

[22]   A. D. Becke, "Density-functional Thermochemistry. III. The Role of Exact Exchange"*, J. Chem. Phys.* **98**, 5648-5652 (1993).

[23]   B. Miehlich, A. Savin, H. Stoll and H. Preuss, "Results Obtained with the Correlation Energy Density Functionals of Becke and Lee, Yang and Parr", Chem. *Phys. Lett.* **157**, 200-206 (1989).

[24]   A. D. McLean and G. S. Chandler, "Contracted Gaussian-basis sets for molecular calculations. 1. 2nd row atoms, Z=11-18," *J. Chem. Phys.*, **72** 5639-48 (1980).

[25]   T. Clark, J. Chandrasekhar, G. W. Spitznagel and P. V. R. Schleyer, "Efficient diffuse function-augmented basis-sets for anion calculations. 3. The 3-21+G basis set for 1st-row elements, Li-F," *J. Comp. Chem.*, **4** 294-301, (1983).

[26]   M. J. Frisch, J. A. Pople and J. S. Binkley, "Self-Consistent Molecular Orbital Methods. 25. Supplementary Functions for Gaussian Basis Sets," *J. Chem. Phys.*, **80** (1984) 3265-69.

[27]   B. Flemming, P. T. Wolczanski and R. Hoffman, "Transition Metal Complexes of Cyclic and Open Ozone and Thiozone," JACS vol. 127, 1278-1285 (2005).

[28]   G. A. Venter, H. G. Raubenheimer and J. Dillen, "On the Structure and Bonding of First Row Transition Metal Ozone Carbonyl Hydrides," *J. Phys. Chem.*, 111, 8193-8201 (2007).

[29]   A. Fouqueau, S. Mer and M. E. Casida, "Comparison of density functional for energy and structural differences between the high-$[^5T_{2g}: (t_{2g})^4(e_g)^2]$ and low-$[^1A_{1g}: (t_{2g})^6(e_g)^0]$ spin states of the hexaquoferrous cation $[Fe(H_2O)^6]^{+2}$", *J. Chem. Phys.* Vol 120, 20, 9473-9486, (2004).

[30]   C. S. Babu, M. Madhusoodanan, G. Sridhar and B. L. Tembe, "Orientations of $[Fe(H_2O)_6]^{+2}$ and $[Fe(H_2O)_6]^{+3}$ Complexes at a Reactive Separation in Water" *J. AM. Chem. Soc.* 119, 5679-5681 (1997)

Ozone (O^3)
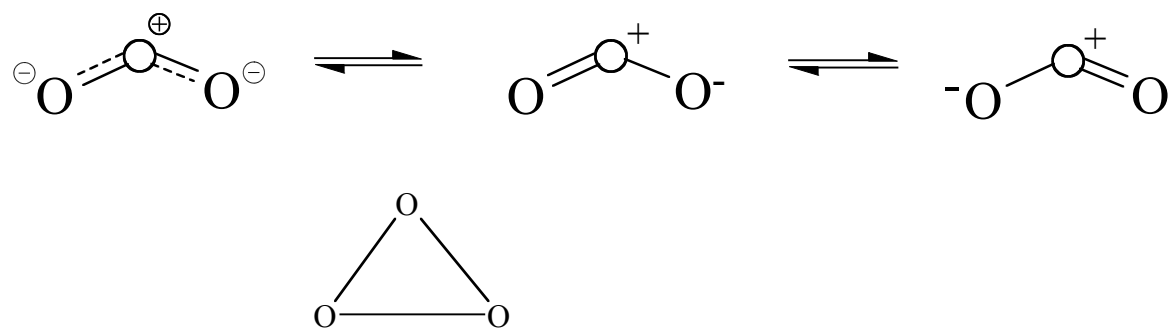
Ozone (O_3^{-2})
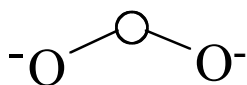
Figure 1. Schematic representations of different electronic configurations of Ozone for neutral and charged structures [27].

(a) (b) (c) (d)
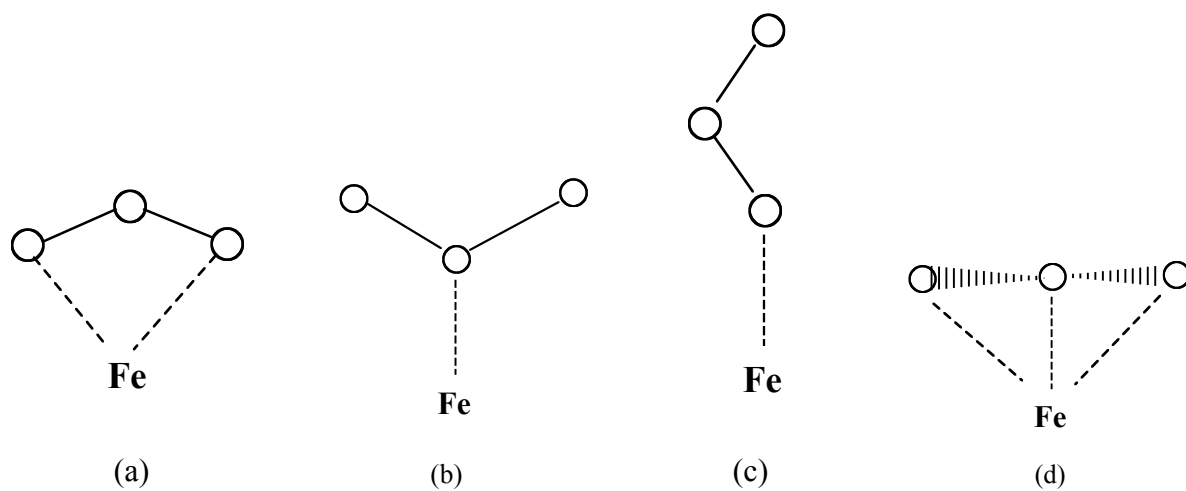
Figure 2. Schematic representations of different orientations of Ozone with respect to approach to Fe [28].
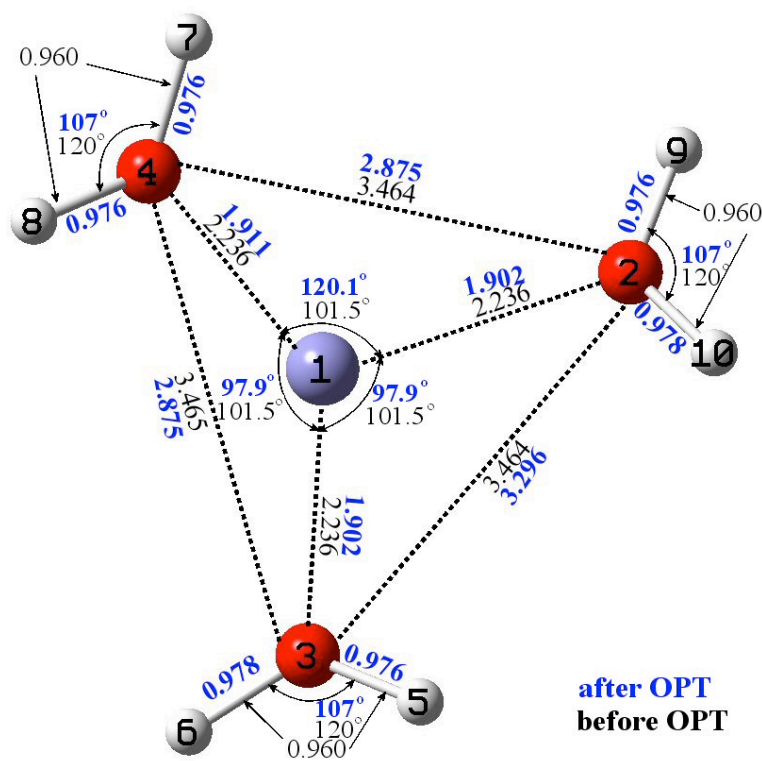
Figure 3. Geometry of complex [Fe^{++}(H$_2$O)$_3$], without Ozone, before (black) and after (blue) geometry optimization. The energies of the complexes before and after geometry optimization are E$_s$=-1492.133 a.u. and E$_F$= -1492.195 a.u., respectively, with 1 imaginary frequency. For optimization in the presence water the energies of the complexes before and after geometry optimization are E$_s$=-1492.526 a.u. and E$_F$= -1492.574 a.u. This optimized state had 1 imaginary frequency.
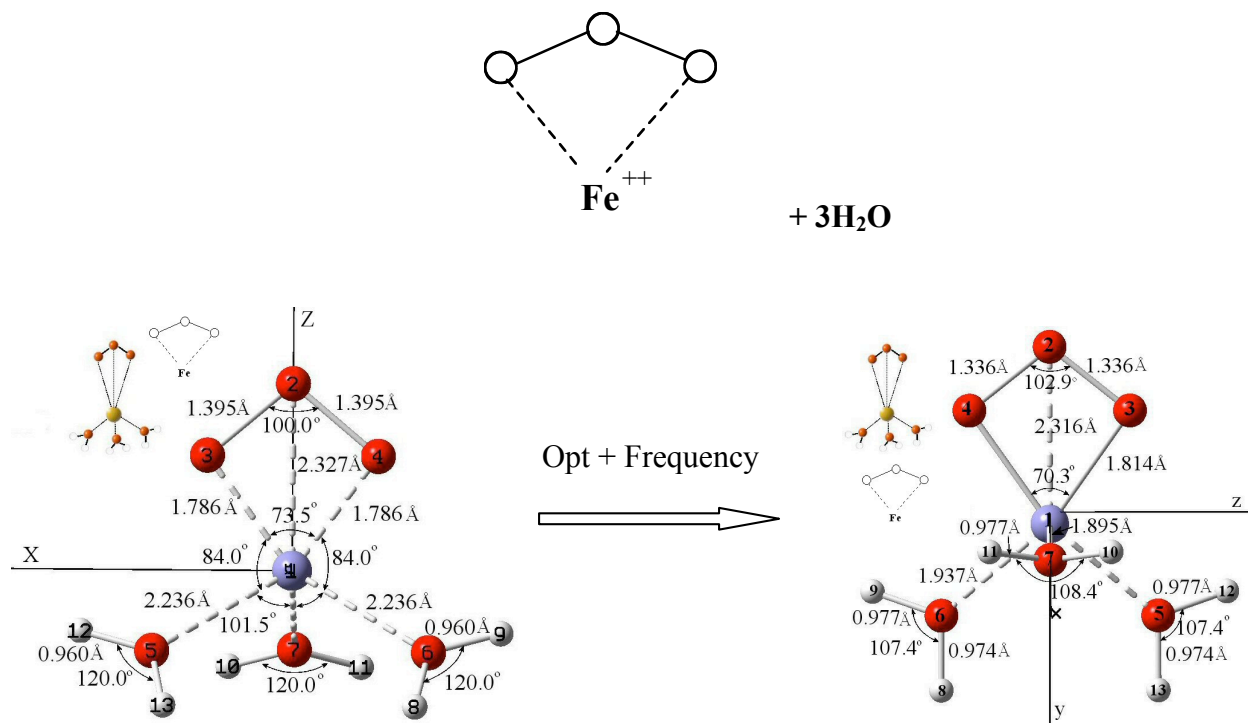
Figure 4(a). Geometry of $[Fe-3(H_2O)-O_3]^{+2}$, for the Ozone approach orientation shown, before and after geometry optimization. The energies of the systems before and after geometry optimization are E_s=-1717.637 a.u. and E_F= -1717.706 a.u., respectively, with 1 imaginary frequency. For optimization in the presence water solvent background, the energies of the systems before and after geometry optimization are E_s=-1717.964 a.u. and E_F= -1718.042 a.u. This optimized state had 1 imaginary frequency.
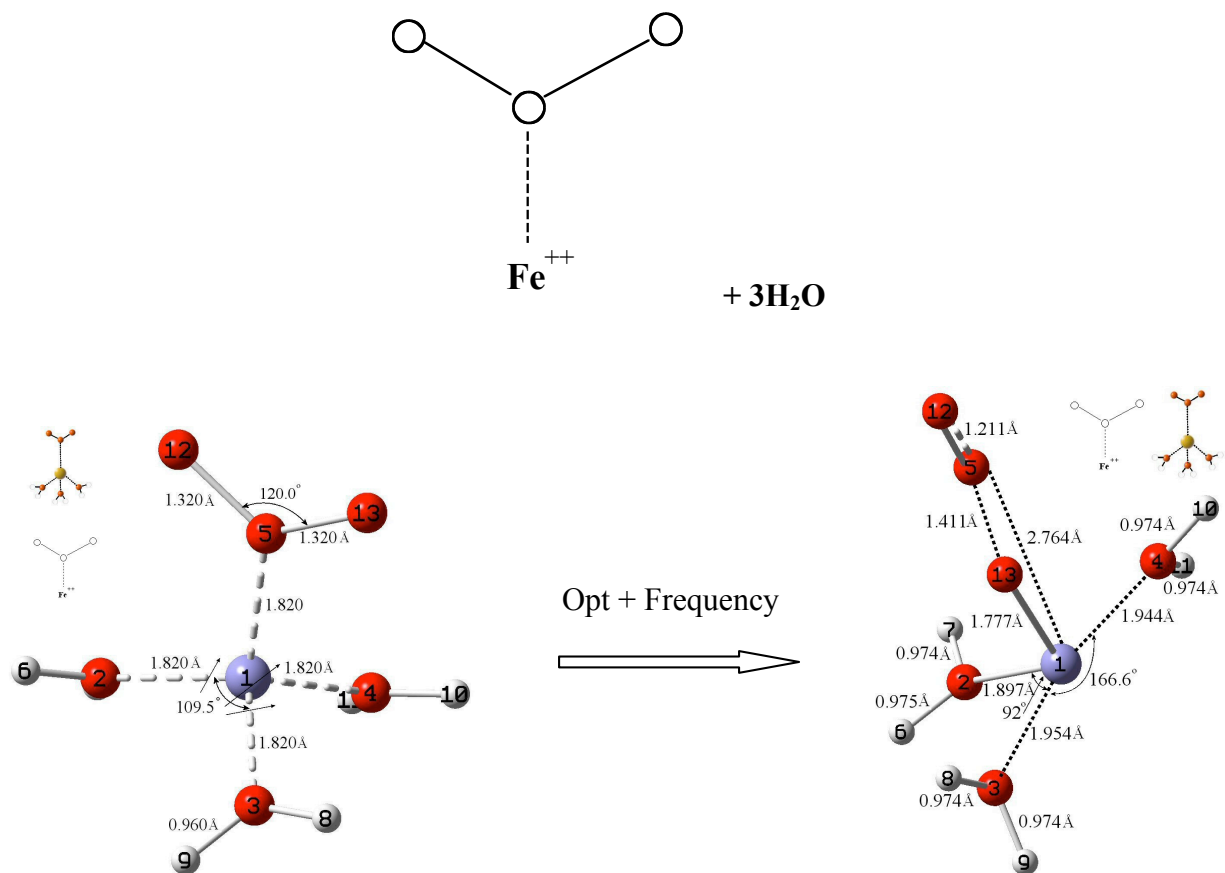
Figure 4(b). Geometry of $[Fe-3(H_2O)-O_3]^{+2}$, for the Ozone approach orientation shown, before and after geometry optimization. The energies of the systems before and after geometry optimization are E_s=-1717.546 a.u. and E_F= -1717.679 a.u., respectively. For optimization in the presence water solvent background, the energies of the systems before and after geometry optimization are E_s=-1717.898 a.u. and E_F= -1717.986 a.u. This optimized state had 0 imaginary frequencies.
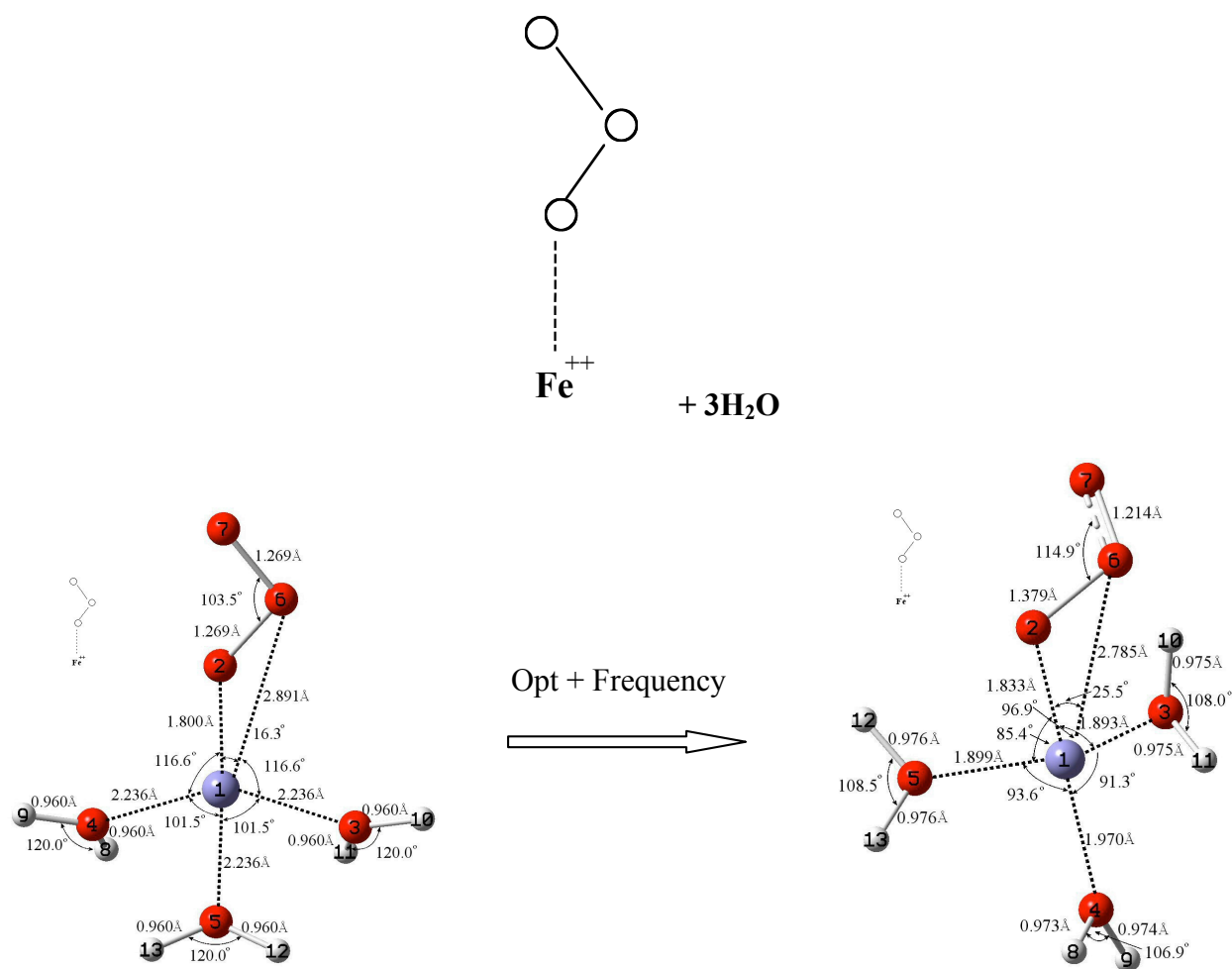
Figure 4(c). Geometry of $[Fe-3(H_2O)-O_3]^{+2}$, for the Ozone approach orientation shown, before and after geometry optimization. The energies of the systems before and after geometry optimization are E_s=-1717.588 a.u. and E_F= -1717.677 a.u., respectively, with 0 imaginary frequencies. For optimization in the presence water solvent background, the energies of the systems before and after geometry optimization are E_s=-1717.921 a.u. and E_F= -1717.024 a.u. This optimized state had 0 imaginary frequencies.
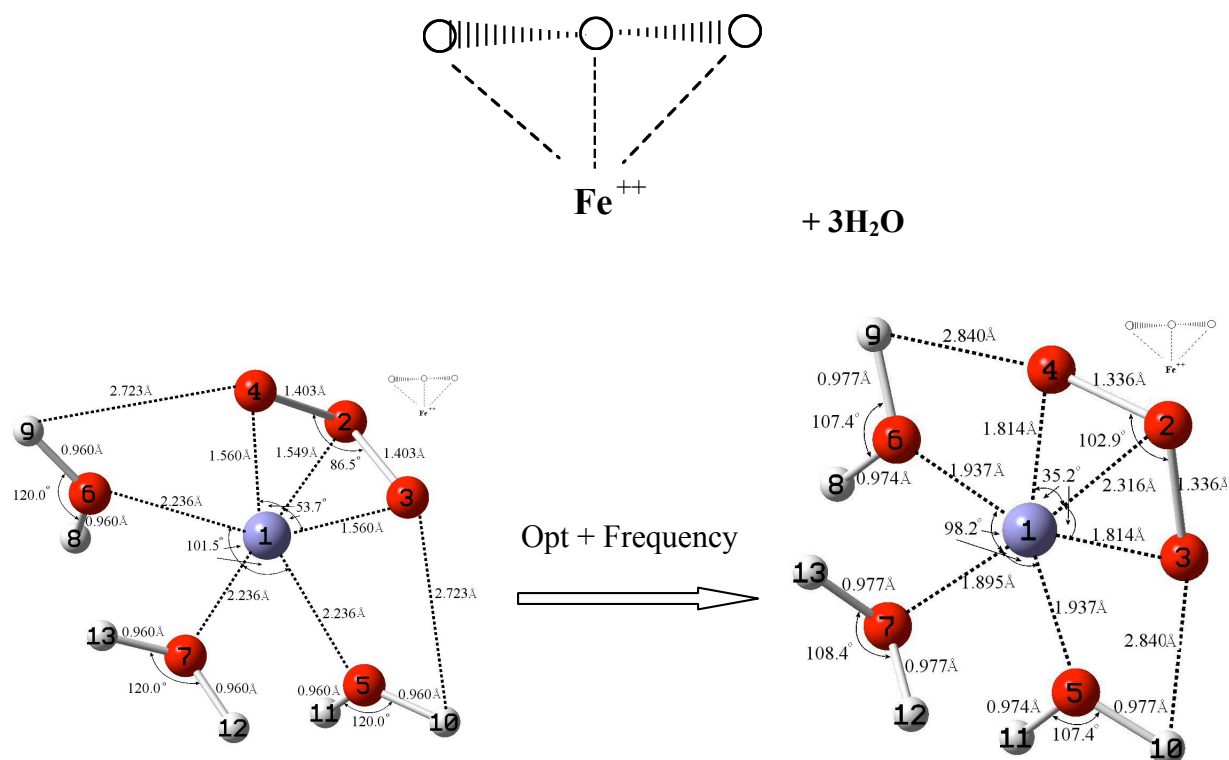
Figure 4(d). Geometry of $[Fe\text{-}3(H_2O)\text{-}O_3]^{+2}$, for the Ozone approach orientation shown, before and after geometry optimization. The energies of the systems before and after geometry optimization are E_s=-1717.483 a.u. and $E_F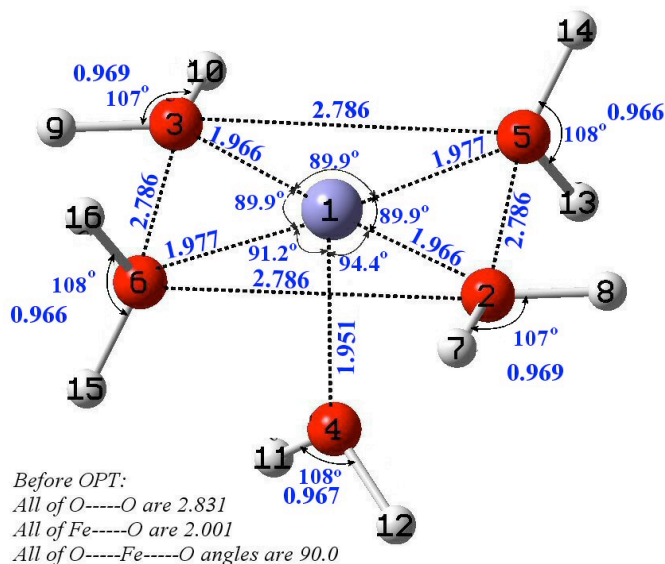$= -1717.707 a.u., respectively, with 1 imaginary frequency. For optimization in the presence water solvent background, the energies of the systems before and after geometry optimization are E_s=-1717.803 a.u. and E_F= -1718.041 a.u. This optimized state had 2 imaginary frequencies.
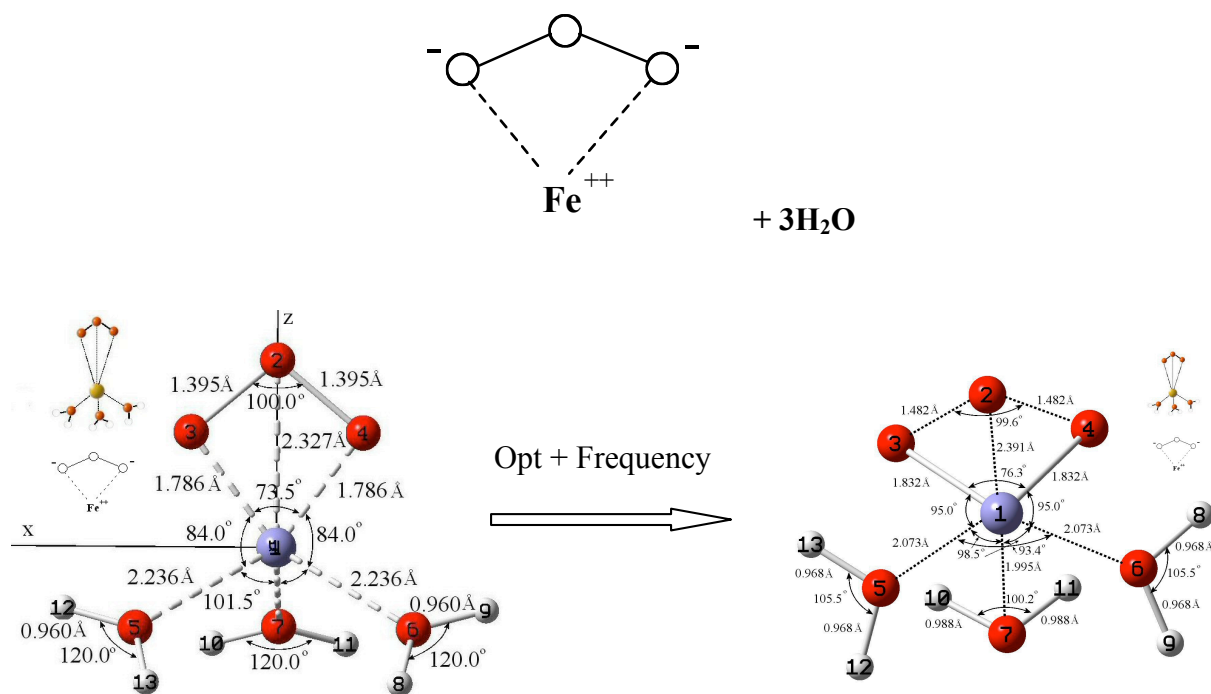
Figure 5(a). Geometry of [Fe 3(H₂O) O₃], for the Ozone approach orientation shown, before and after geometry optimization. The energies of the systems before and after geometry optimization are E_s=-1718.316 a.u. and E_F=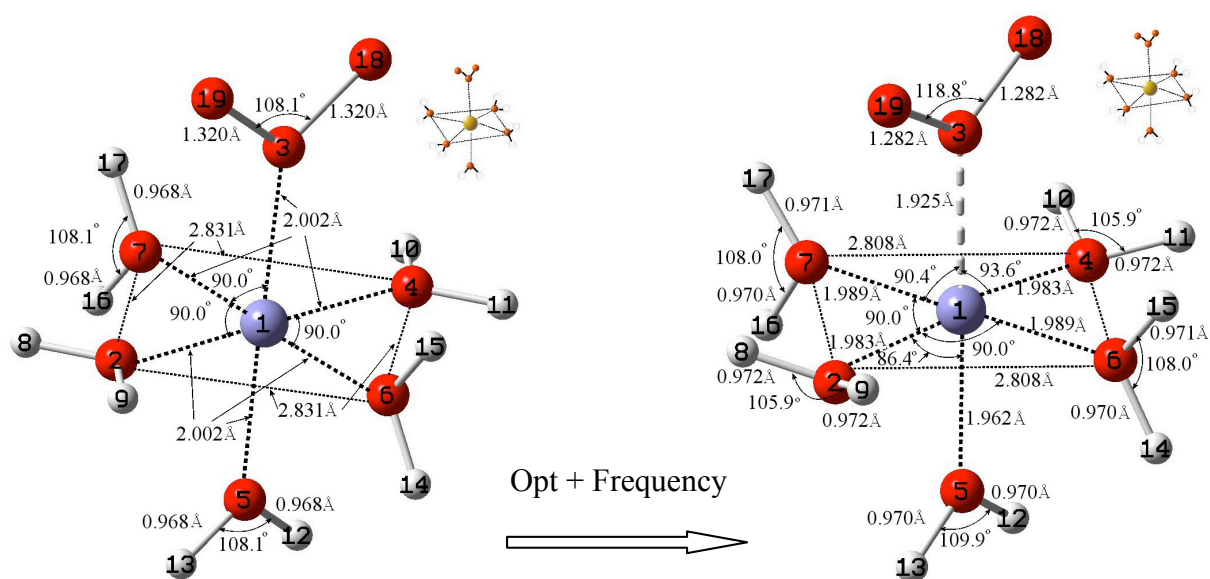 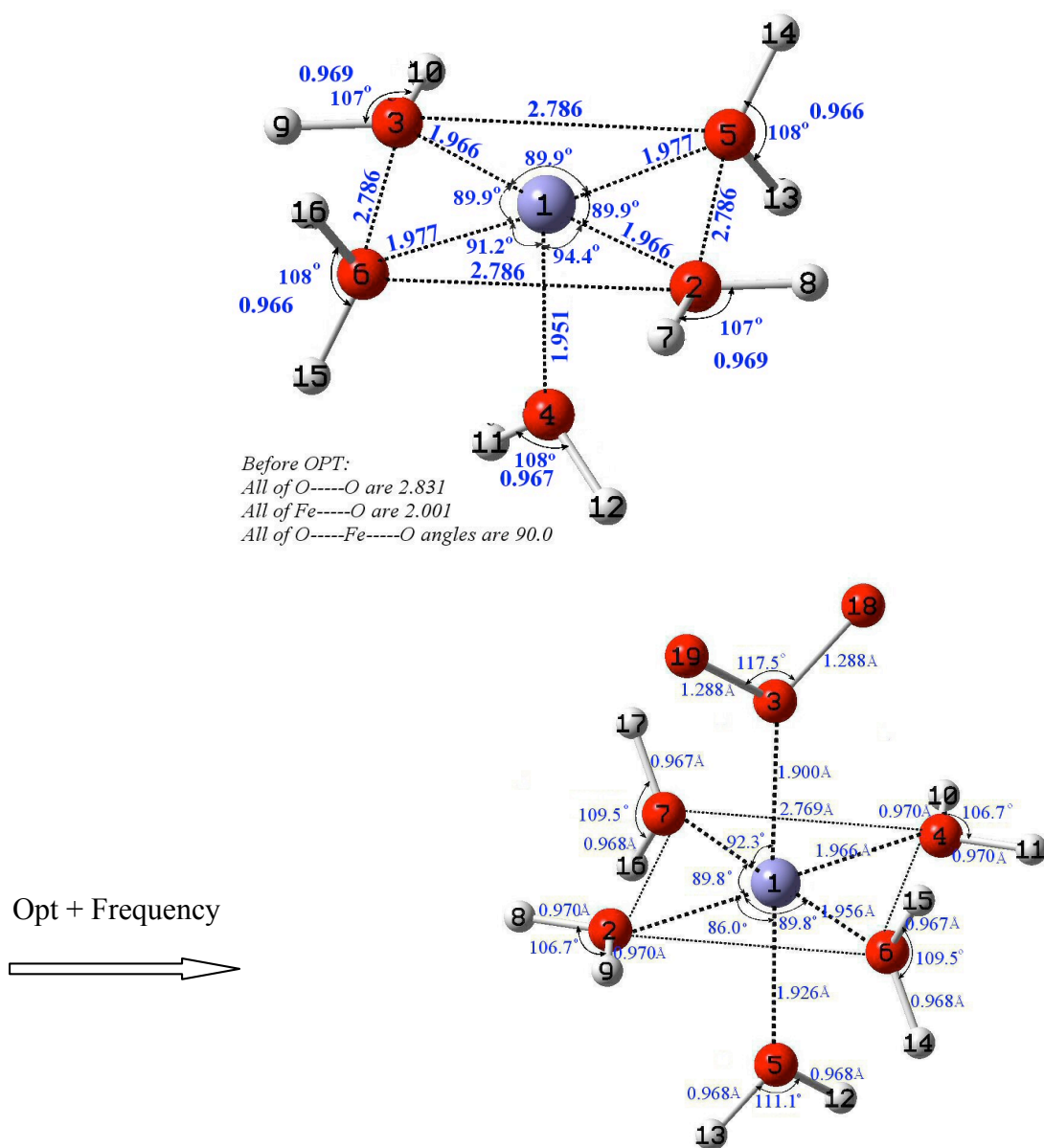-1718.381 a.u., respectively, with 2 imaginary frequencies. For optimization in presence of water solvent background, the energies of the systems before and after geometry optimization are E_s=-1718.366 a.u. and E_F= -1718.417 a.u. This optimized state had 1 imaginary frequency.
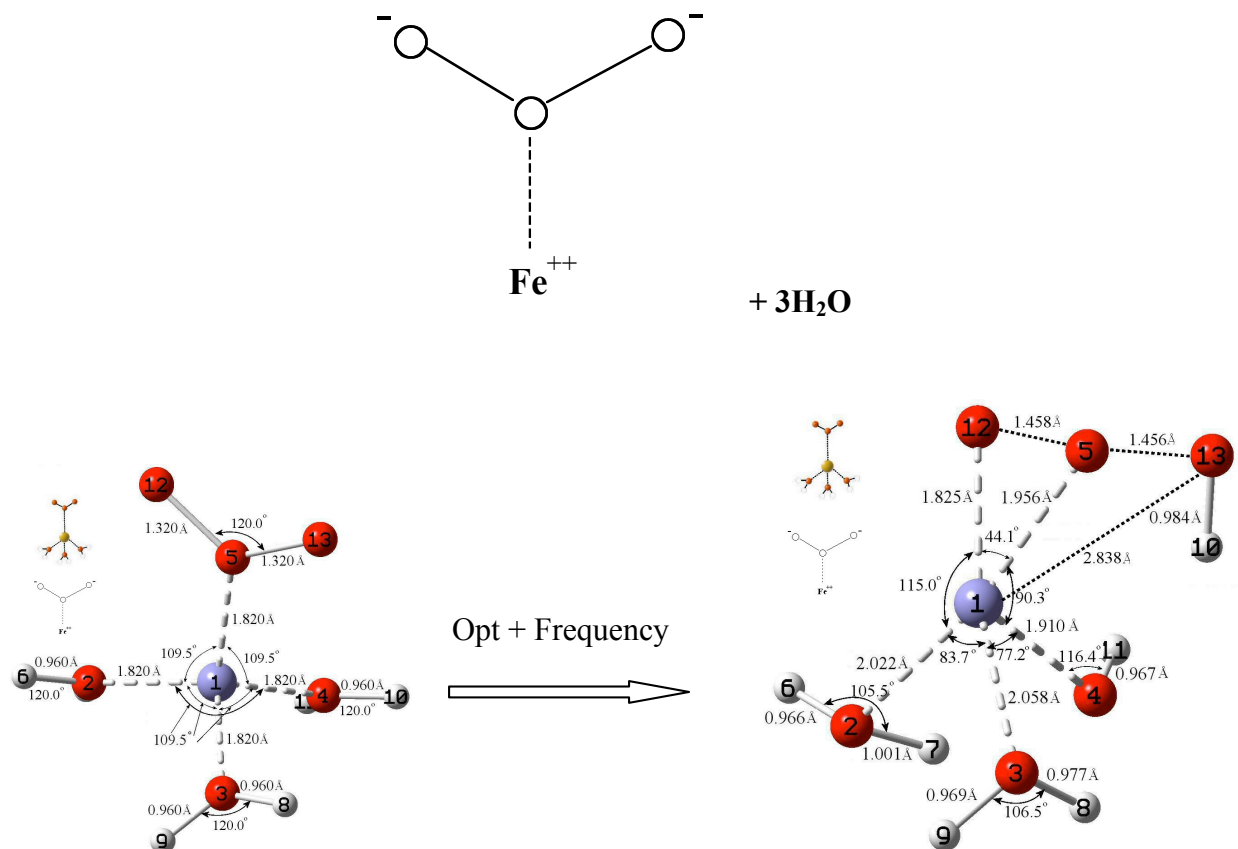
Figure 5(b). Geometry of [Fe 3(H$_2$O) O$_3$], for the Ozone approach orientation shown, before and after geometry optimization. The energies of the systems before and after geometry optimization are E$_s$=-1718.117 a.u. and E$_F$=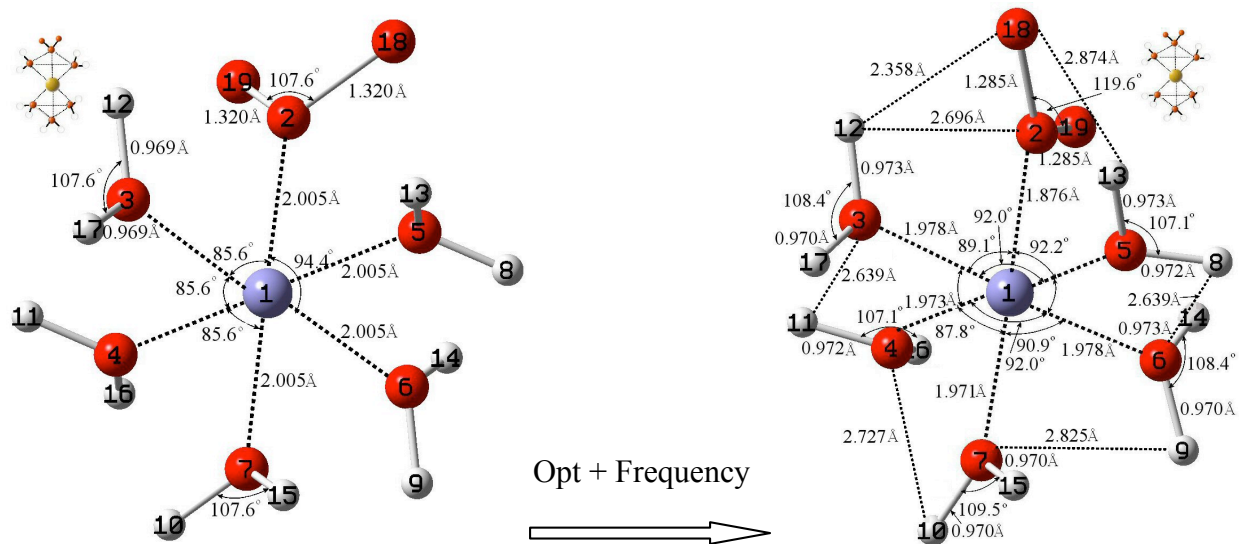 -1718.388 a.u., respectively, with 0 imaginary frequencies. For optimization in presence of water solvent background, the energies of the systems before and after geometry optimization are E$_s$=-1718.198 a.u. and E$_F$= -1718.417 a.u. This optimized state had 0 imaginary frequencies.
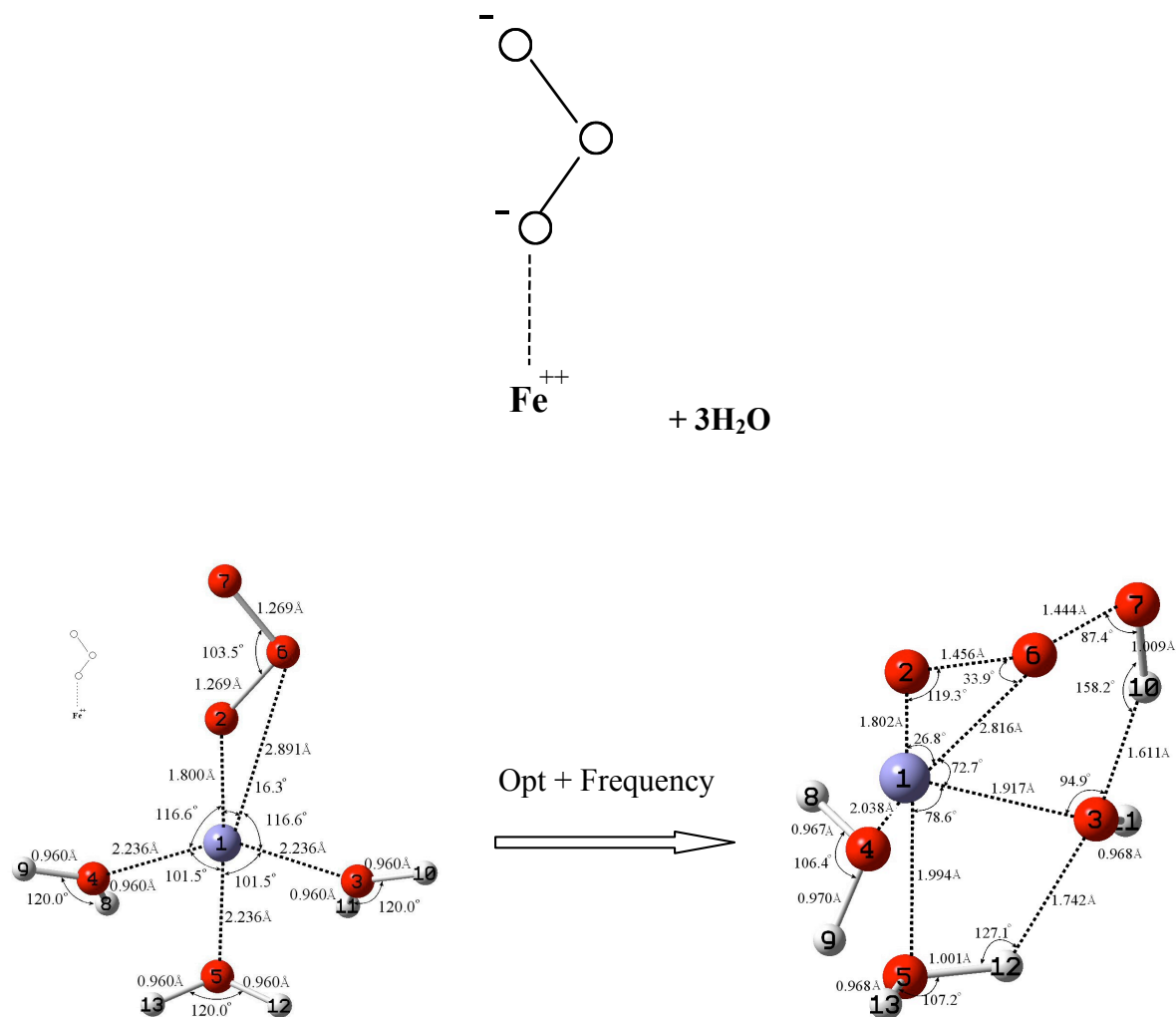
Figure 5(c). Geometry of [Fe 3(H$_2$O) O$_3$], for the Ozone approach orientation shown, before and after geometry optimization. For this geometry sufficient convergence could not be achieved without a water solvent background. The energies of the systems before and after geometry optimization are E$_s$=-1718.268 a.u. and E$_F$= -1718.411 a.u., respectively, with 0 imaginary frequencies.
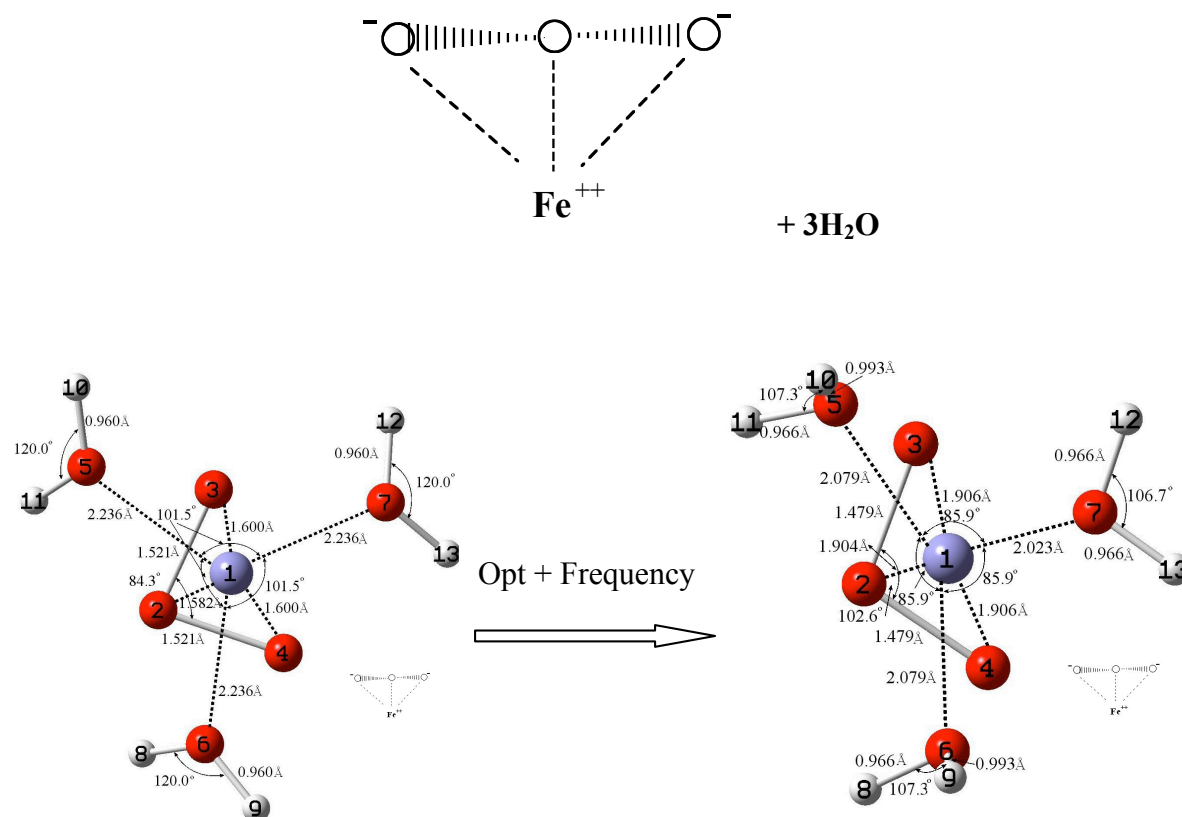
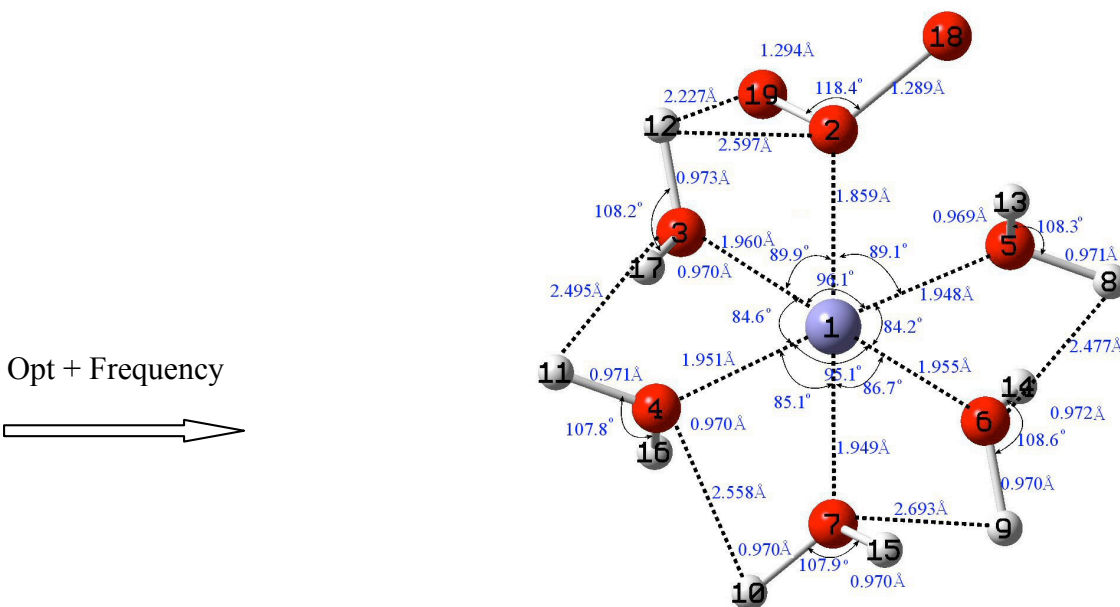**Figure 5(d)**. Geometry of [Fe 3(H_2O) O_3], for the Ozone approach orientation shown, before and after geometry optimization. The energies of the systems before and after geometry optimization are E_s=-1718.197 a.u. and E_F= -1718.80 a.u., respectively, with 1 imaginary frequency. For optimization in presence of a water solvent background, the energies of the systems before and after geometry optimization are E_s=-1718.234 a.u. and E_F= -1718.412 a.u. This optimized state had 1 imaginary frequencies.
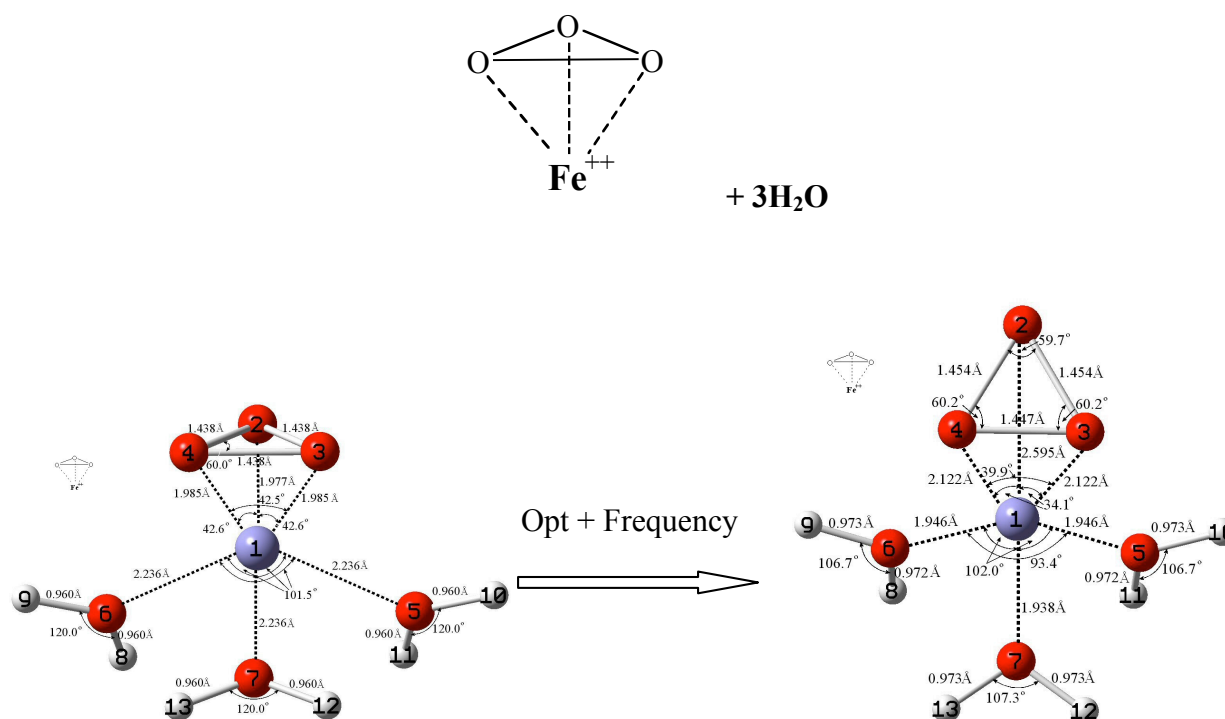
Figure 6. Geometry of $[Fe-3(H_2O)-O_3]^{+2}$, for the orientation of cyclic Ozone shown, before and after geometry optimization. The energies of the systems before and after geometry optimization are E_s=-1717.536 a.u. and E_F= -1717.599 a.u., respectively, with 2 imaginary frequencies. For optimization in the presence of a water solvent background, the energies of the systems before and after geometry optimization are E_s=-1717.852 a.u. and E_F= -1717.940 a.u. This optimized state had 2 imaginary frequencies.
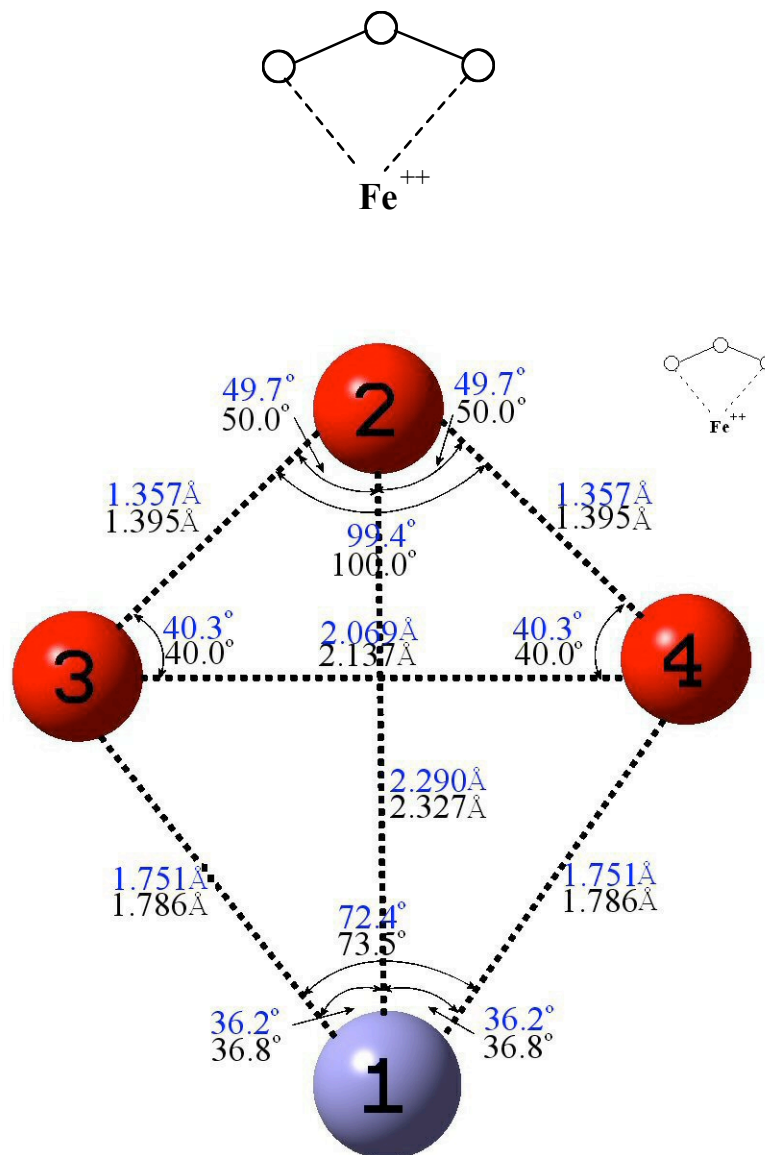
Figure 7(a). Geometry of $[Fe-O_3]^{+2}$, for the orientation of Ozone shown and in presence of a water solvent background, before (black) and after (blue) geometry optimization. The energies of the complexes before and after geometry optimization are E_s=-1488.569 a.u. and E_F= -1488.572 a.u., respectively. This optimized state had 0 imaginary frequencies.
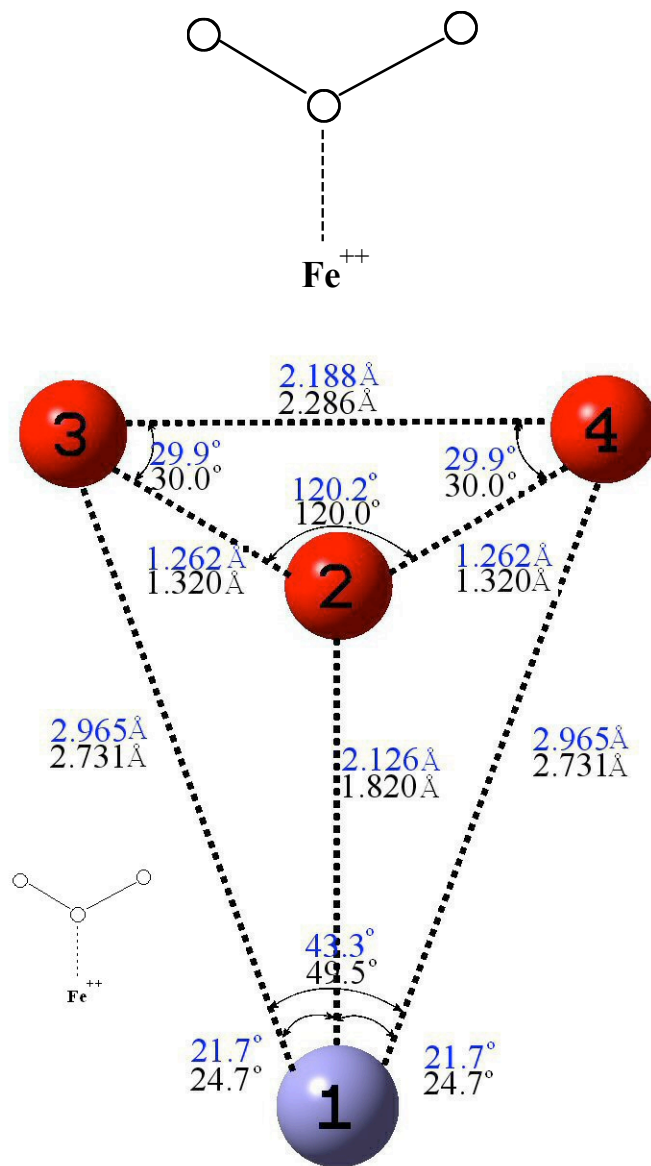
Figure 7(b). Geometry of $[Fe-O_3]^{+2}$, for the orientation of Ozone shown and in presence of a water solvent background, before (black) and after (blue) geometry optimization. The energies of the complexes before and after geometry optimization are E_s=-1488.540 a.u. and E_F= -1488.549 a.u., respectively. This optimized state had 0 imaginary frequencies.
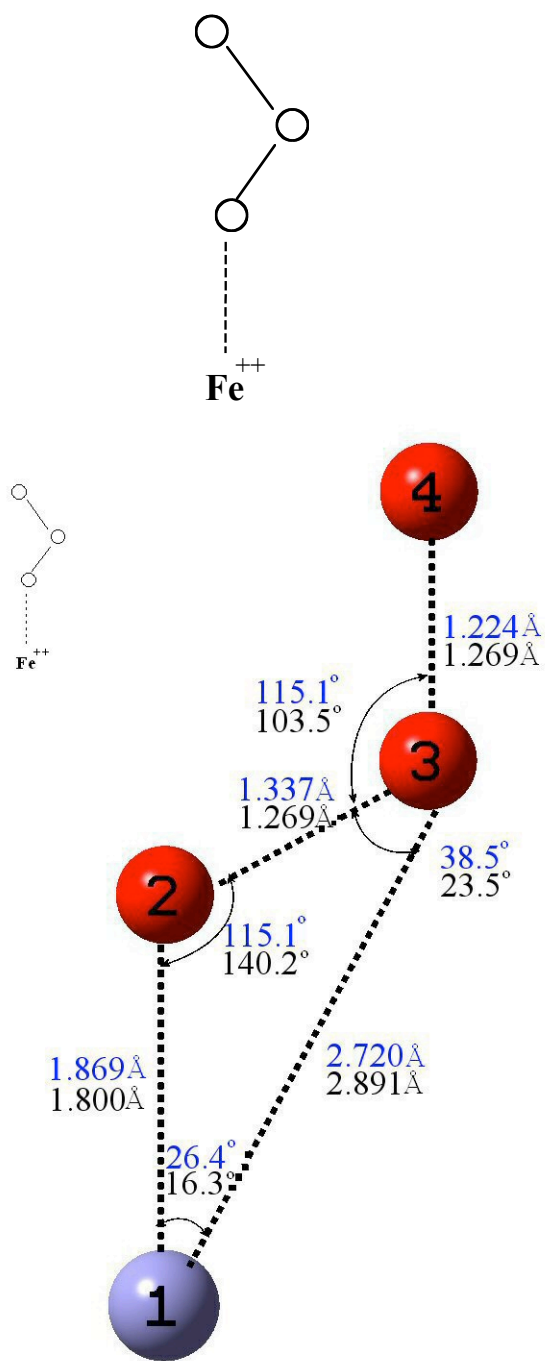
Figure 7(c). Geometry of $[Fe\text{-}O_3]^{+2}$, for the orientation of Ozone shown and in presence of a water solvent background, before (black) and after (blue) geometry optimization. The energies of the complexes before and after geometry optimization are E_s=-1488.565 a.u. and E_F= -1488.588 a.u., respectively. This optimized state had 0 imaginary frequencies.
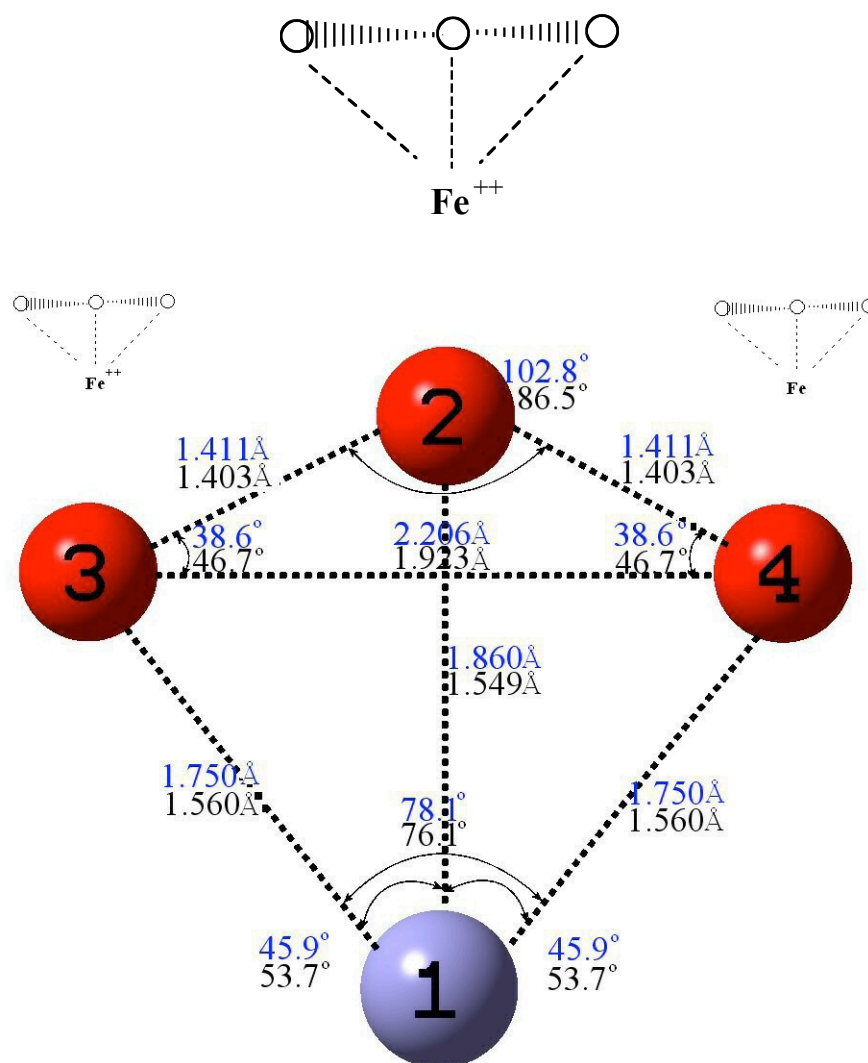
Figure 7(d). Geometry of $[Fe\text{-}O_3]^{+2}$, for the orientation of Ozone shown and in presence of a water solvent background, before (black) and after (blue) geometry optimization. The energies of the complexes before and after geometry optimization are E_s=-1488.429 a.u. and E_F= -1488.548 a.u., respectively. This optimized state had 0 imaginary frequencies.
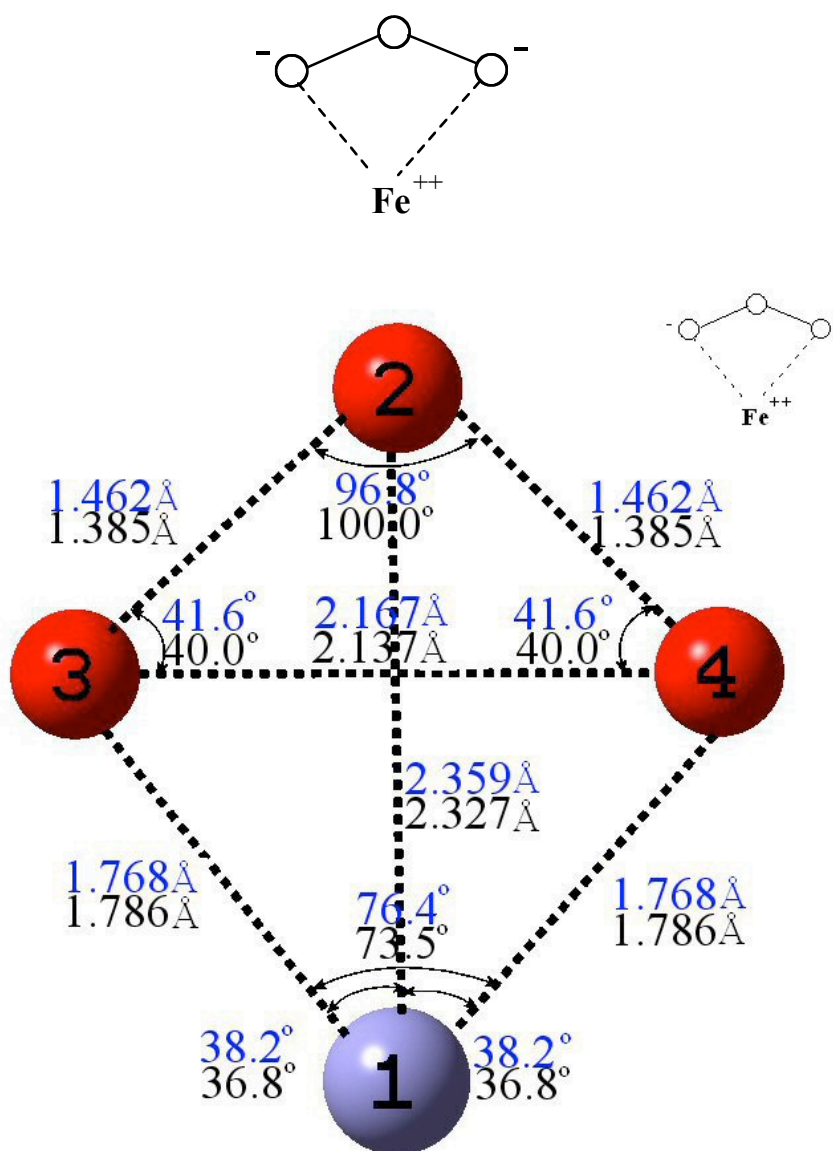
Figure 8(a). Geometry of [Fe-O$_3$], which has zero net charge, for the orientation of Ozone shown and in presence of a water solvent background, before (black) and after (blue) geometry optimization. The energies of the complexes before and after geometry optimization are E$_s$=-1489.015 a.u. and E$_F$= -1489.020 a.u., respectively. This optimized state had 0 imaginary frequencies.
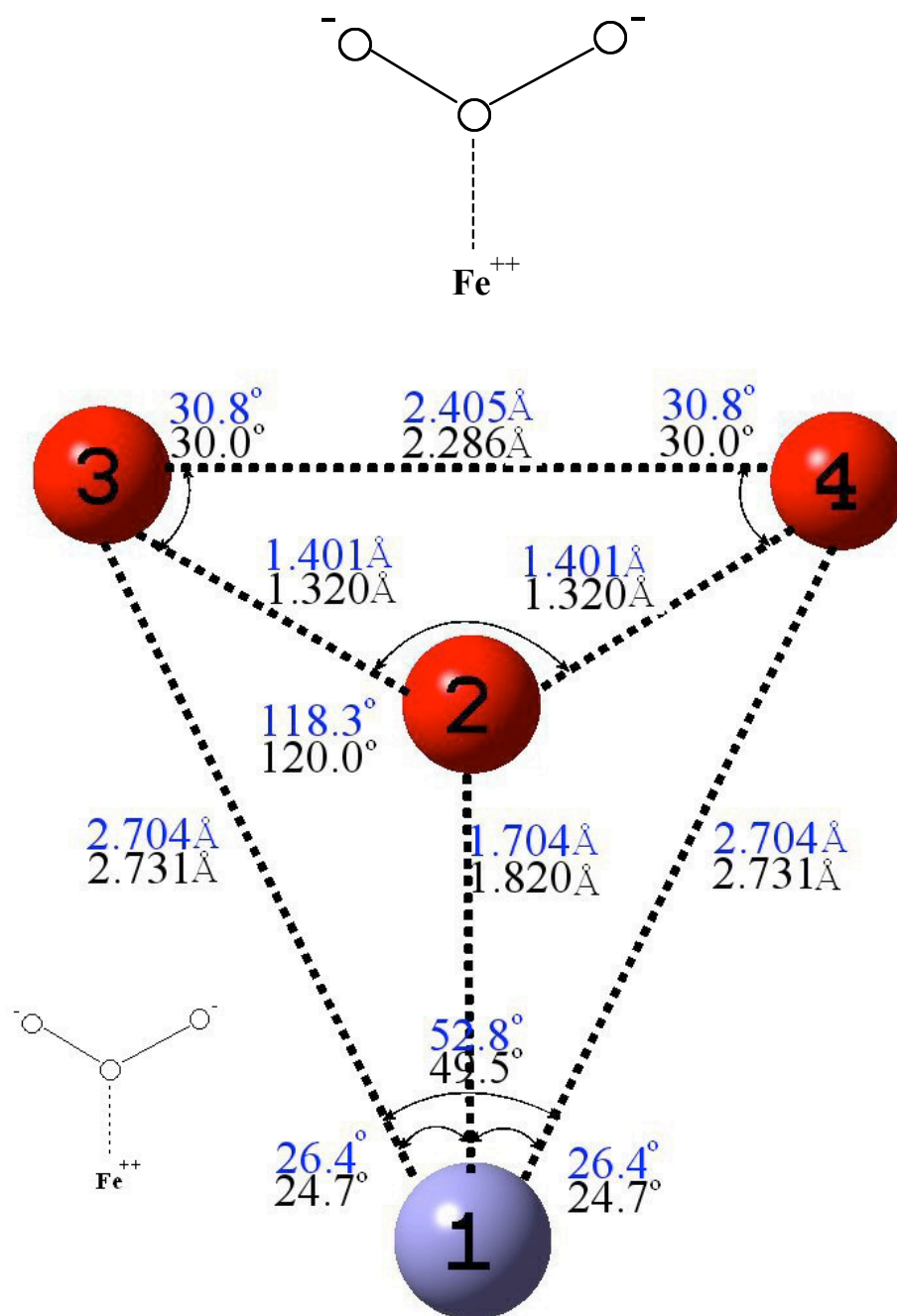
Figure 8(b). Geometry of [Fe-O$_3$], which has zero net charge, for the orientation of Ozone shown and in presence of a water solvent background, before (black) and after (blue) geometry optimization. The energies of the complexes before and after geometry optimization are E$_s$=-1488.909 a.u. and E$_F$= -1488.922 a.u., respectively. This optimized state had 2 imaginary frequencies.
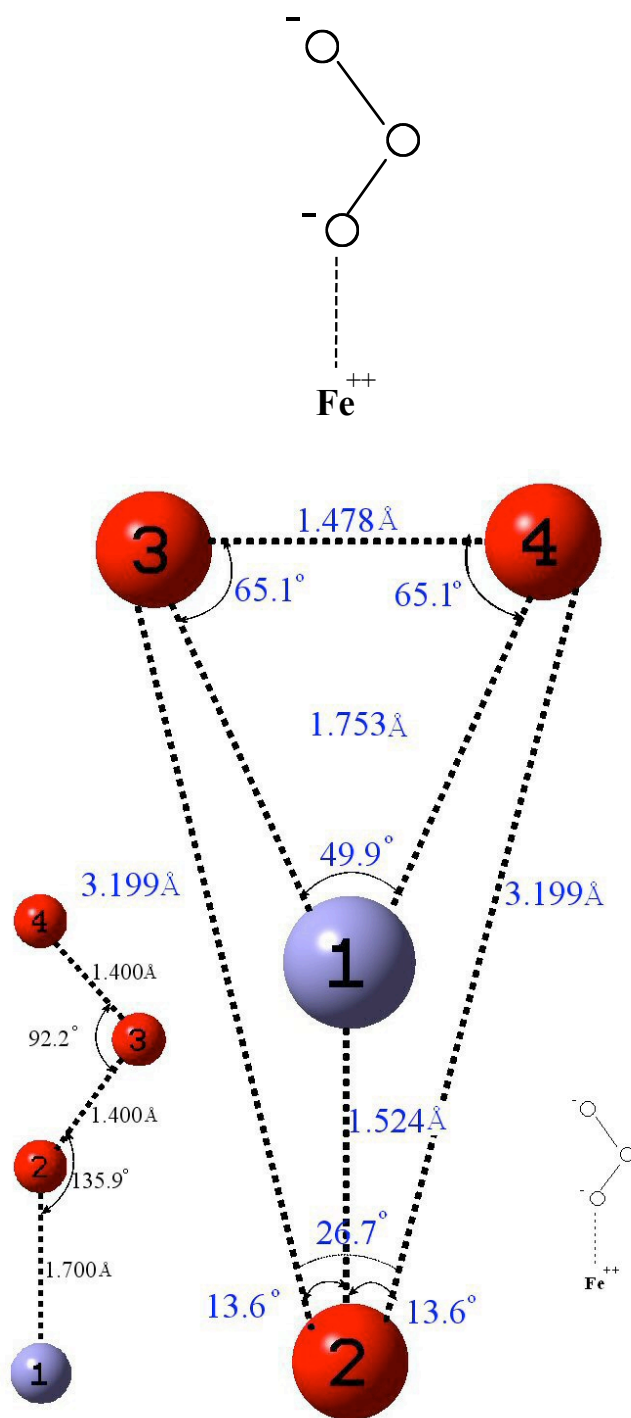
Figure 8(c). Geometry of [Fe-O$_3$], which has zero net charge, for the orientation of Ozone shown and in presence of a water solvent background, before (black) and after (blue) geometry optimization. The energies of the complexes before and after geometry optimization are E$_s$=-1489.054 a.u. and E$_F$= -1489.059 a.u., respectively. This optimized state had 0 imaginary frequencies.
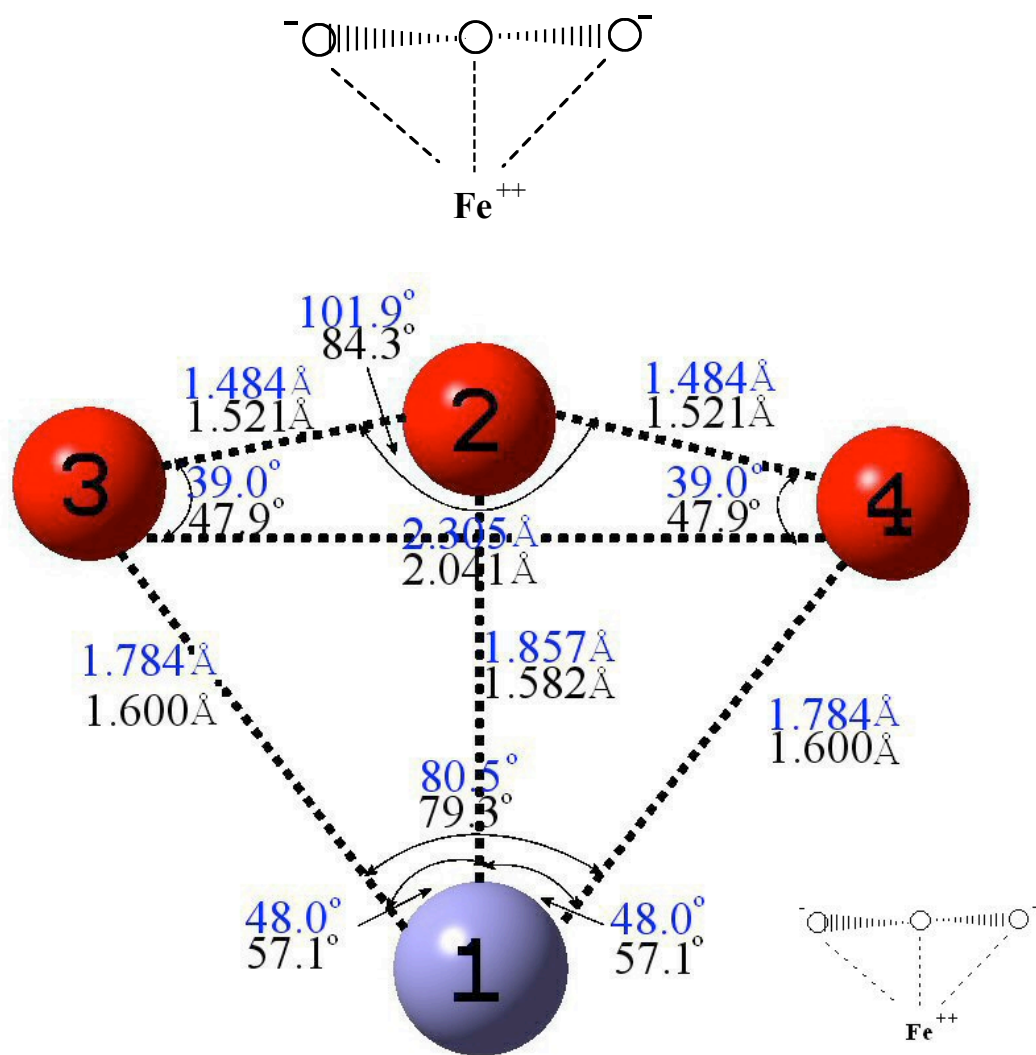
Figure 8(d). Geometry of [Fe-O$_3$], which has zero net charge, for the orientation of Ozone shown and in presence of a water solvent background, before (black) and after (blue) geometry optimization. The energies of the complexes before and after geometry optimization are E$_s$=-1488.868 a.u. and E$_F$= -1488.973 a.u., respectively. This optimized state had 0 imaginary frequencies.
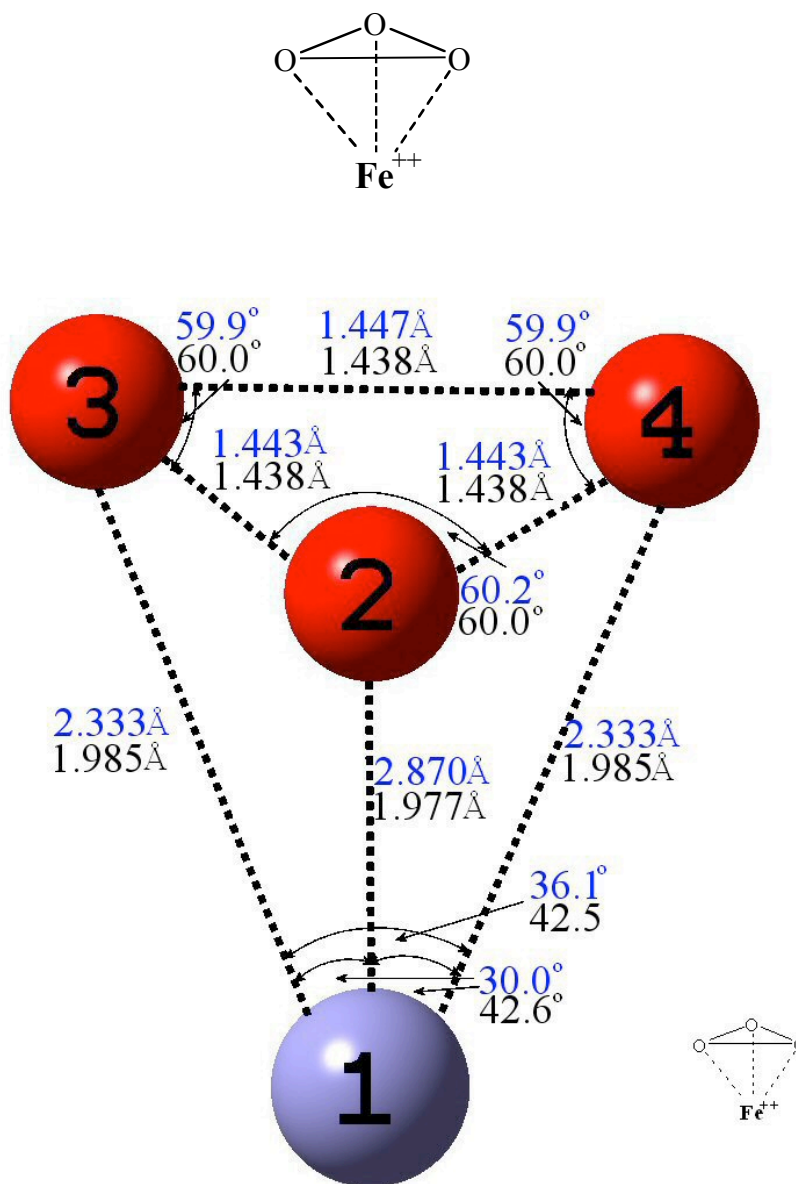
Figure 9. Geometry of [Fe-O$_3$]$^{+2}$, which has net charge +2, for the orientation of cyclic Ozone shown and in presence of a water solvent background, before (black) and after (blue) geometry optimization. The energies of the complexes before and after geometry optimization are E$_s$=-1488.482 a.u. and E$_F$= -1488.507 a.u., respectively. This optimized state had 1 imaginary frequency.
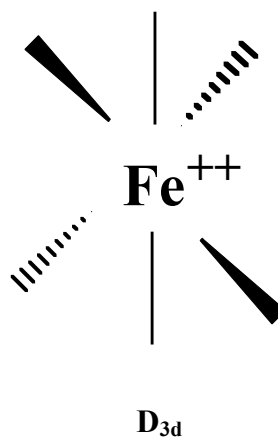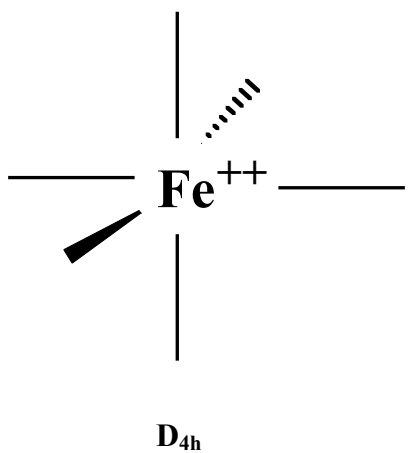
Figure 10. Schematic representation of two symmetries of $[Fe(H_2O)^6]^{+2}$ complex, which are associated with symmetry groups D_{4h} and D_{3d} [29,30].
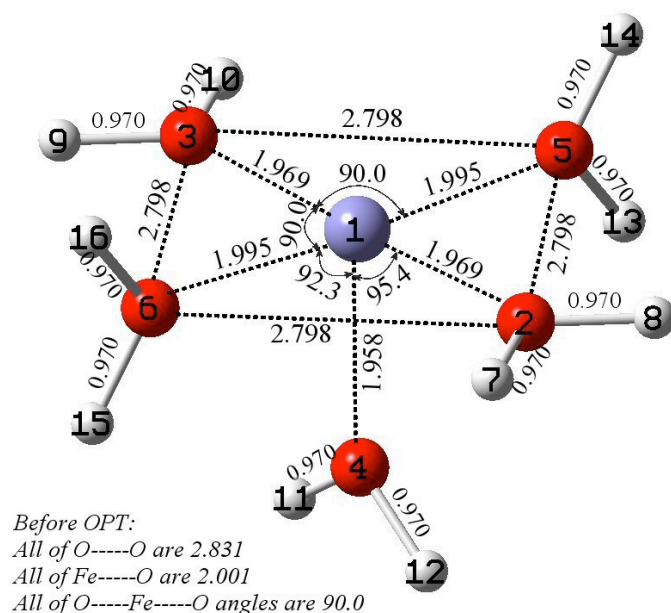
Figure 11(a). Geometry of complex $[Fe(H_2O)_5]^{+2}$ D_{4h}, without Ozone, before and after geometry optimization. The energies of the complexes before and after geometry optimization are E_s=-1645.203 a.u. and E_F= -1645.205 a.u., respectively, with 2 imaginary frequencies.

Figure 11(b). Geometry of complex $[Fe(H_2O)_5]^{+2}$ D_{4h}, without Ozone and in presence of a water solvent background, before and after geometry optimization. The energies of the complexes before and after geometry optimization are E_s=-1645.506 a.u. and E_F= -1645.510 a.u., respectively, with 3 imaginary frequencies.

Figure 12(a). Geometry of complex $[Fe(H_2O)_5O_3]^{+2}$ D_{4h}, before and after geometry optimization. The energies of the complexes before and after geometry optimization are E_s=-1870.614 a.u. and E_F= -1870.630 a.u., respectively, with 2 imaginary frequencies.

Figure 12(b). Geometry of complex $[Fe(H_2O)_5O_3]^{+2}$ D_{4h}, in presence of a water solvent background, before and after geometry optimization. The energies of the complexes before and after geometry optimization are E_s=-1870.912 a.u. and E_F= -1870.930 a.u., respectively, with 5 imaginary frequencies.

Figure 13(a). Geometry of complex $[Fe(H_2O)_5]^{+2}$ D_{3d}, without Ozone, before (black) and after (blue) geometry optimization. The energies of the complexes before and after geometry optimization are E_s=-1645.201 a.u. and E_F= -1645.205 a.u., respectively, with 0 imaginary frequencies.

Figure 13(b). Geometry of complex $[Fe(H_2O)_5]^{+2}$ D_{4h}, without Ozone and in presence of a water solvent background, after geometry optimization. The energies of the complexes before and after geometry optimization are E_s=-1645.508 a.u. and E_F= -1645.514 a.u., respectively, with 0 imaginary frequencies.

Figure 14(a). Geometry of complex $[Fe(H_2O)_5O_3]^{+2}$ D_{3d}, before and after geometry optimization. The energies of the complexes before and after geometry optimization are E_s=-1870.608 a.u. and E_F= -1870.638 a.u., respectively, with 0 imaginary frequencies.

Figure 14(b). Geometry of complex $[Fe(H_2O)_5O_3]^{+2}$ D_{3d}, in presence of a water solvent background, after geometry optimization. The energies of the complexes before and after geometry optimization are E_s=-1870.907 a.u. and E_F= -1870.937 a.u., respectively, with 0 imaginary frequencies.
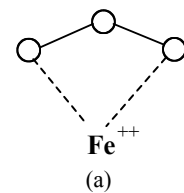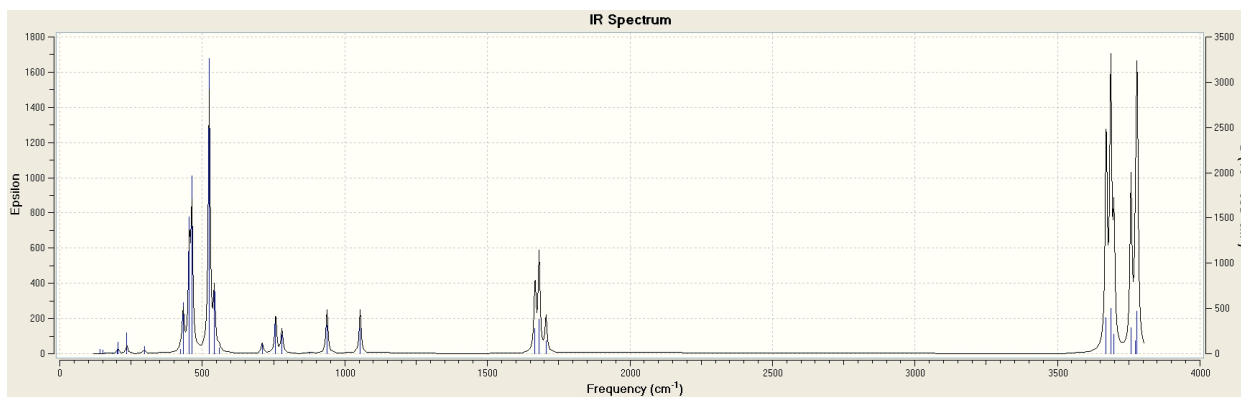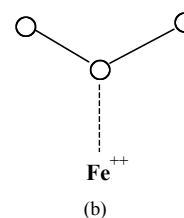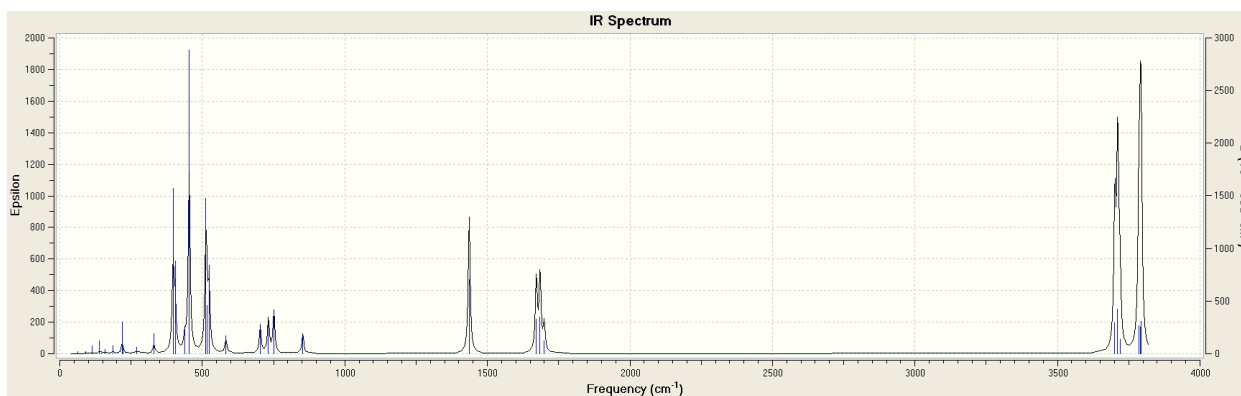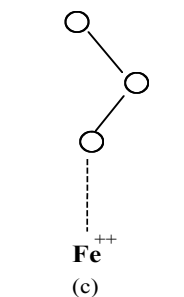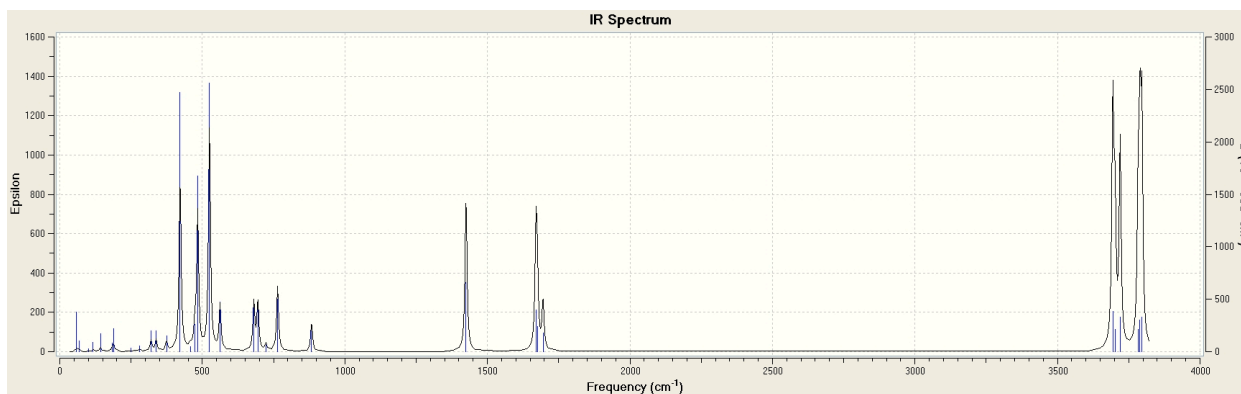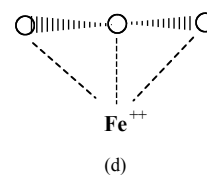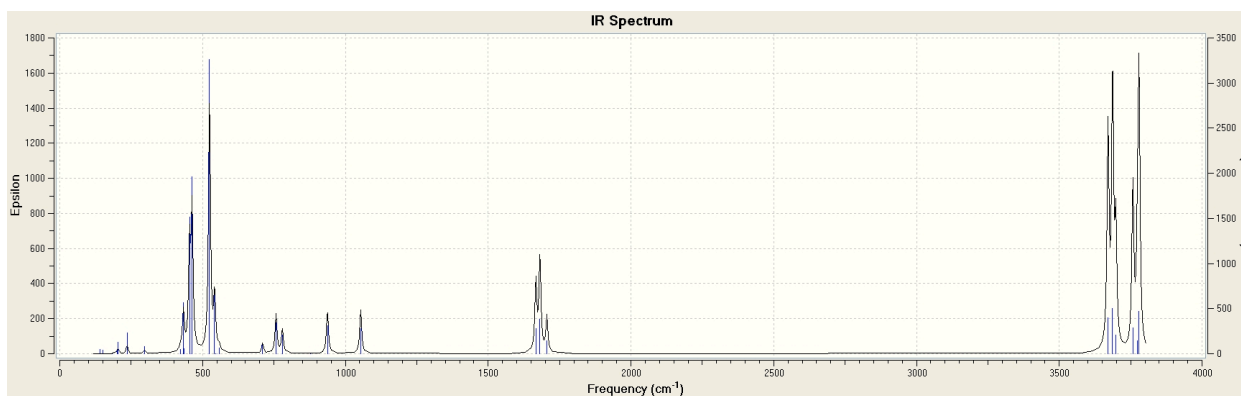
Figure 15. IR spectra for [Fe-3(H$_2$O)-O$_3$]$^{+2}$, which has net charge +2, for different approaches of Ozone.
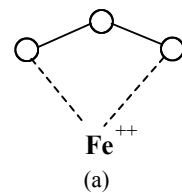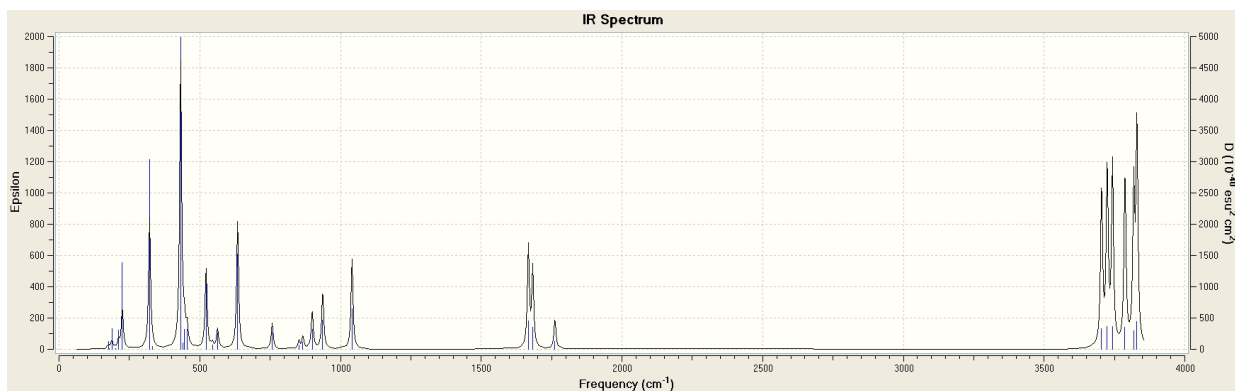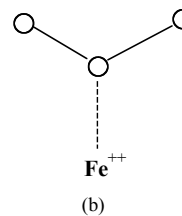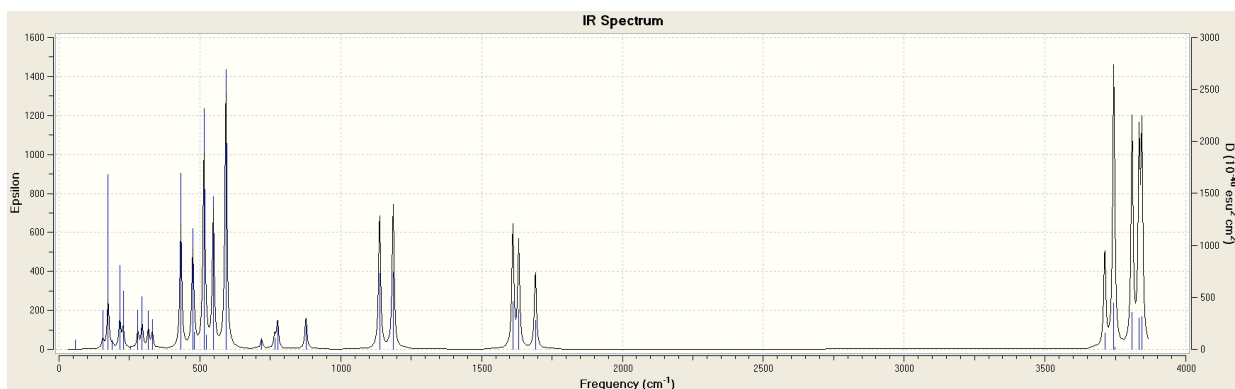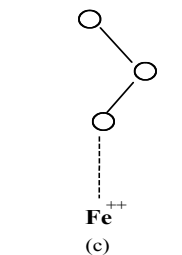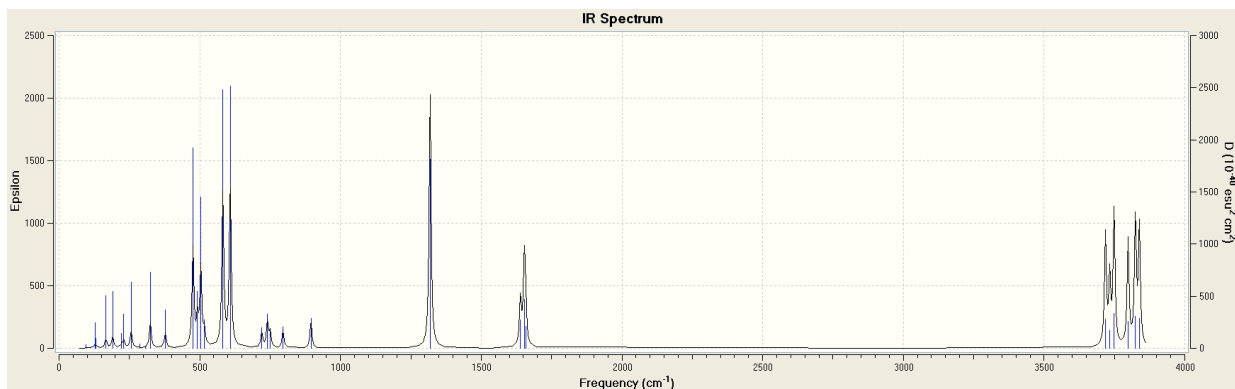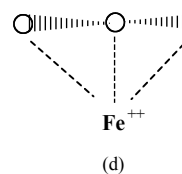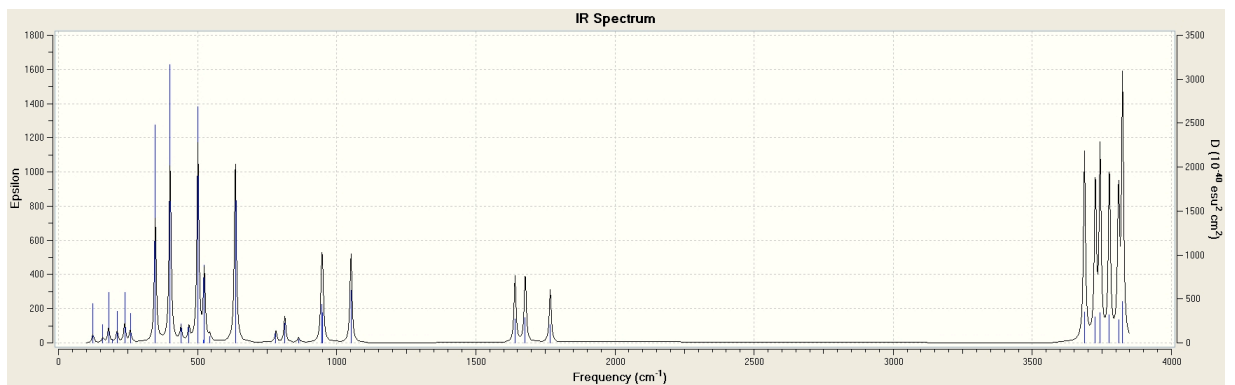
Figure 16. IR spectra for $[Fe\text{-}3(H_2O)\text{-}O_3]^{+2}$, which has net charge +2, in presence of a water solvent background, for different approaches of Ozone.
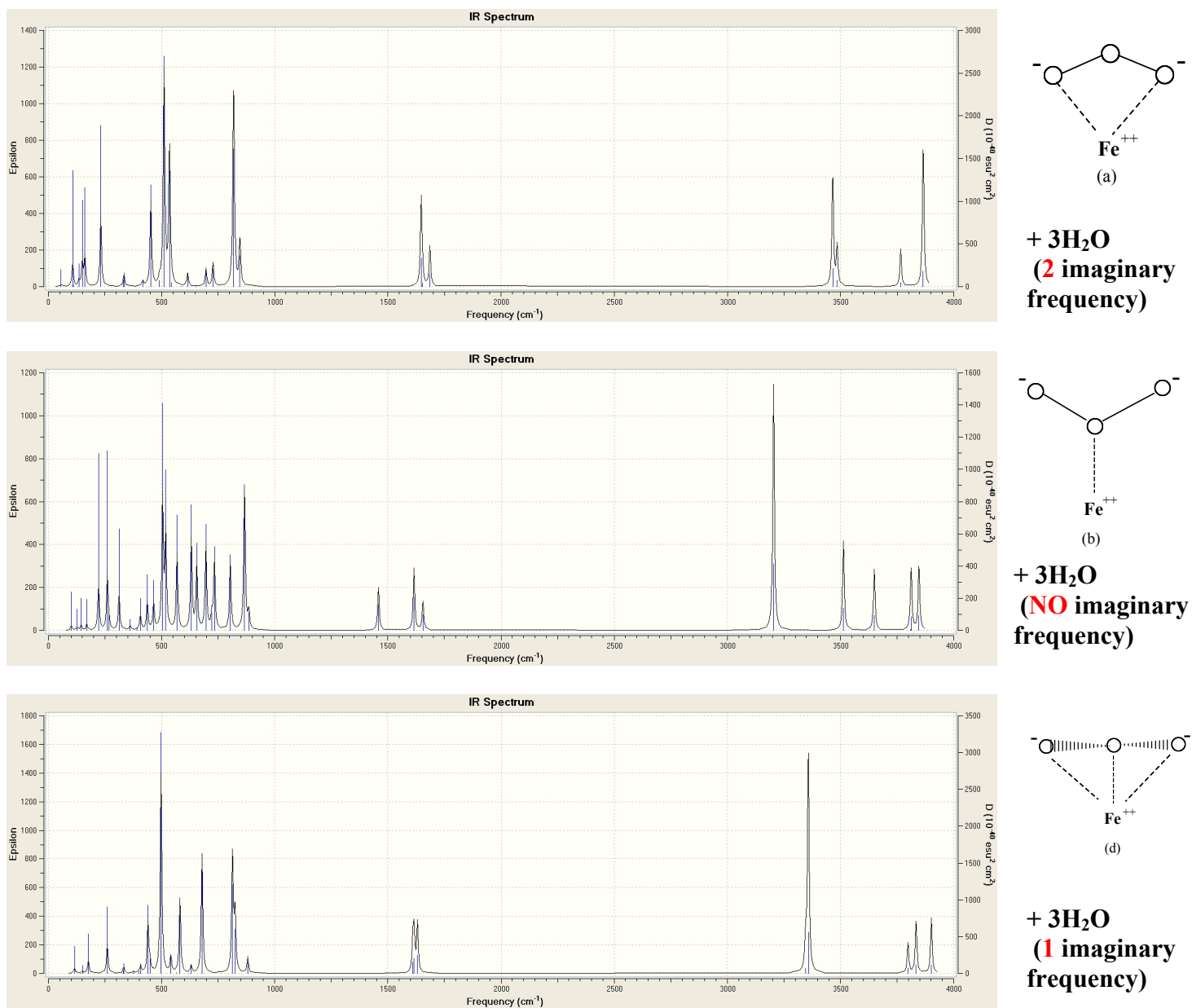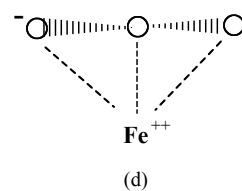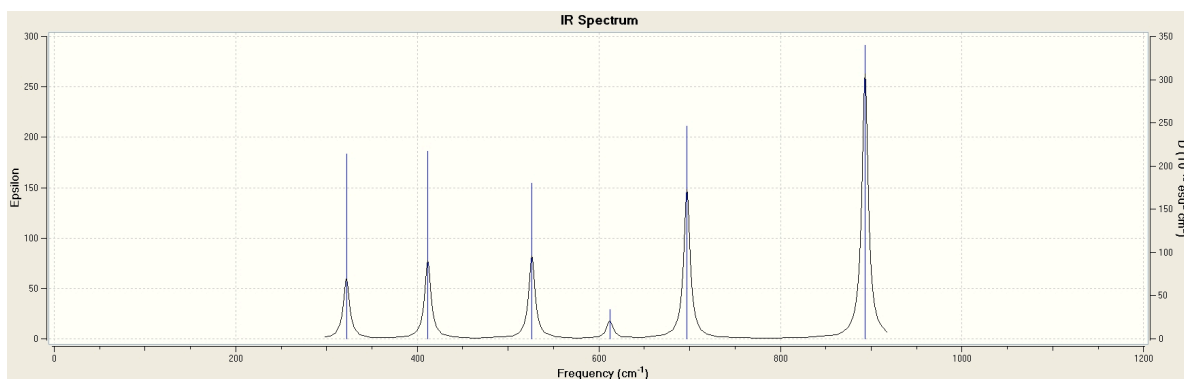
Figure 17. IR spectra for [Fe-3(H_2O)-O_3], which has 0 net charge, for different approaches of Ozone.
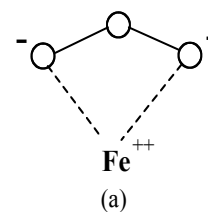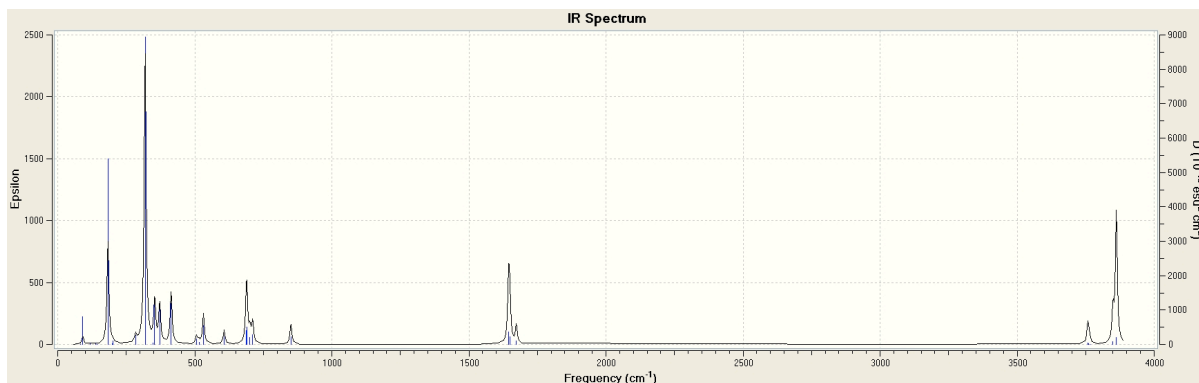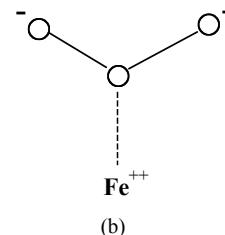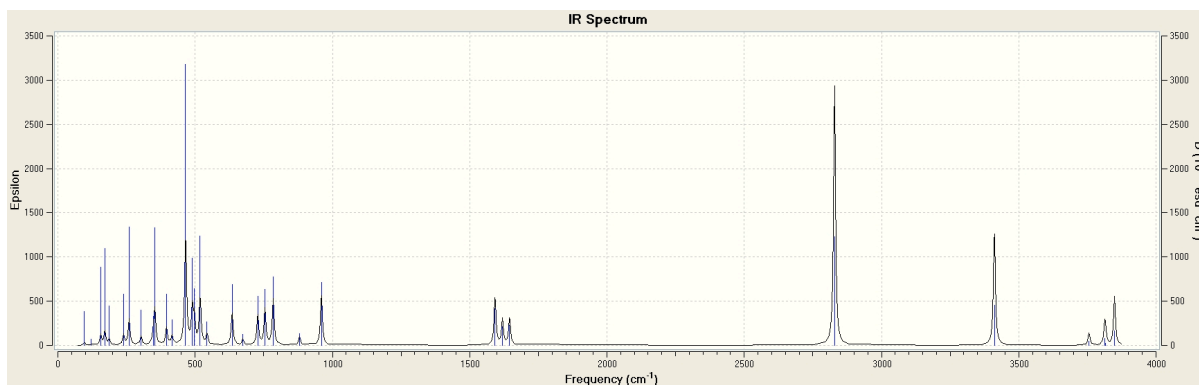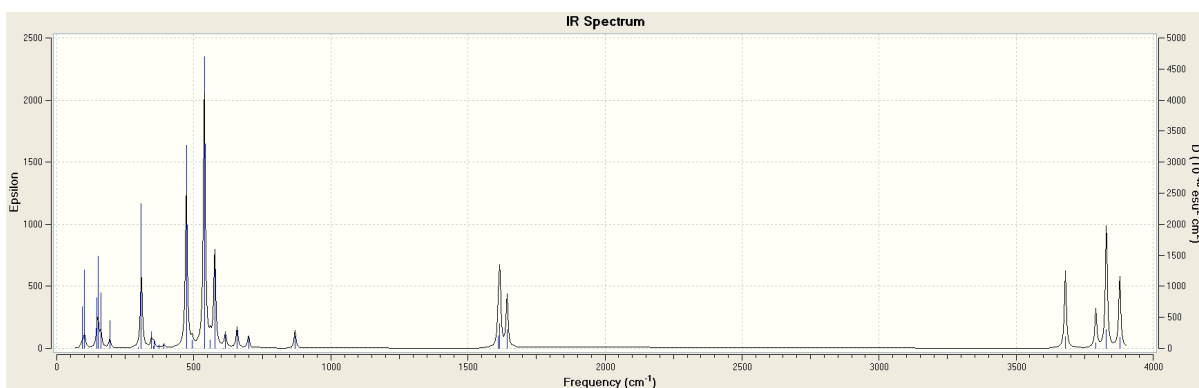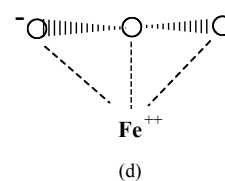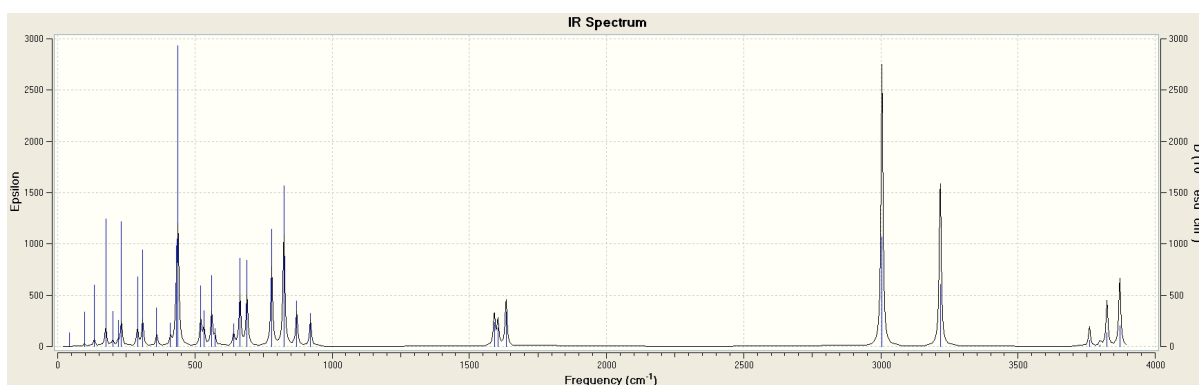
Figure 18. IR spectra for [Fe-3(H₂O)-O₃], which has 0 net charge, in presence of a water solvent background, for different approaches of Ozone.
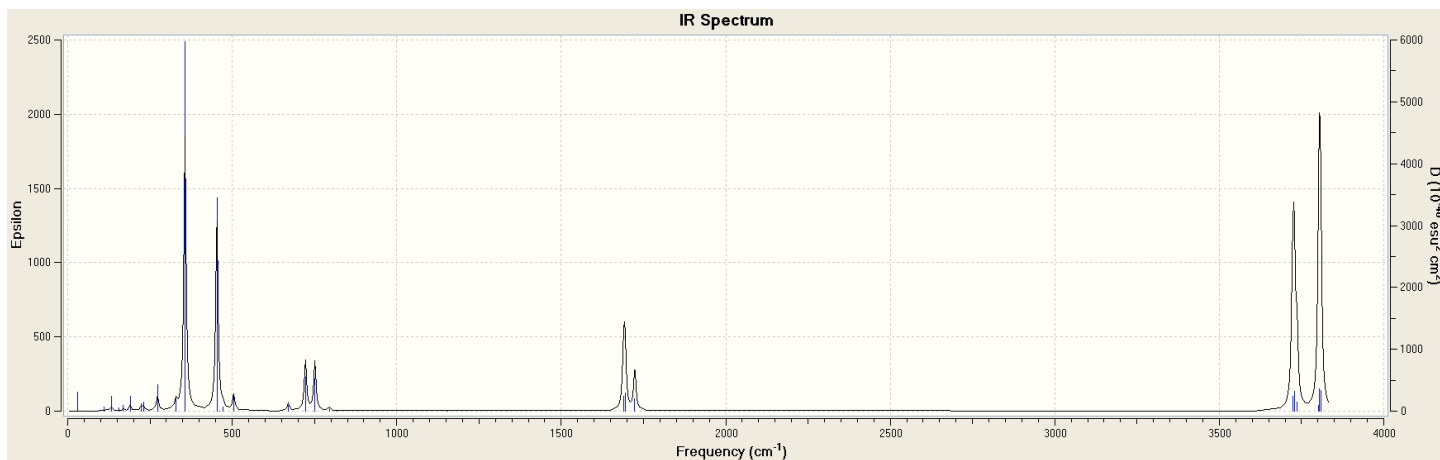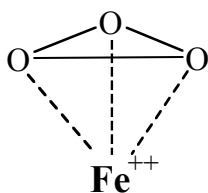
Figure 19. IR spectra for [Fe-3(H$_2$O)-O$_3$]$^{+2}$, for approach of cyclic Ozone (see Fig. 6), (2 imaginary frequencies).
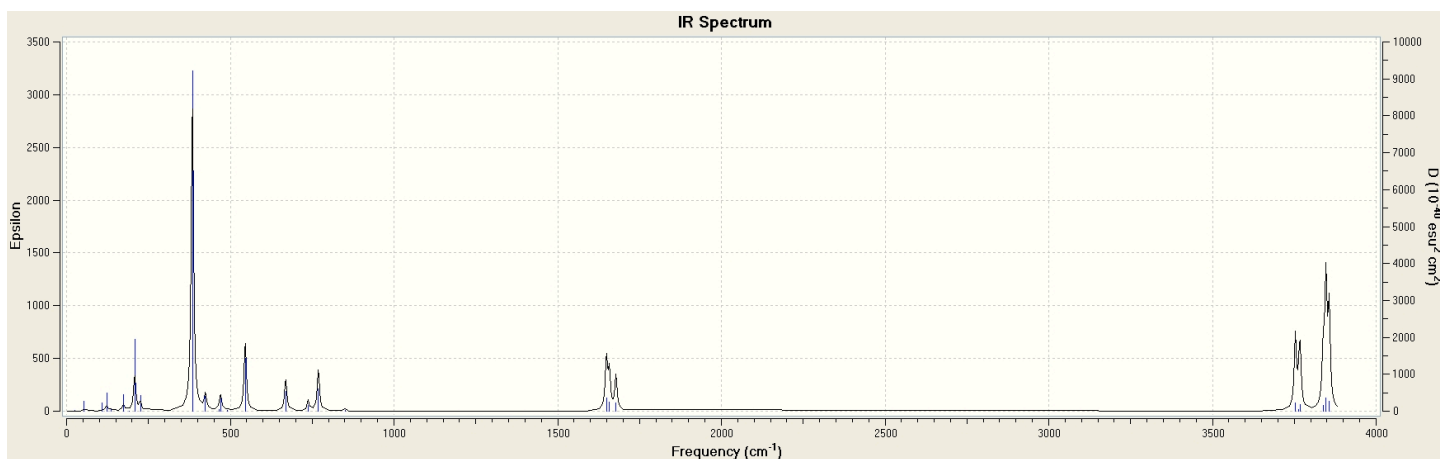
Figure 20. IR spectra for [Fe-3(H$_2$O)-O$_3$]$^{+2}$, for approach of cyclic Ozone, in presence of a water solvent background, (2 imaginary frequencies).
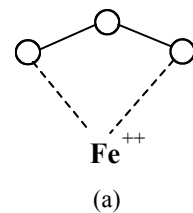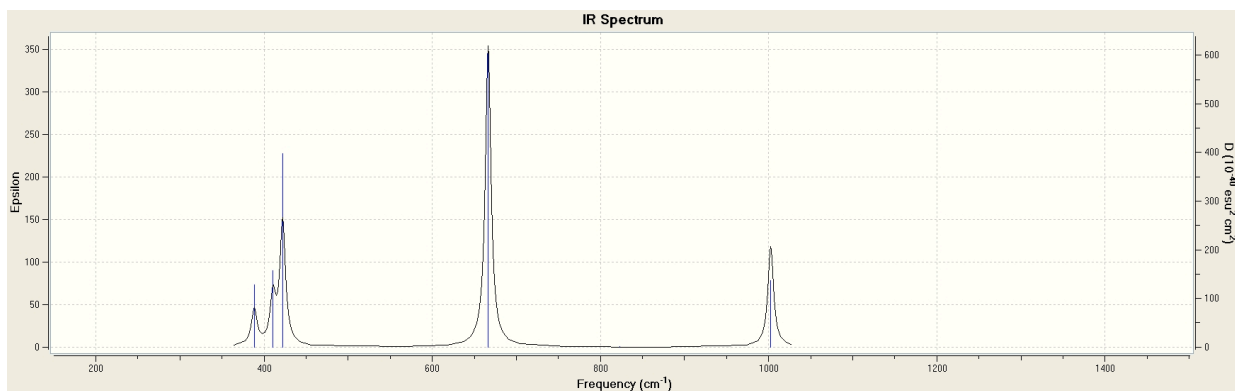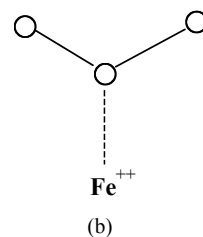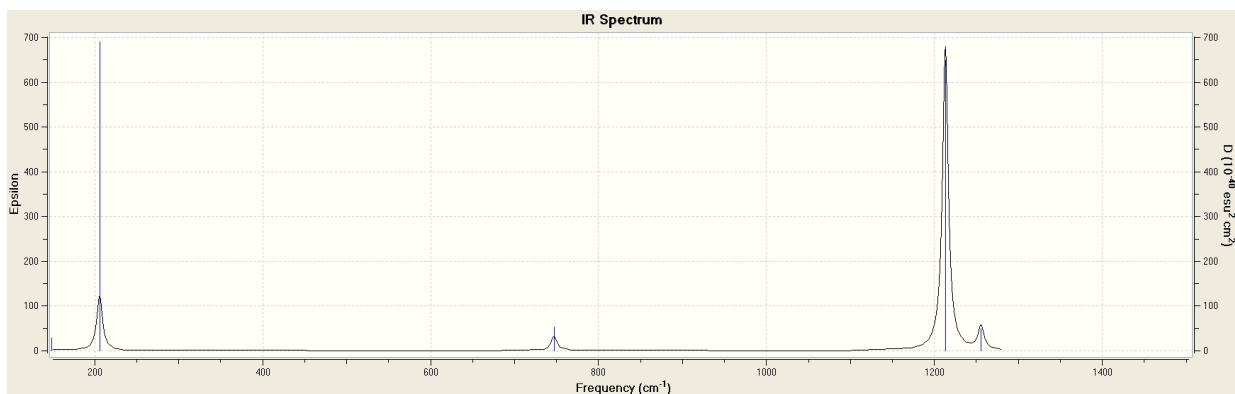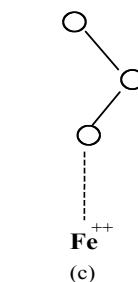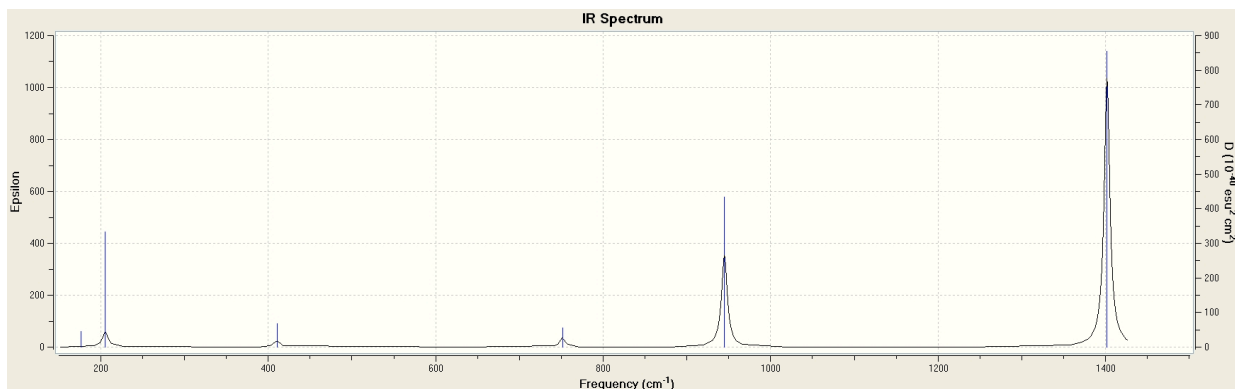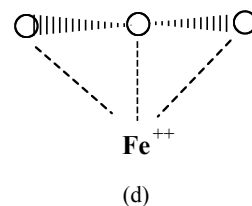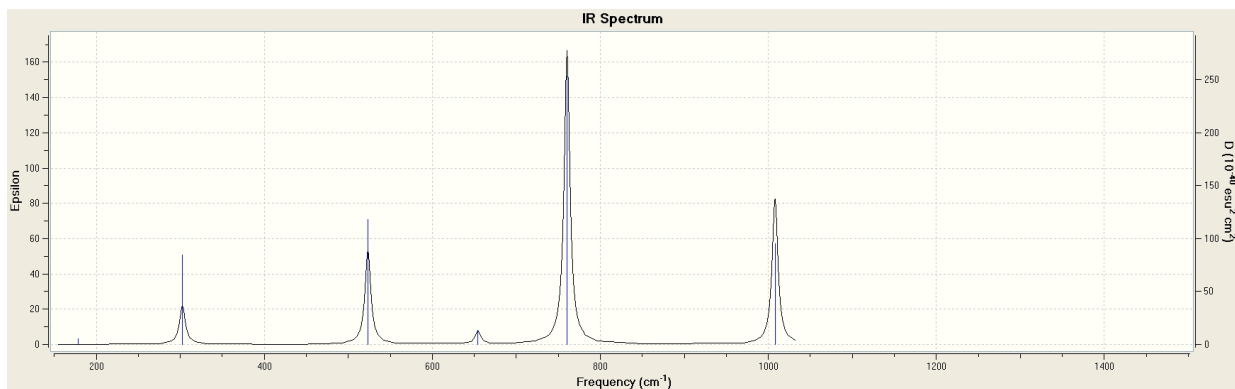
Figure 21. IR spectra for $[Fe\text{-}O_3]^{+2}$, which has net charge +2, in presence of a water solvent background, for different approaches of Ozone.
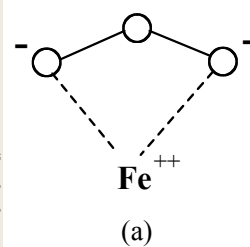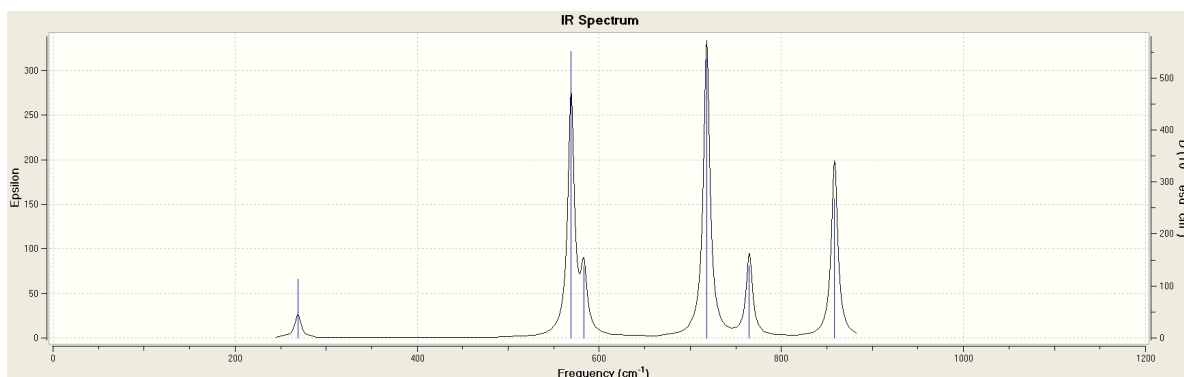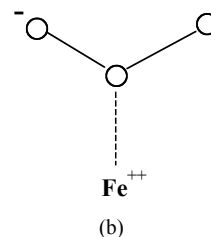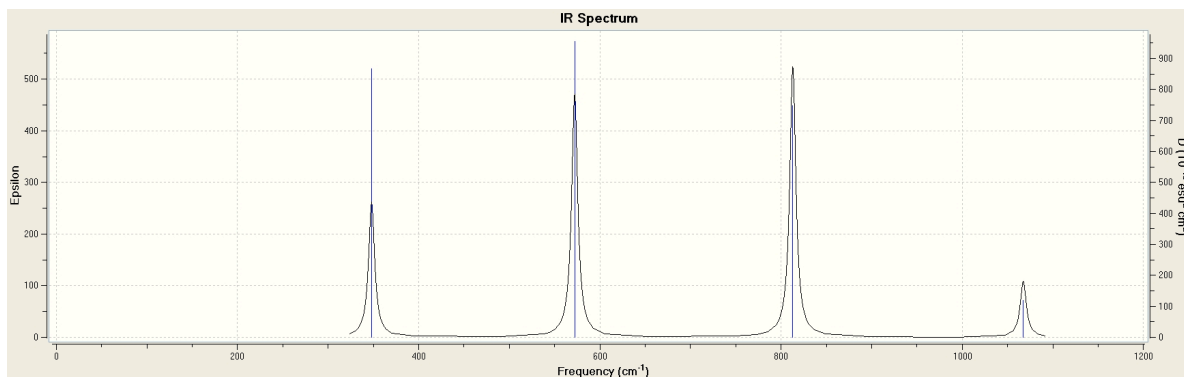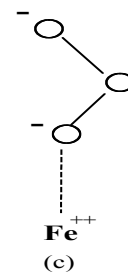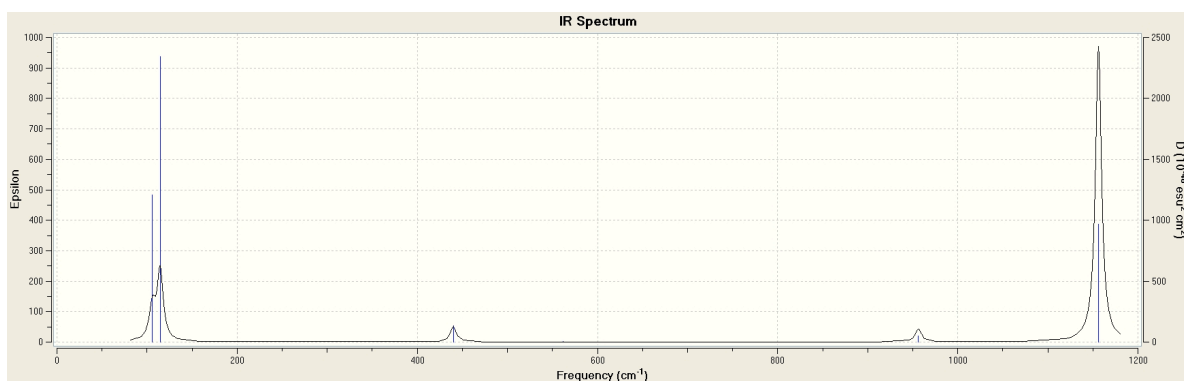
Figure 22. IR spectra for [Fe-O₃], which has 0 net charge, in presence of a water solvent background, for different approaches of Ozone.
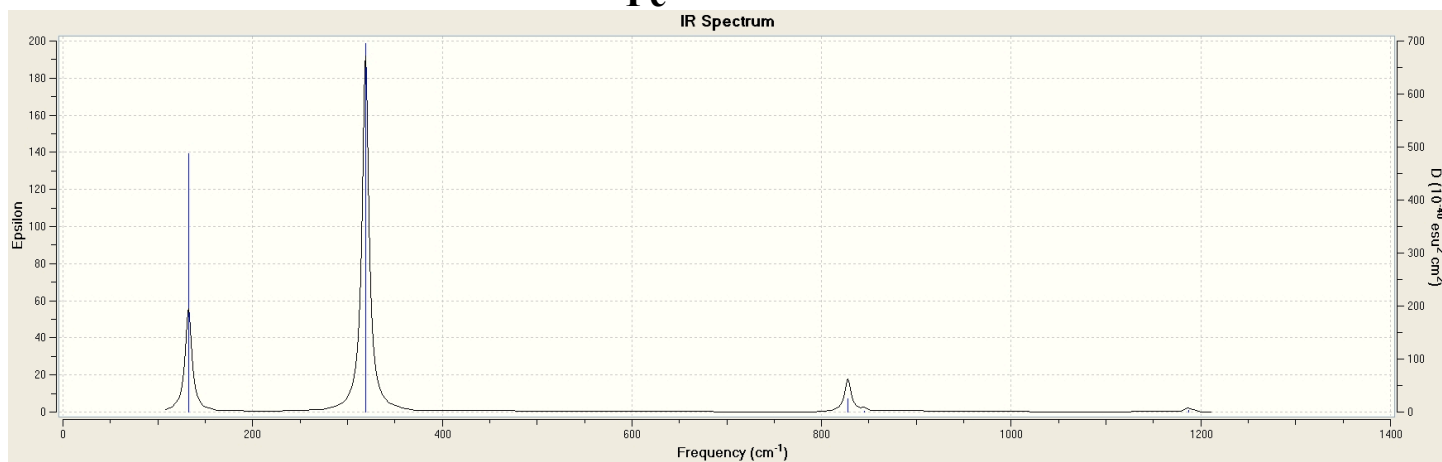
Figure 23. IR spectra for $[Fe\text{-}O_3]^{+2}$, which has net charge +2, for approach of cyclic Ozone, in presence of a water solvent background, for different approaches of Ozone (1 imaginary frequency).
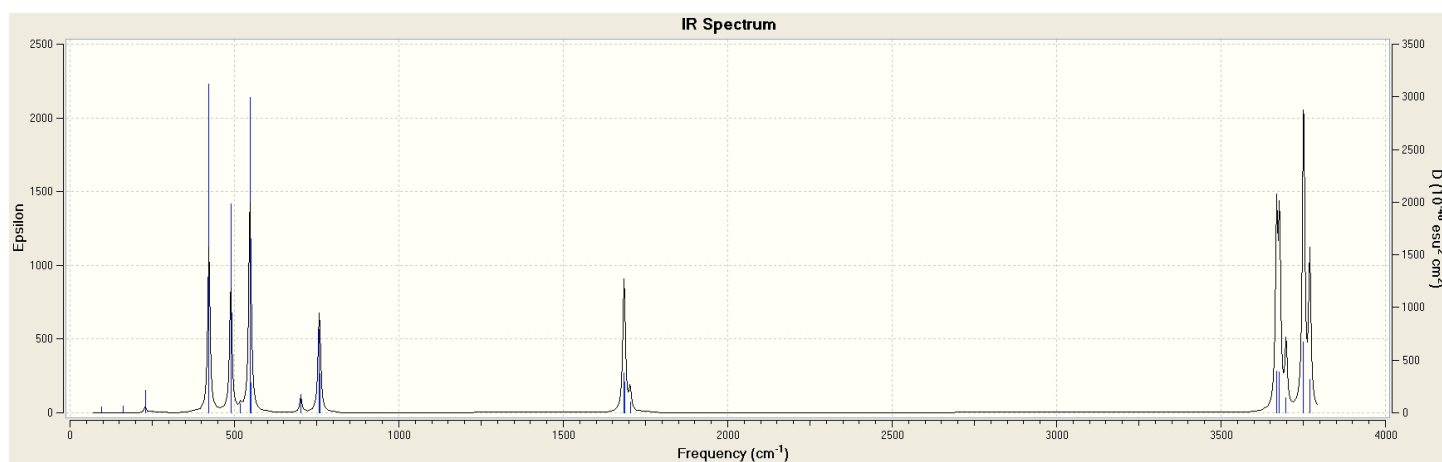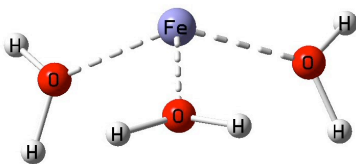
Figure 24. IR spectra for $[Fe^{++}(H_2O)_3]$ (1 imaginary frequency).
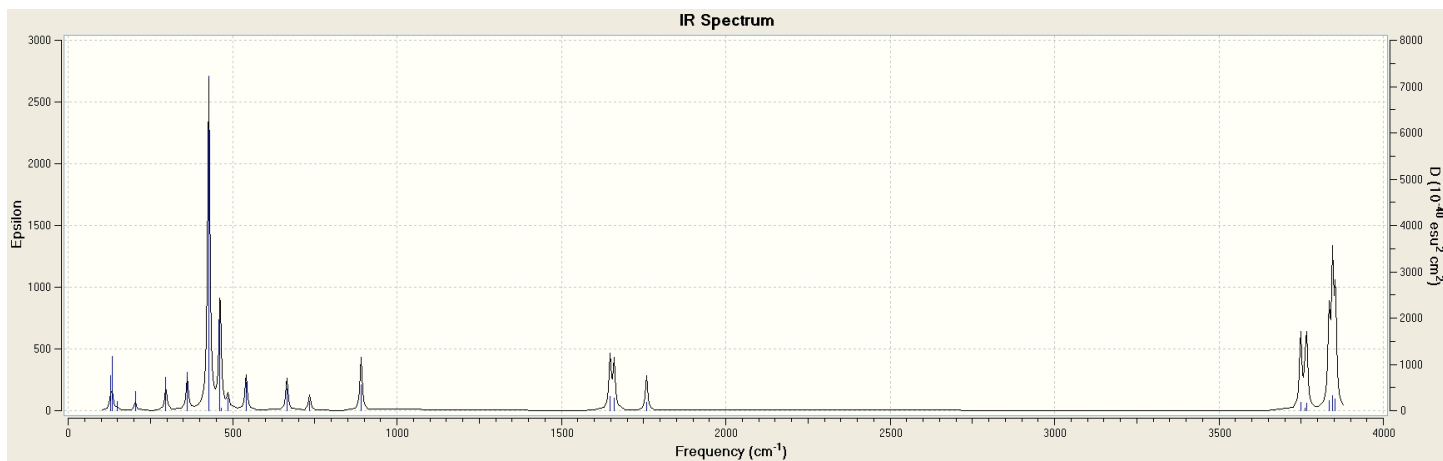
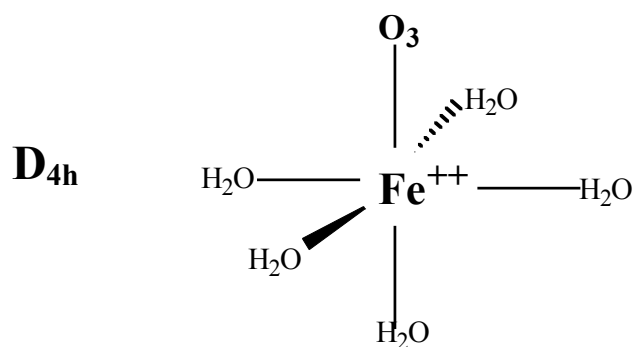**Figure 25.** IR spectra for $[Fe^{++}(H_2O)_3]$ in presence of a water solvent background (1 imaginary frequency).
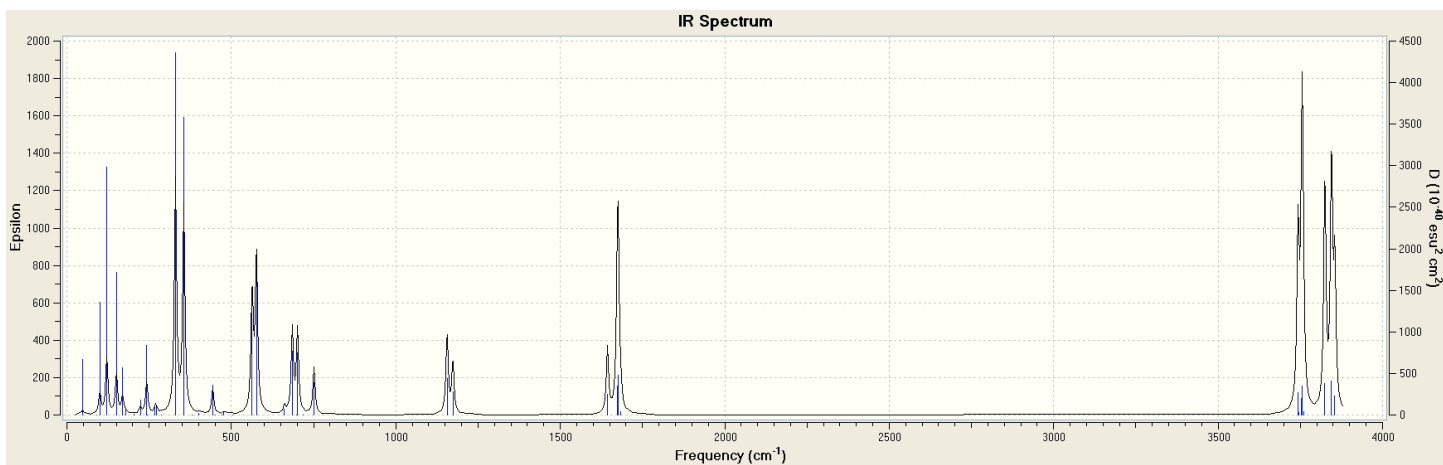
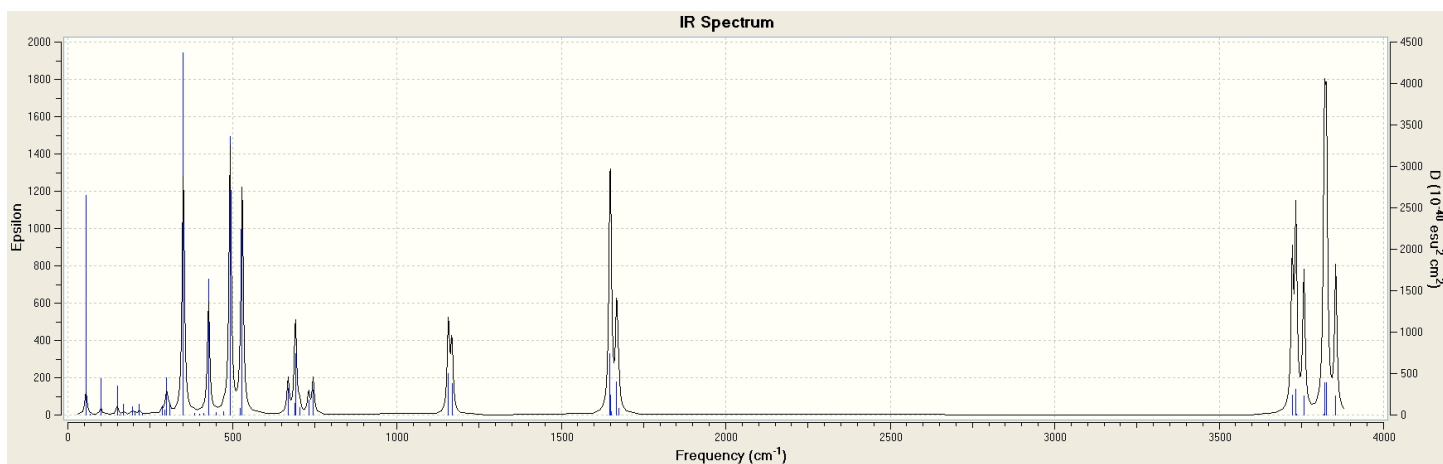**Figure 26.** IR spectra for $[Fe(H_2O)_5O_3]^{+2}$ D_{4h} (2 imaginary frequency).
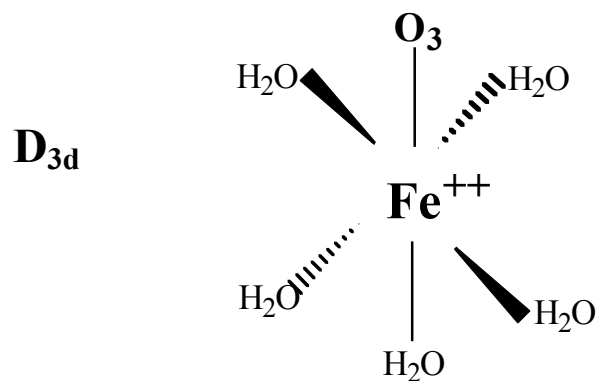
Figure 27. IR spectra for $[Fe(H_2O)_5O_3]^{+2}$ D_{3d} (0 imaginary frequencies).

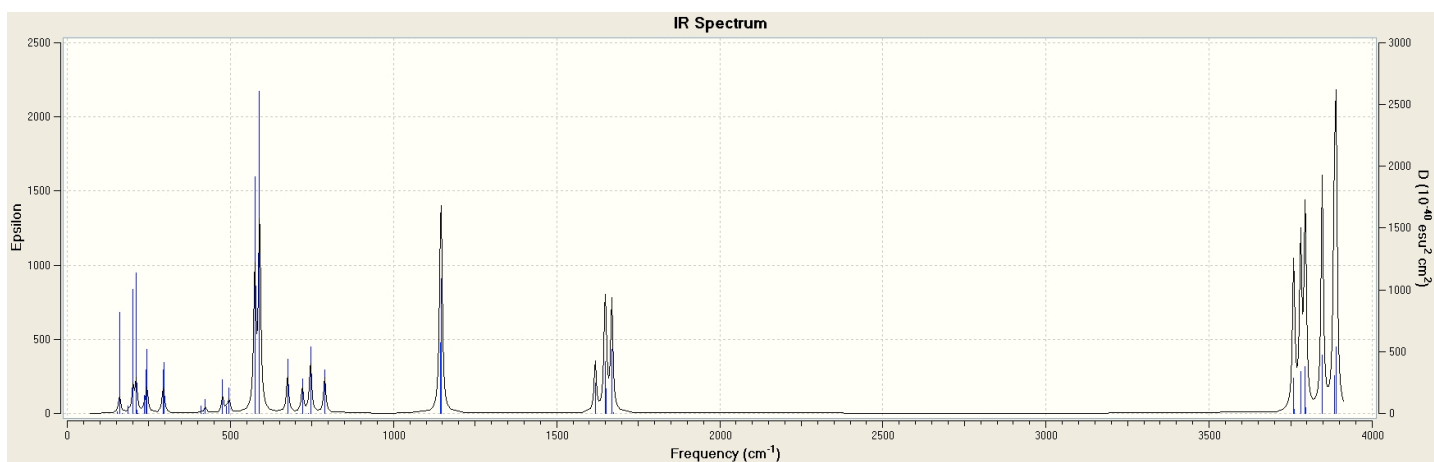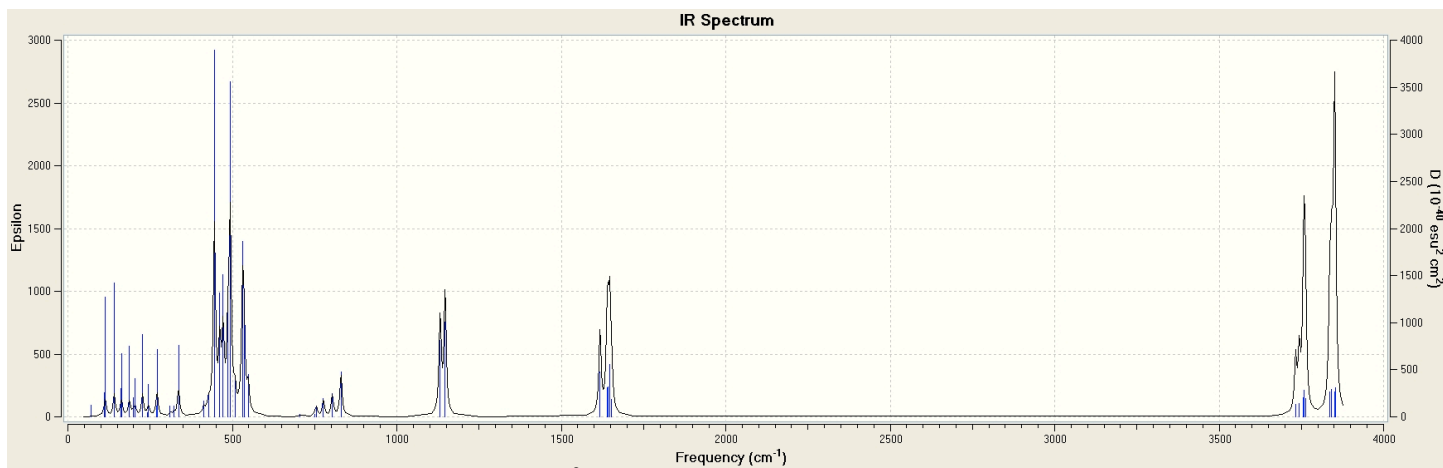**Figure 28.** IR spectra for $[Fe(H_2O)_5O_3]^{+2}$ D_{4h} in presence of a water solvent background (5 imaginary frequency).

Figure 29. IR spectra for $[Fe(H_2O)_5O_3]^{+2}$ D_{3d} in presence of a water solvent background (0 imaginary frequencies).
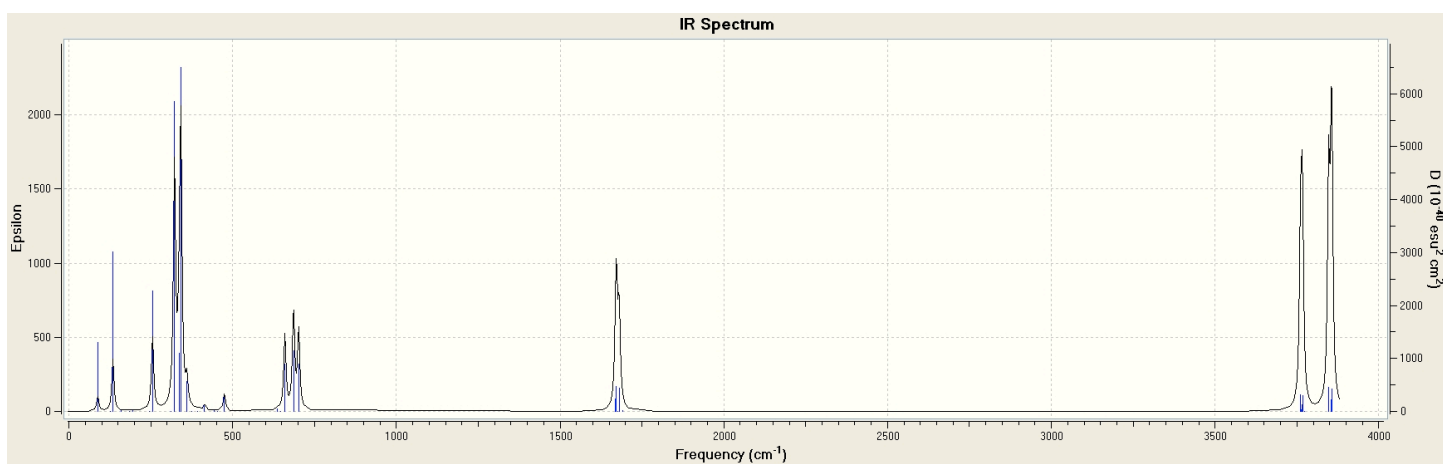

Figure 30. IR spectra for $[Fe^{++}(H_2O)_5]$ D_{4h} (no Ozone) (2 imaginary frequencies).

Figure 31. IR spectra for $[Fe^{++}(H_2O)_5]$ D_{4h} (no Ozone) in presence of a water solvent background (3 imaginary frequencies).

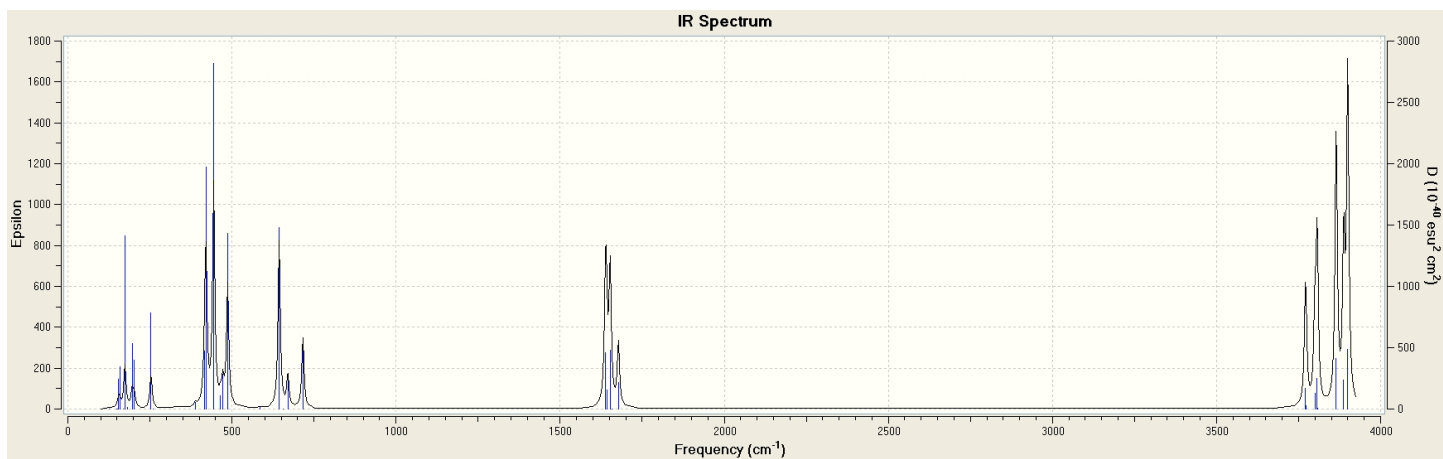**Figure 32.** IR spectra for $[Fe^{++}(H_2O)_5]$ D_{3d} (no Ozone) (0 imaginary frequencies).

Figure 33. IR spectra for $[Fe^{++}(H_2O)_5]$ D_{3d} (no Ozone) in presence of a water solvent background (0 imaginary frequencies).

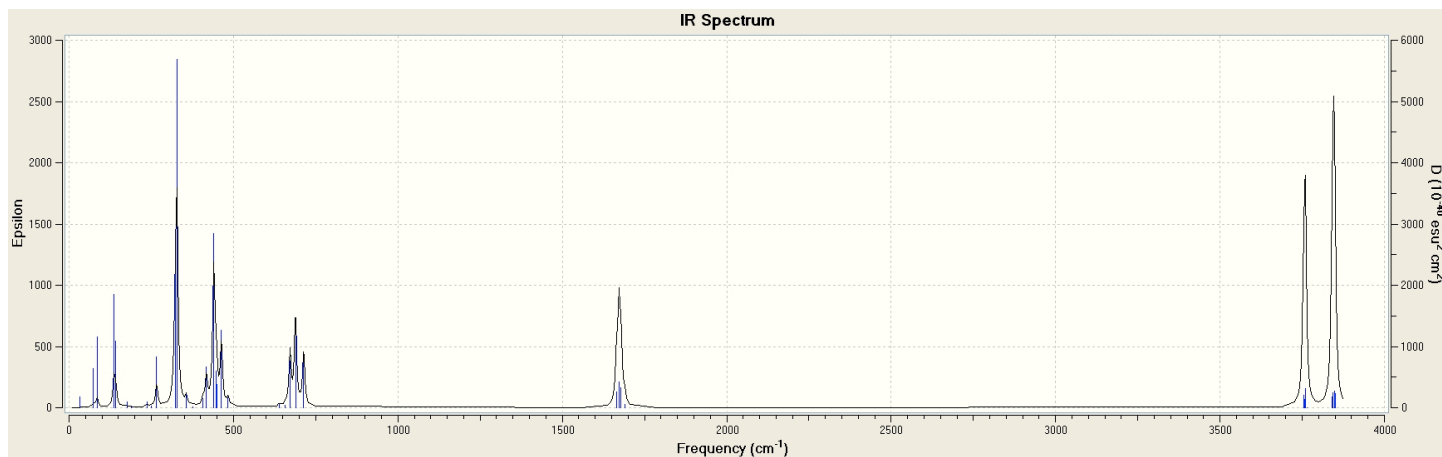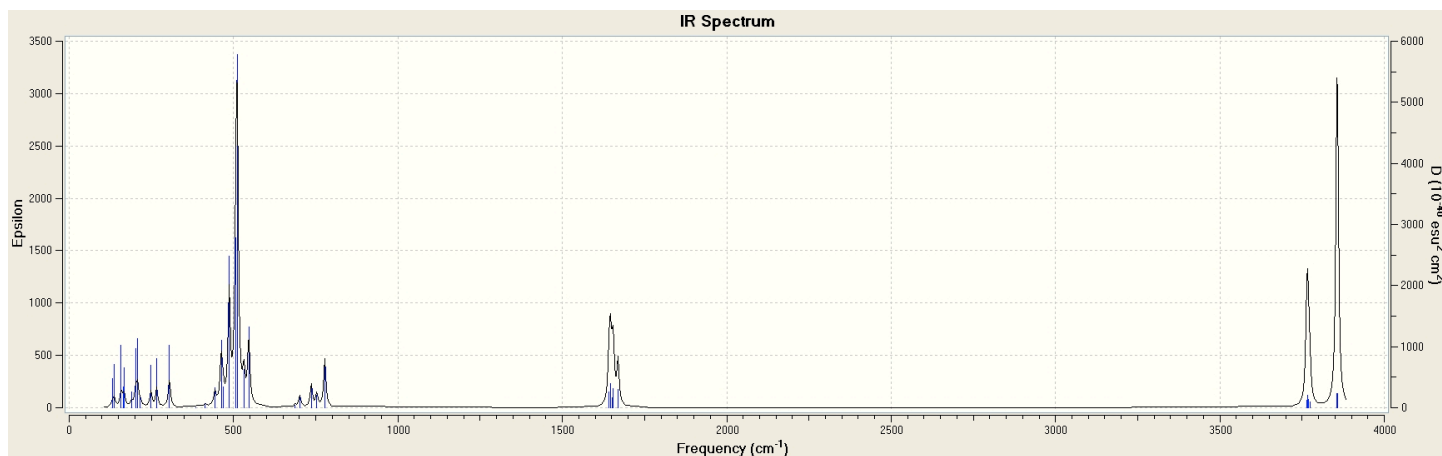**Table 1.** Comparison of energies and numbers of imaginary frequencies for initial and optimized geometries of $[Fe \cdot 3(H_2O) \cdot O_3]^{+2}$ with and without the presence of a water solvent background.

Structure	Start Energy a.u.	Opt Energy a.u.	Imaginary Frequency	+ water solvent Start Energy a.u.	+ water solvent Opt Energy a.u.	+ water solvent Imaginary Frequency
Fe⁺⁺(H₂O)₃	-1492.133	-1492.195	1	-1492.526	-1492.574	1
Fe⁺⁺ +3 H₂O	-1717.637	-1717.706	1	-1717.964	-1718.042	1
Fe⁺⁺ +3 H₂O	-1717.546	-1717.679	NO	-1717.898	-1717.986	NO
Fe⁺⁺ +3 H₂O	-1717.588	-1717.677	NO	-1717.921	-1718.024	NO
Fe⁺⁺ +3 H₂O	-1717483	-1717.707	1	-1717.803	-1718.041	2
Fe⁺⁺ +3 H₂O	-1717.536	-1717.599	2	-1717.852	-1717.940	2

Table 2. Comparison of energies and numbers of imaginary frequencies for initial and optimized geometries of [Fe $\cdot 3(H_2O) \cdot O_3$] with and without the presence of a water solvent background.
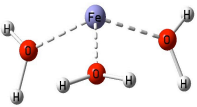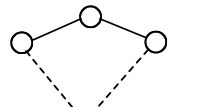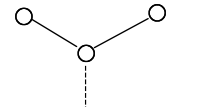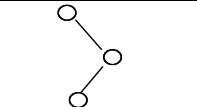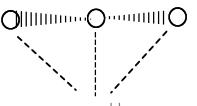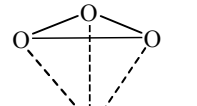
Structure	Start Energy a.u.	Opt Energy a.u.	Imaginary Frequency	+ water solvent Start Energy a.u.	+ water solvent Opt Energy a.u.	+ water solvent Imaginary Frequency
Fe^{++} +3 H₂O	-1718.316	-1718.381	2	-1718.366	-1718.417	1
Fe^{++} +3 H₂O	-1718.117	-1718.388	NO	-1718.198	-1718.417	NO
Fe^{++} +3 H₂O	Converge failed	-	-	-1718.268	-1718.411	NO
Fe^{++} +3 H₂O	-1718.197	-1718.80	1	-1718.234	-1718.412	1

Table 3. Comparison of energies and numbers of imaginary frequencies for initial and optimized geometries of $[Fe-O_3]^{+2}$ in presence of a water solvent background.
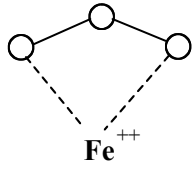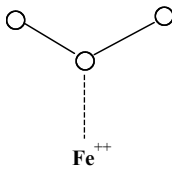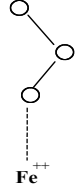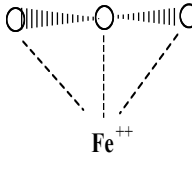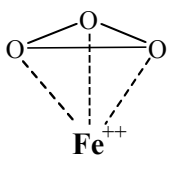
Structure	Start Energy a.u.	Opt Energy a.u.	Imaginary Frequency
	-1488.569	-1488.572	NO
	-1488.540	-1488.549	NO
	-1488.565	-1488.588	NO
	-1488.429	-1488.548	NO
	-1488.482	-1488.507	1

Table 4. Comparison of energies and numbers of imaginary frequencies for initial and optimized geometries of [Fe-O$_3$] in presence of a water solvent background.
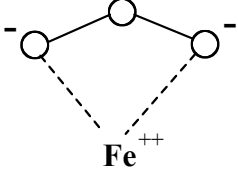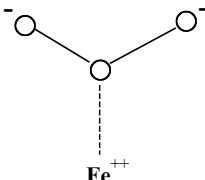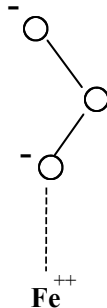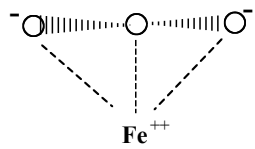
Structure	Start Energy a.u.	Opt Energy a.u.	Imaginary Frequency
	-1489.015	-1489.020	NO
	-1488.909	-1488.922	2
	-1489.054	-1489.059	NO
	-148.868	-1488.973	NO

Table 5. Comparison of energies and numbers of imaginary frequencies for initial and optimized geometries of $[Fe(H_2O)_5]^{+2}$ with and without the presence of a water solvent background.
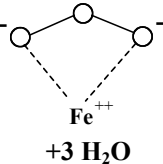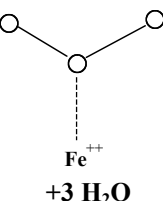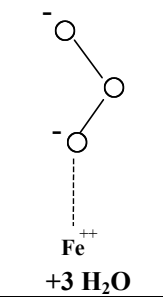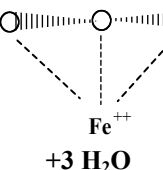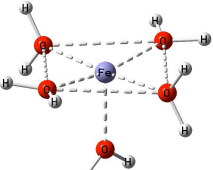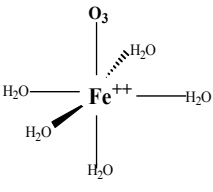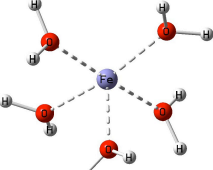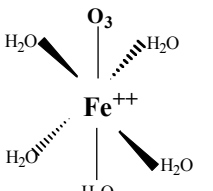
Structure	Start Energy a.u.	Opt Energy a.u.	Imaginary Frequency	+ water solvent Start Energy a.u.	+ water solvent Opt Energy a.u.	+ water solvent Imaginary Frequency
D_{4h} $Fe^{++}(H_2O)_5$	-1645.203	-1645.205	2	-1645.506	-1645.510	3
D_{4h}	-1870.614	-1870.630	2	-1870.912	-1870.930	5
D_{3d} $Fe^{++}(H_2O)_5$	-1645.201	-1645.205	NO	-1645.508	-1645.514	NO
D_{3d}	-1870.608	-1870.638	NO	-1870.907	-1870.937	NO

57

Table 6. Frequencies and IR intensities for stable structures of [Fe $\cdot 3(H_2O)$ $\cdot O_3]^{+2}$ with and without the presence of a water solvent background.
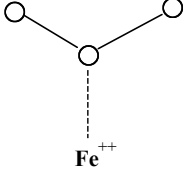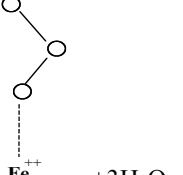
	frequency (cm^{-1})	Intensity (km/mol)	frequency (cm^{-1})	Intensity (km/mol)	frequency (cm^{-1})	Intensity (km/mol)	frequency (cm^{-1})	Intensity (km/mol)
1	63.17	0.35	57.13	1.24	59.13	5.57	95.94	0.76
2	90.06	0.40	155.94	14.62	68.67	1.81	128.00	7.82
3	113.42	2.11	174.27	73.42	100.27	0.72	131.76	3.18
4	138.27	4.25	188.80	4.20	116.93	2.65	166.73	21.21
5	145.15	0.16	215.75	43.49	142.65	6.15	190.55	26.02
6	159.02	1.53	227.59	31.97	182.80	3.74	220.54	7.91
7	186.68	3.37	253.03	1.37	189.00	10.41	230.09	18.81
8	219.09	16.61	279.99	26.29	248.36	1.94	256.01	40.72
9	221.62	4.11	295.11	37.21	280.32	3.86	286.05	2.74
10	270.55	4.11	317.14	29.56	320.17	16.25	306.00	1.64
11	330.07	15.64	330.98	23.90	337.86	17.03	324.36	59.28
12	397.46	156.65	432.36	183.32	374.61	13.93	377.42	34.87
13	404.56	89.30	474.50	138.43	422.13	261.69	475.91	229.49
14	438.44	25.79	479.98	19.80	457.86	5.63	491.83	66.91
15	453.88	328.31	514.40	298.99	473.82	30.86	503.84	183.74
16	512.41	189.23	522.07	17.73	483.76	202.86	516.31	35.10
17	515.90	58.95	547.63	201.98	524.99	337.17	581.94	362.01
18	523.78	110.09	592.40	399.84	562.13	67.11	608.26	383.59
19	582.79	25.11	718.77	15.59	680.85	71.75	720.44	35.40
20	703.26	48.97	765.57	21.06	694.80	73.47	740.45	61.24
21	731.87	63.66	775.89	42.86	722.95	10.97	750.08	35.50
22	751.08	77.97	876.44	49.55	764.08	96.27	795.76	40.35
23	852.70	37.50	1137.94	208.33	883.34	43.72	894.96	64.33
24	1436.20	253.56	1186.06	218.70	1425.16	234.72	1318.50	598.92
25	1671.79	138.52	1610.98	184.48	1670.45	166.21	1639.33	112.06
26	1684.78	147.27	1631.82	157.41	1675.12	101.63	1652.98	193.82
27	1699.44	52.03	1691.05	119.60	1695.23	75.20	1657.79	88.53
28	3701.23	271.42	3712.27	149.08	3694.03	358.60	3718.11	257.87
29	3711.23	391.45	3744.12	417.87	3701.76	198.81	3733.44	158.45
30	3718.98	127.49	3747.86	18.93	3719.75	304.43	3748.77	316.10
31	3785.72	252.36	3809.19	337.18	3782.97	200.62	3798.53	245.11
32	3790.97	239.33	3834.26	285.92	3789.39	289.66	3824.43	296.77
33	3793.58	295.05	3843.98	301.26	3796.01	313.40	3838.50	277.68

Table 7. Frequencies and IR intensities for stable structures of [Fe ·3(H_2O) ·O_3] with and without the presence of a water solvent background.
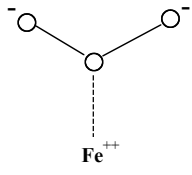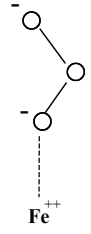
	frequency (cm^{-1})	Intensity (km/mol)	frequency (cm^{-1})	Intensity (km/mol)	frequency (cm^{-1})	Intensity (km/mol)
1	101.22	6.04	90.78	2.28	43.55	1.47
2	127.15	4.20	128.80	2.56	97.71	8.25
3	144.46	7.18	146.63	42.05	133.54	20.04
4	169.37	8.22	172.60	10.74	174.97	54.68
5	221.42	60.88	219.50	66.53	200.65	17.39
6	260.35	72.88	232.24	45.59	220.15	14.27
7	267.00	7.64	260.76	60.75	232.16	71.02
8	311.89	49.18	305.62	38.36	290.73	49.64
9	360.95	6.12	351.54	6.02	309.68	73.19
10	390.47	1.84	371.28	39.69	361.00	33.93
11	406.46	20.30	403.49	1.68	411.19	23.28
12	436.66	37.86	412.39	49.67	432.07	106.45
13	464.83	36.04	475.70	423.26	438.49	322.56
14	504.26	178.48	488.86	47.10	521.53	77.60
15	518.19	129.81	497.23	134.53	532.95	46.92
16	568.18	102.04	534.82	40.48	561.35	97.29
17	631.30	123.43	543.92	48.12	573.24	25.16
18	655.22	88.96	628.05	309.47	641.31	35.20
19	695.71	115.21	660.41	32.11	664.23	143.72
20	721.98	19.39	726.01	116.25	689.92	145.30
21	733.26	95.72	746.71	127.14	779.91	223.05
22	803.65	94.66	791.13	147.79	824.39	323.85
23	866.56	196.56	880.10	32.44	870.98	96.99
24	885.27	24.39	968.26	158.13	921.25	75.24
25	1458.27	58.82	1592.48	147.48	1591.28	93.67
26	1615.40	84.34	1626.99	124.76	1604.41	73.62
27	1654.91	39.51	1653.87	74.08	1634.25	137.02
28	3204.87	332.53	2816.95	874.06	3004.23	805.76
29	3513.50	122.67	3451.02	336.01	3216.59	488.13
30	3649.79	84.50	3764.05	66.60	3760.51	55.55
31	3810.31	5.75	3804.82	93.77	3799.88	14.93
32	3812.57	81.78	3813.88	11.56	3824.39	129.85
33	3847.04	90.73	3858.08	188.45	3870.93	198.24

Table 8. Frequencies and IR intensities for stable structures of $[Fe \cdot O_3]^{+2}$ in presence of a water solvent background.
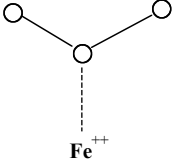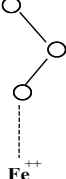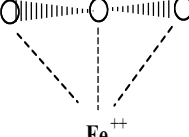
	frequency (cm^{-1})	Intensity (km/mol)	frequency (cm^{-1})	Intensity (km/mol)	frequency (cm^{-1})	Intensity (km/mol)	frequency (cm^{-1})	Intensity (km/mol)
1	388.33	12.49	148.48	1.07	176.10	2.02	178.63	0.24
2	410.61	16.16	152.31	0.02	205.59	17.17	302.55	6.39
3	422.12	42.13	205.77	35.59	410.56	7.01	523.37	15.45
4	666.49	102.43	746.98	9.88	751.43	10.34	654.37	2.15
5	823.08	0.20	1213.07	197.10	944.86	102.56	760.40	48.24
6	1002.50	34.27	1255.54	15.57	1401.77	300.13	1008.01	24.03

Table 9. Frequencies and IR intensities for stable structures of $[Fe \cdot O_3]^{+2}$ in presence of a water solvent background.
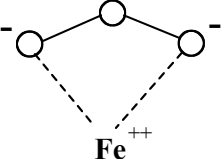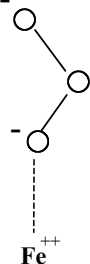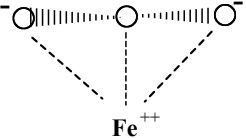
	frequency (cm^{-1})	Intensity (km/mol)	frequency (cm^{-1})	Intensity (km/mol)	frequency (cm^{-1})	Intensity (km/mol)
1	268.96	7.61	105.85	32.06	321.90	17.24
2	569.06	78.62	114.55	67.25	411.54	22.42
3	583.08	20.20	440.01	14.74	526.19	23.80
4	717.97	96.23	562.06	0.86	612.05	5.23
5	764.84	26.69	956.28	12.37	696.99	42.95
6	858.47	57.64	1156.21	281.06	893.21	76.08

Table 10. Frequencies and IR intensities for stable structure of $Fe^{++}(H_2O)_3$ (no Ozone) with and without the presence of a water solvent background.
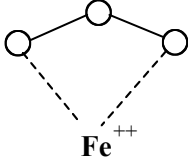
	frequency (cm^{-1})	Intensity (km/mol)	frequency (cm^{-1})	Intensity (km/mol)
1	-54.93	6.92	-297.33	19.68
2	95.48	1.28	128.28	24.53
3	139.12	0.10	134.40	39.67
4	160.47	2.41	149.89	7.14
5	228.68	12.05	204.19	21.27
6	252.11	0.00	297.30	54.35
7	422.30	330.34	362.37	75.14
8	488.81	243.07	427.69	774.50
9	489.86	14.95	461.90	270.44
10	518.37	11.53	466.91	7.14
11	546.97	410.80	485.89	32.17
12	550.86	39.25	541.34	83.44
13	702.17	30.98	665.37	76.91
14	757.20	149.72	734.25	37.42
15	760.33	71.04	891.06	124.25
16	1683.90	160.20	1648.33	124.94
17	1686.15	123.67	1660.54	112.77
18	1703.40	44.92	1759.27	81.19
19	3669.11	362.79	3748.67	175.96
20	3677.90	358.45	3761.91	57.99
21	3697.97	128.75	3766.93	153.60
22	3748.81	1.46	3835.12	204.94
23	3751.17	628.29	3845.61	318.46
24	3769.93	298.76	3854.38	247.18

Table 11. Frequencies and IR intensities for stable structure of $Fe^{++}(H_2O)_5$ D_{3d} (no Ozone) with and without the presence of a water solvent background.

	frequency (cm^{-1})	Intensity (km/mol)	frequency (cm^{-1})	Intensity (km/mol)
			In water solvent	
1	33.56	1.44	131.22	15.53
2	73.97	11.85	136.98	24.45
3	85.49	24.74	158.07	40.33
4	135.45	8.15	164.53	14.08
5	137.01	63.78	167.58	27.46
6	142.56	38.97	189.27	12.39
7	177.81	3.99	202.31	49.28
8	189.14	1.11	208.33	58.96
9	236.51	5.49	216.33	9.68
10	250.75	1.99	248.75	43.72
11	266.30	55.09	266.04	53.57
12	322.65	176.32	304.75	78.16
13	328.07	467.55	385.97	0.43
14	356.66	22.35	412.44	7.23
15	375.95	1.39	443.33	36.02
16	407.48	15.37	462.32	128.08
17	417.69	69.91	467.56	40.10
18	439.98	313.48	486.52	302.72
19	446.20	66.81	507.22	353.32
20	449.14	43.48	511.09	740.97
21	463.42	146.93	531.44	83.18
22	483.71	19.89	546.10	181.68
23	638.99	8.02	686.44	7.42
24	657.66	5.89	701.25	32.01
25	672.10	127.47	736.62	63.66
26	688.59	222.57	753.09	37.99
27	713.58	132.28	777.62	134.24
28	1664.99	108.94	1642.07	105.11
29	1672.08	179.59	1646.16	165.58
30	1673.90	47.57	1652.16	66.94
31	1678.82	135.27	1655.19	130.65
32	1689.62	24.01	1669.23	123.16
33	3753.66	193.43	3763.44	109.51
34	3758.18	128.13	3765.85	189.51
35	3758.58	97.90	3766.86	8.25
36	3759.94	293.86	3768.65	130.20
37	3765.86	5.67	3773.39	94.06
38	3839.96	169.11	3855.37	164.02
39	3843.89	160.39	3855.74	208.81
40	3844.51	237.00	3856.33	228.74
41	3847.34	266.35	3857.33	224.44
42	3849.95	216.97	3859.02	219.26

Table 12(a). Frequencies and IR intensities for stable structure of $[Fe(H_2O)_5O_3]^{+2}$ D_{3d} with and without the presence of a water solvent background.
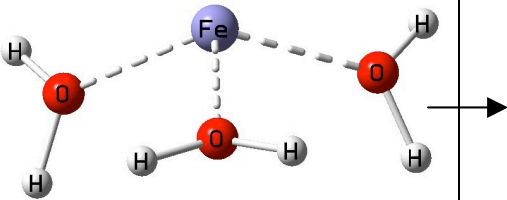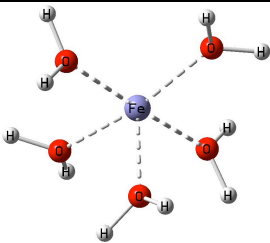
	frequency (cm^{-1})	Intensity (km/mol)	frequency (cm^{-1})	Intensity (km/mol)
			In water solvent	
1	55.05	36.60	71.25	2.14
2	68.43	0.15	109.86	6.95
3	100.10	10.92	114.01	36.23
4	149.98	13.22	140.96	50.15
5	157.40	0.09	160.78	12.00
6	160.78	0.04	163.94	27.51
7	169.03	5.69	186.95	35.19
8	195.64	4.82	198.12	9.96
9	203.34	2.03	204.75	21.00
10	203.40	0.68	226.93	49.86
11	217.01	6.90	242.09	2.87
12	227.91	1.08	245.52	21.31
13	286.03	7.57	269.08	7.71
14	294.91	4.28	271.53	48.81
15	300.62	33.71	310.55	8.84
16	308.61	10.87	322.42	9.08
17	350.97	384.86	336.35	63.88
18	385.28	2.33	414.02	17.14
19	400.66	1.14	428.19	25.29
20	413.04	1.75	445.42	435.08
21	427.65	175.53	461.66	151.99
22	449.68	3.74	471.74	178.05
23	473.94	4.48	486.43	155.70
24	474.07	3.98	493.49	440.19
25	493.36	414.95	507.98	48.09

Table 12(b). Frequencies and IR intensities for stable structure of $[Fe(H_2O)_5O_3]^{+2}$ D_{3d} with and without the presence of a water solvent background.

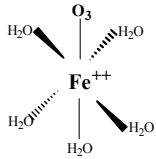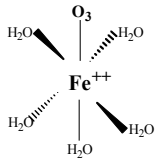|			In water solvent	
	frequency (cm^{-1})	Intensity (km/mol)	frequency (cm^{-1})	Intensity (km/mol)
26	523.60	10.09	531.08	248.43
27	529.83	339.56	535.39	174.40
28	530.00	20.87	548.39	62.04
29	669.53	53.96	705.20	4.30
30	691.30	23.65	750.48	5.51
31	691.85	128.58	755.42	20.07
32	704.36	16.25	776.84	38.33
33	732.06	32.88	803.88	49.78
34	745.60	55.22	830.43	98.70
35	1156.94	144.44	1131.76	230.30
36	1167.58	111.63	1146.92	288.38
37	1648.30	304.39	1617.80	194.81
38	1649.69	101.20	1639.23	128.38
39	1653.42	15.16	1641.65	132.52
40	1668.55	165.85	1647.41	228.66
41	1674.42	32.15	1653.29	75.11
42	3722.12	225.36	3732.57	122.87
43	3723.18	4.10	3743.68	135.01
44	3733.24	291.76	3756.54	187.68
45	3736.24	13.82	3759.00	262.76
46	3757.77	215.30	3762.68	184.61
47	3819.55	5.49	3836.55	257.20
48	3820.12	375.66	3842.47	279.46
49	3824.99	21.76	3850.28	230.82
50	3826.10	376.32	3851.01	254.59
51	3854.55	226.05	3852.79	294.36